PMR 3301

Simulação de Processos no Estado Sólido

Izabel Machado

machadoi@usp.br

Mechatronics and Mechanical Systems Engineering Department – Escola Politécnica – University of São Paulo

http://lattes.cnpq.br/6705415923436933

CAD - FEA –CAM- FEA/CAM

- Objetivo é dar uma visão geral de como análises utilizando elementos finitos e softwares de apoio, como o CAD, são importantes na manufatura de componentes

Análise utilizando elementos finitos

- FEM - https://www.youtube.com/watch?v=boSLQYhDXoE
- FEM - https://www.youtube.com/watch?v=boSLQYhDXoE
- ABAQUS
- ANSYS
- DEFORM
- MAGMA
- LS DYNA
- CONSOL
- MATLAB (otimização, machine learning)
- EXCEL (estatística e otimização)
- SOLID WORKS
- OUTDESK
- E muito mais....

Análise utilizando elementos finitos

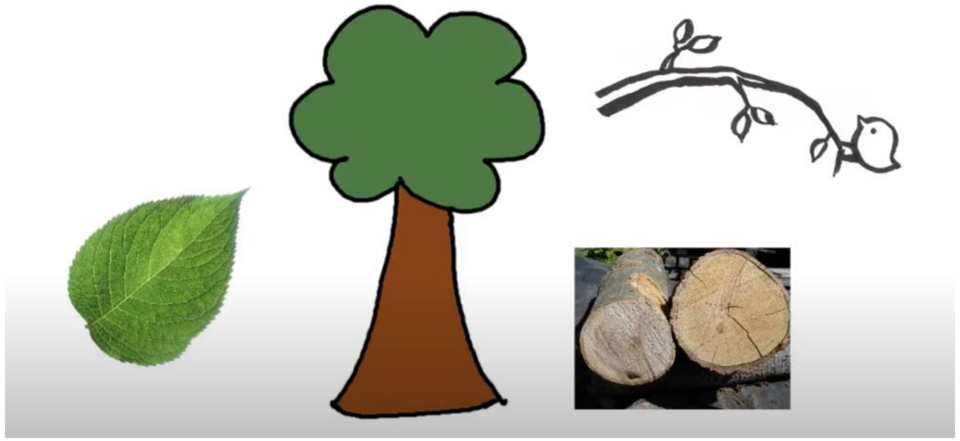

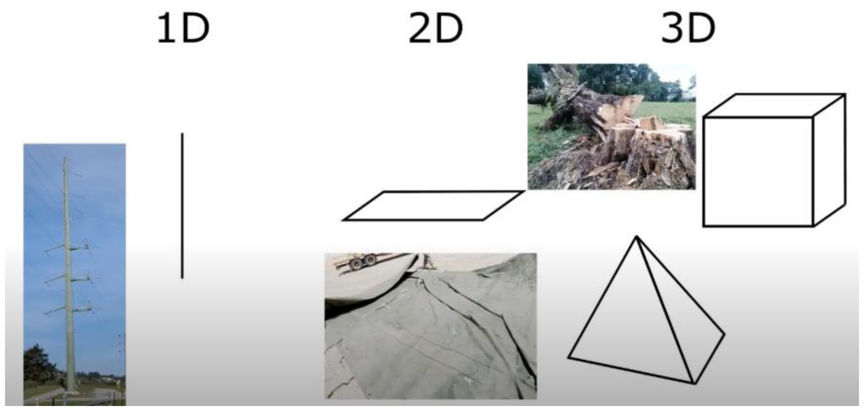

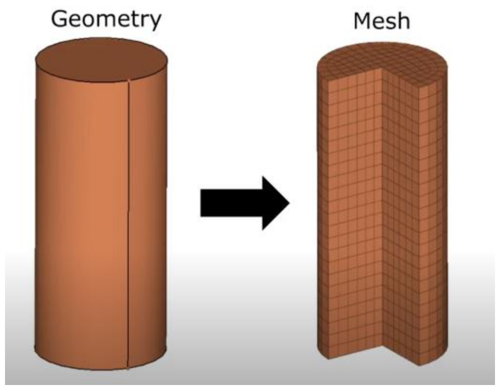

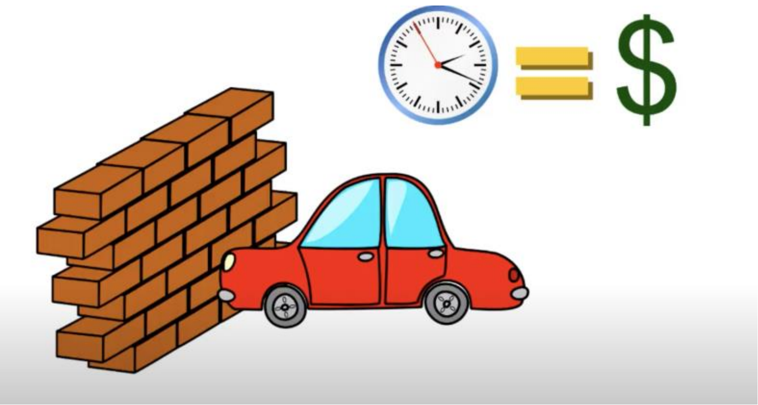

❑FEM - https://www.youtube.com/watch?v=boSLQYhDXoE

Simulação


Functional Generative Design
Setup do Design Space
Objetivos & Restrições
Explorar
Gerar
1
2
3
4
5
Setup da análise
Validar
6
Detalhamento
10
9
8
7
Validação
Seleção da opção vencedora
Geometrias alternativas
© Dassault Systèmes | Confidential Information | 4/15/2020 | ref.: 3DS_Document_2019
DASSAULT SYSTEMES

Simulação

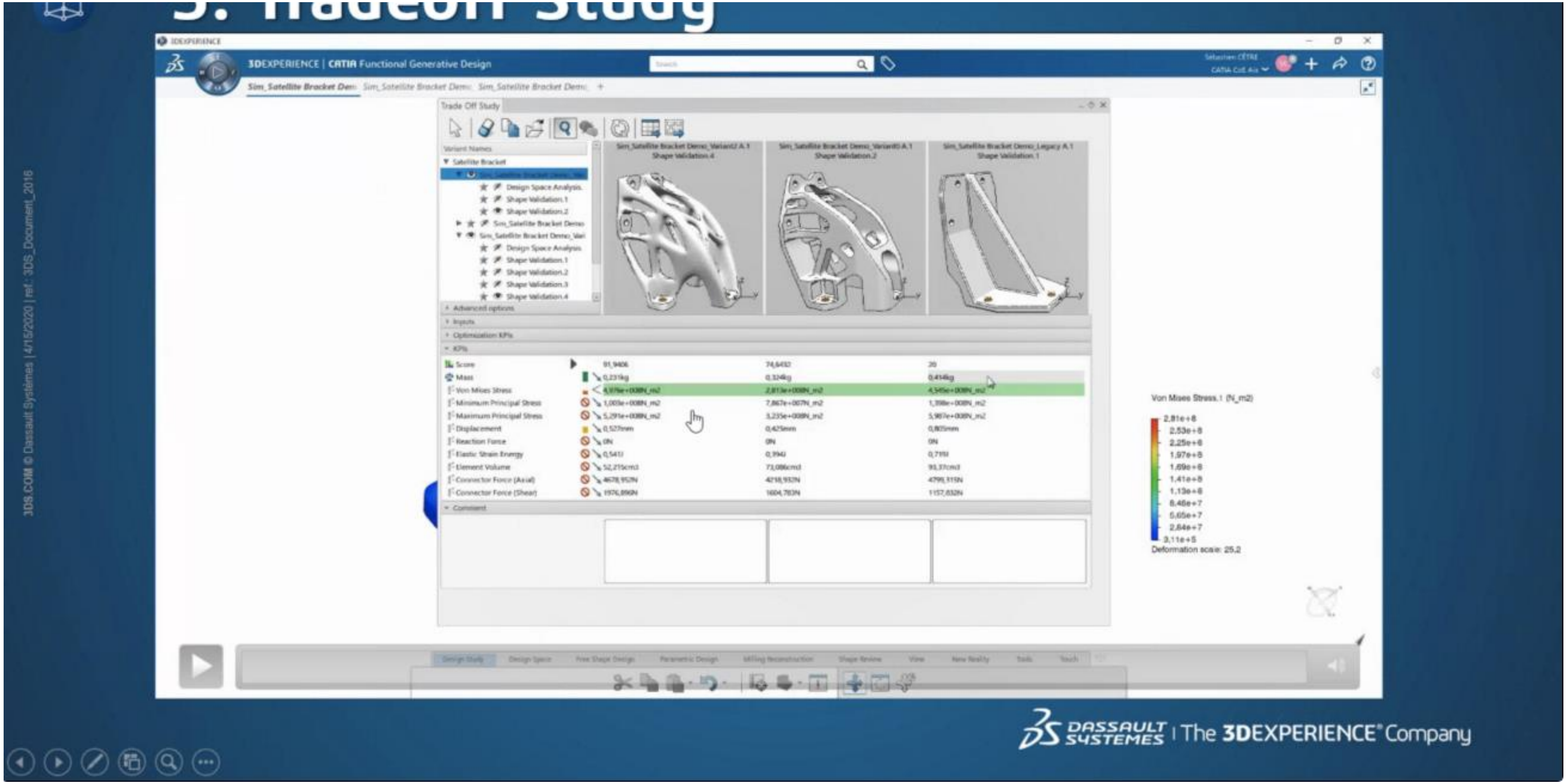
3DEXPERIENCE | CATIA Functional Generative Design
Trade Off Study
Von Mises Stress.1 (N_m2)
DASSAULT SYSTEMES | The 3DEXPERIENCE® Company

Simulação

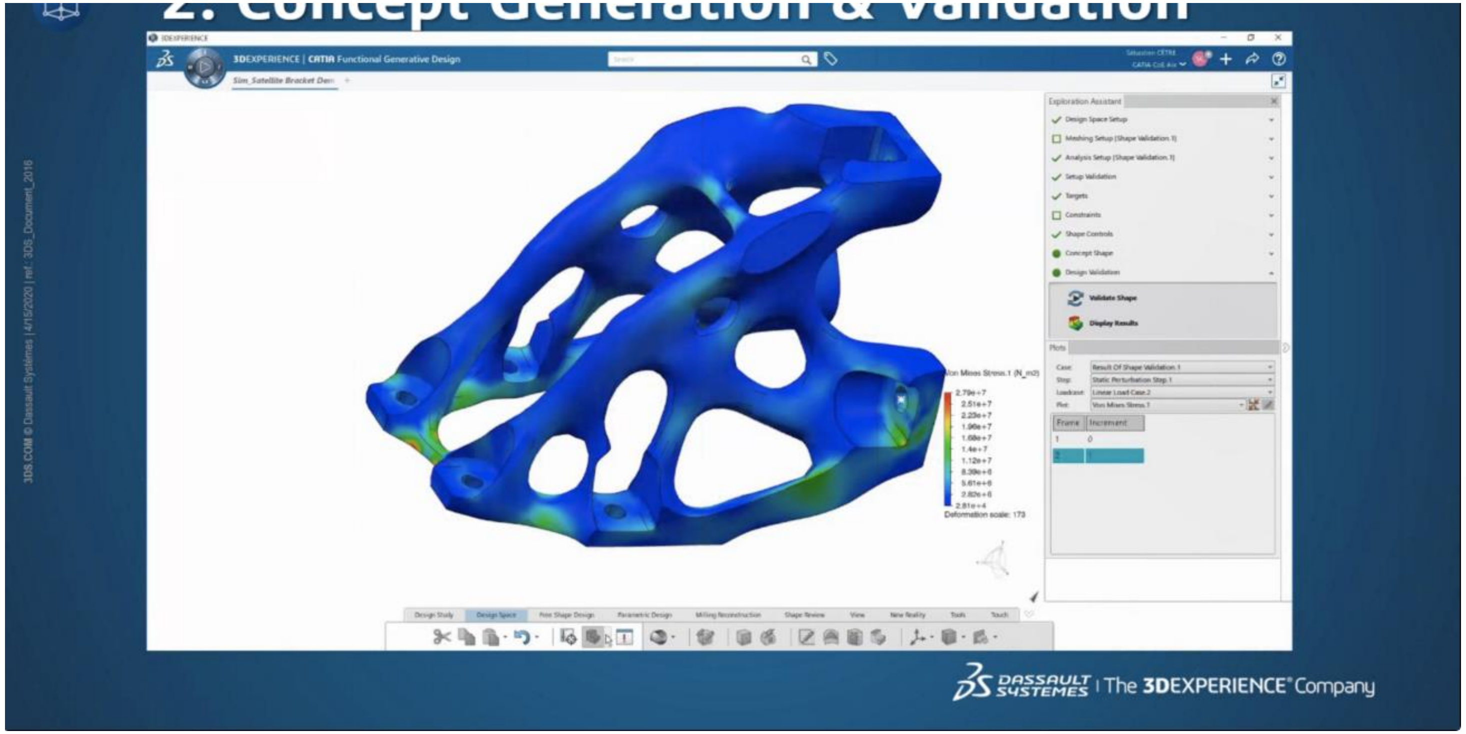
3DEXPERIENCE | CATIA Functional Generative Design
Exploration Assistant
Von Mises Stress.1 (N_m2)
DASSAULT SYSTEMES | The 3DEXPERIENCE Company

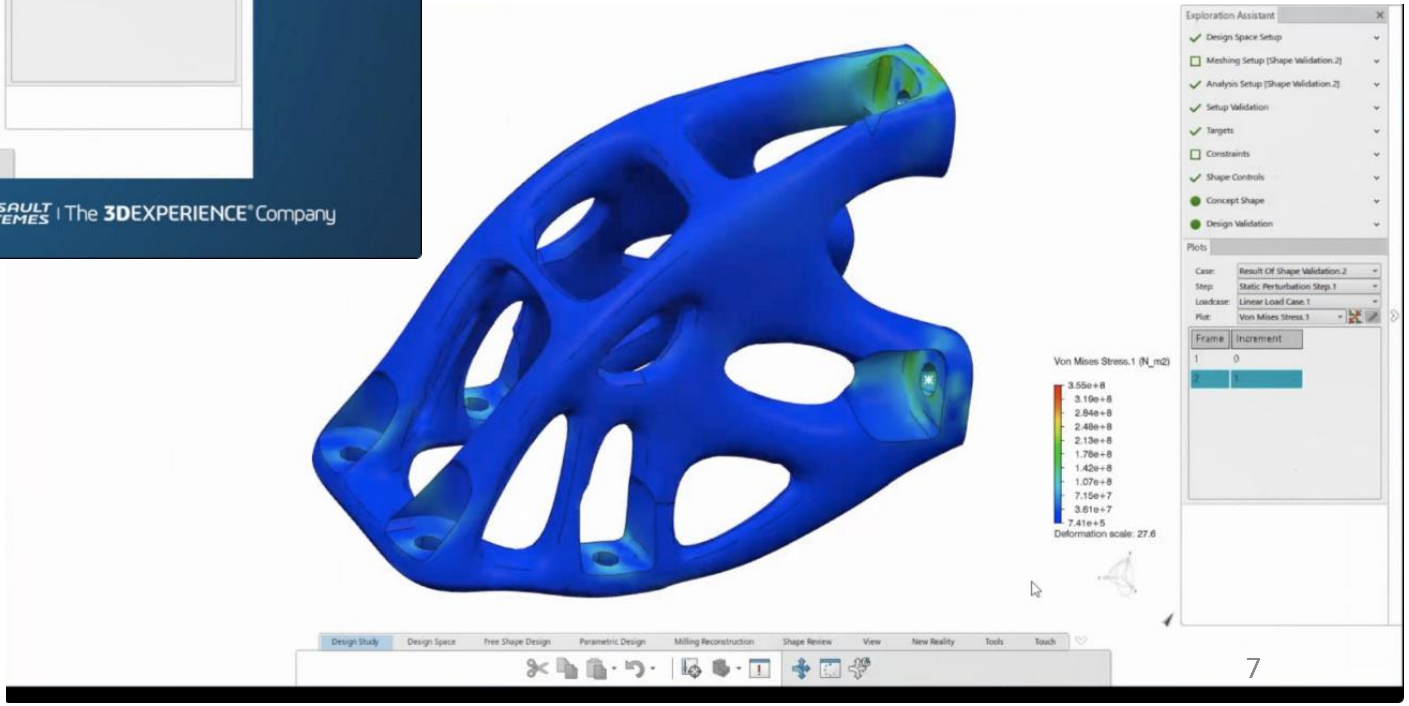
Exploration Assistant
Design Space Setup
Setup Validation
Targets
Constraints
Shape Controls
Concept Shape
Design Validation
Von Mises Stress.1 (N_m2)
3.55e+8
3.19e+8
2.84e+8
2.48e+8
2.13e+8
1.78e+8
1.42e+8
1.07e+8
7.15e+7
3.61e+7
7.41e+5
Deformation scale: 27.6

Exercise 1 – Cantilever Beam

- **PART:** 2D – Deformable – Shell

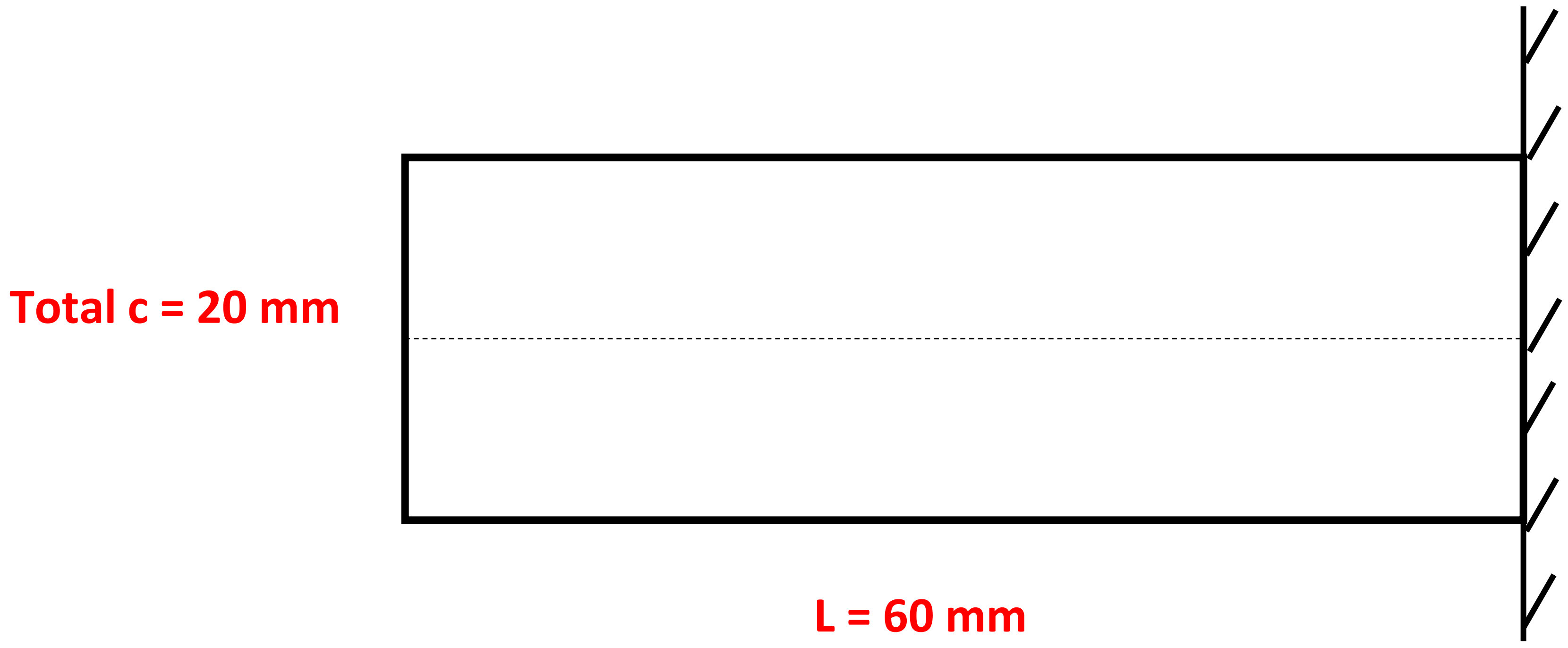

Partition: Face – 2 points

Exercise 1 – Cantilever Beam

- **PROPERTIES: Steel -** E = 200 GPa; $\nu = 0.3$;

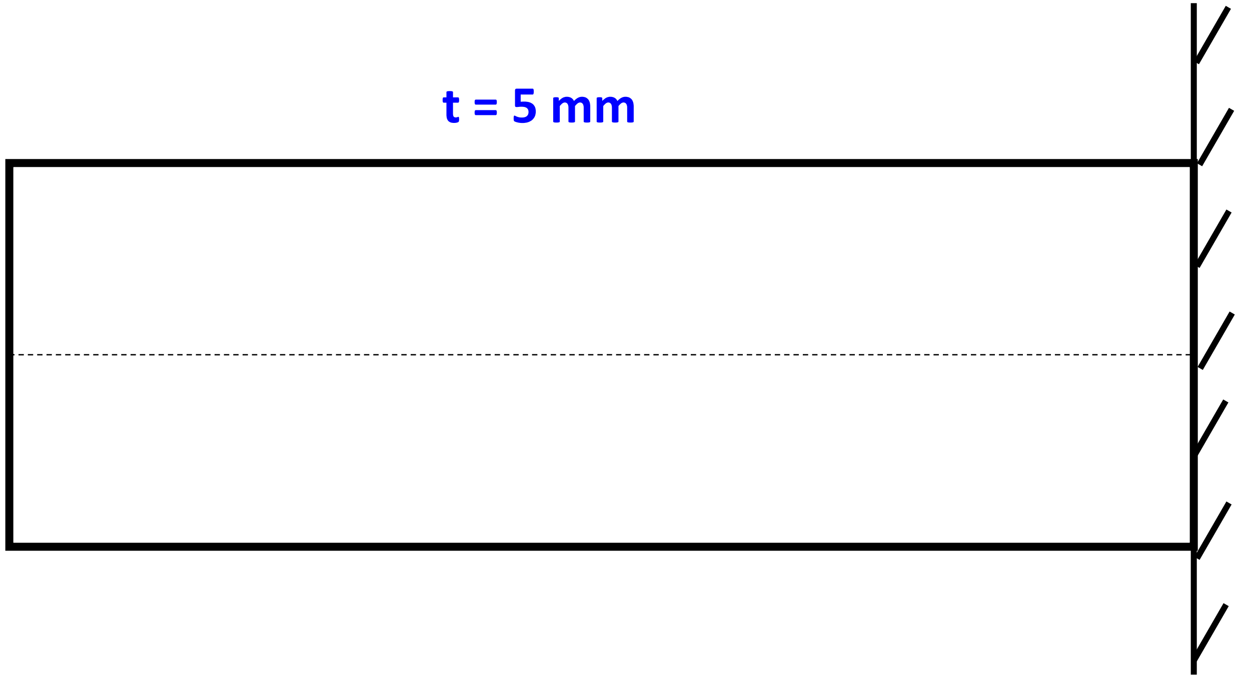

- **ASSEMBLY;**

- **STEP:** Static, General (time = 1 s); Nlgeom: OFF;

Exercise 1 – Cantilever Beam

- **LOAD:** BC – encastre; Concentrated Force = 1000 N;

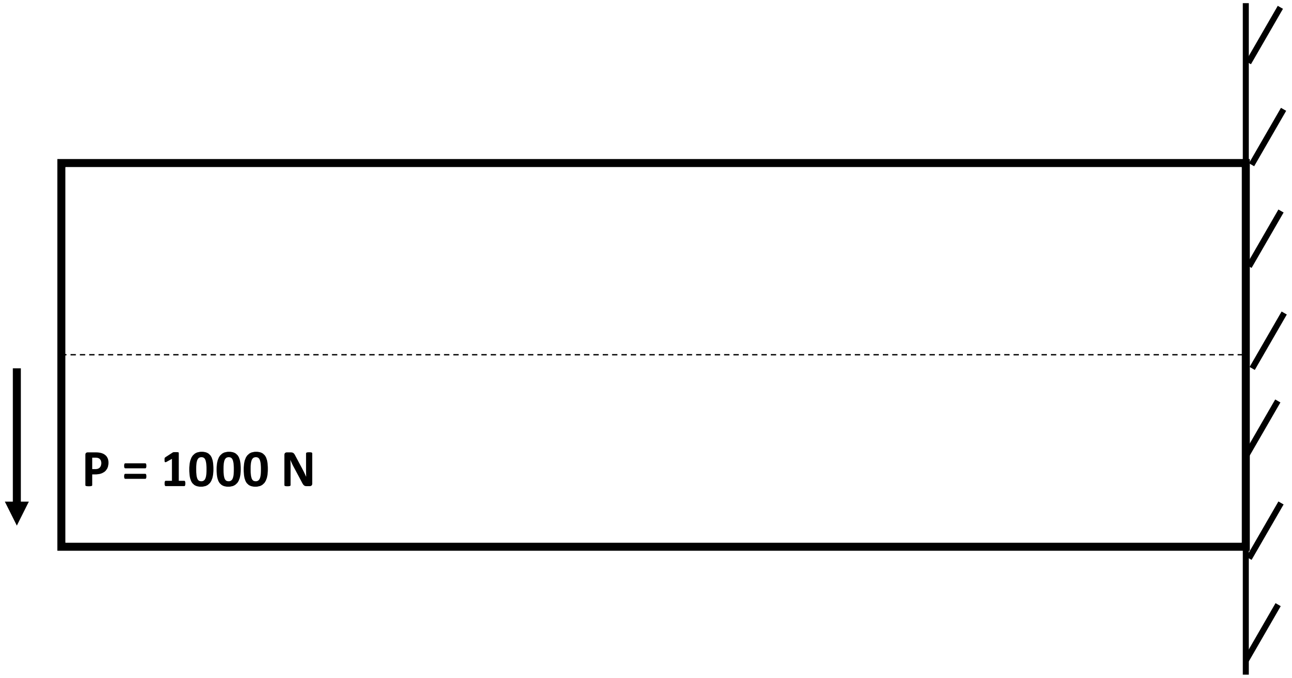

- **MESH:** Triangular Element – Structured Mesh;

Global Size = 5 mm.

Exercise 1 – Cantilever Beam

- **JOB:** Exercise_01

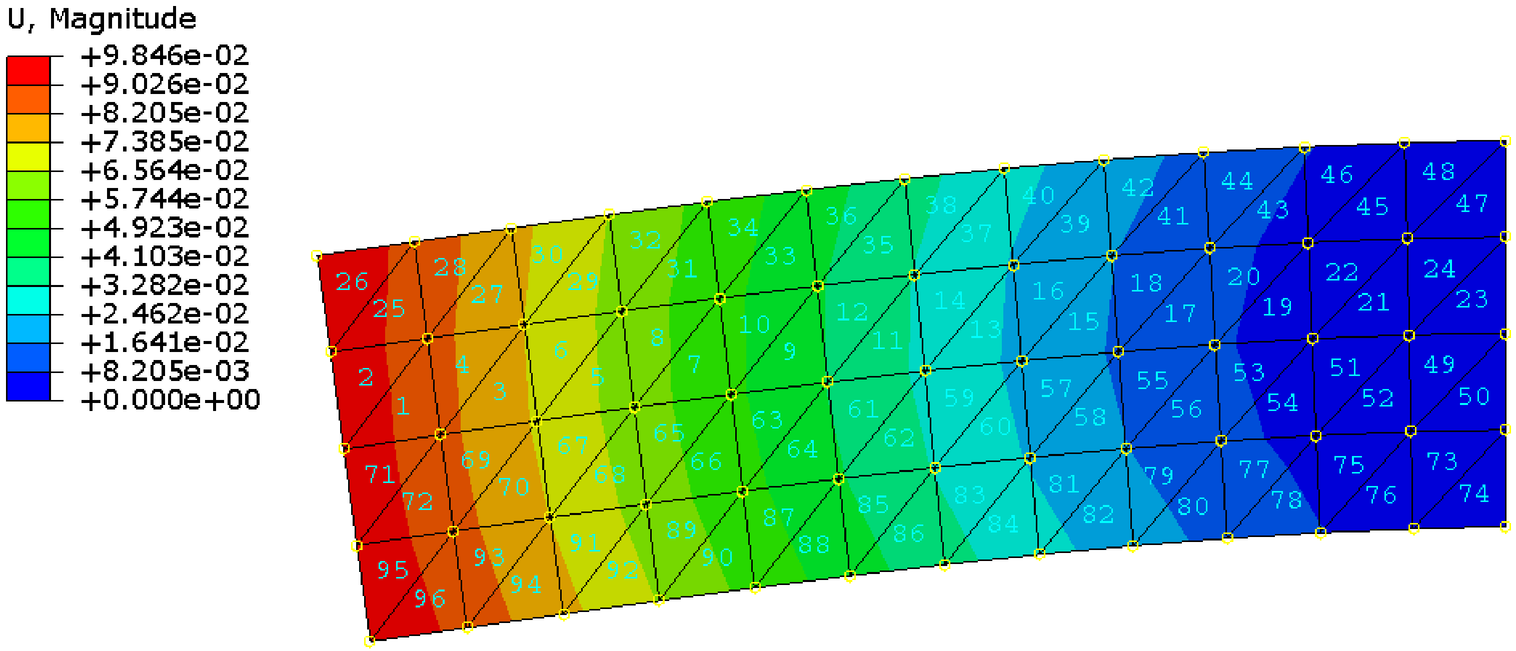

Report: Field Output (RF and U).

Exercise 2 – Plasticity

- **PART: Bar -** 2D – Deformable – Shell

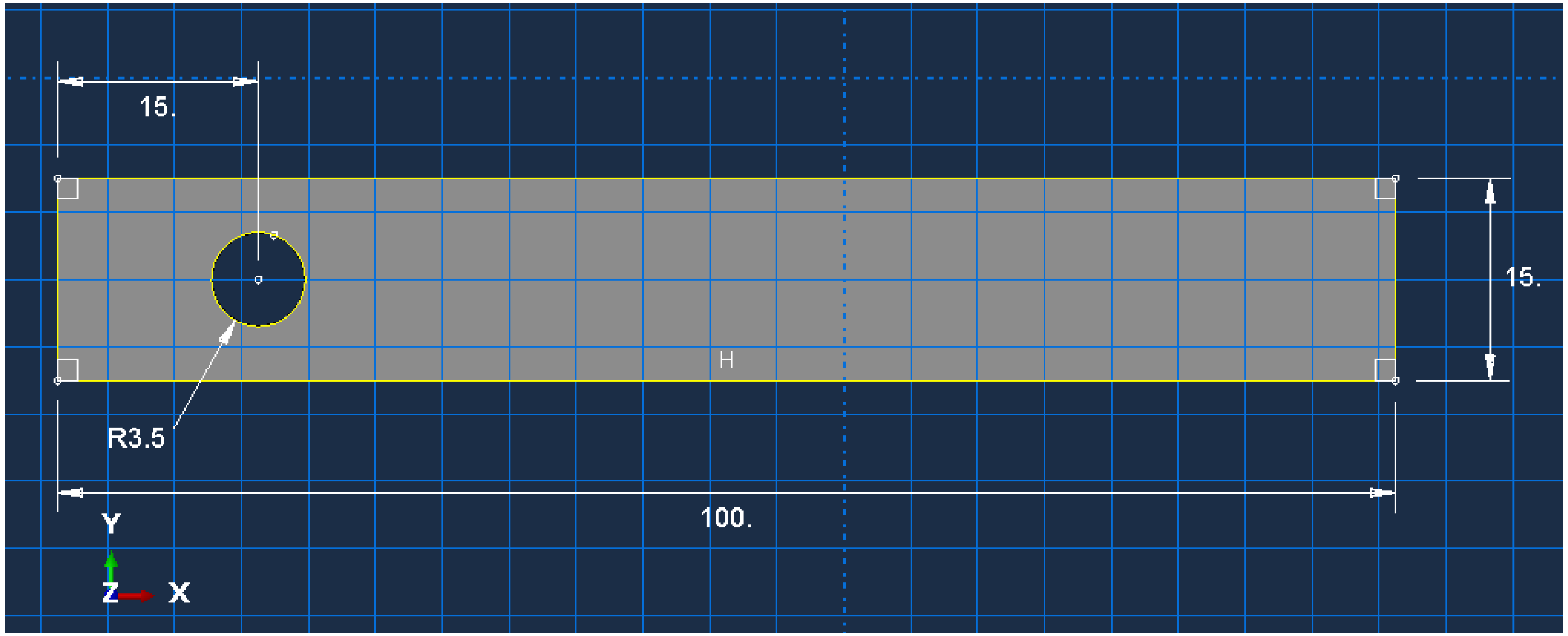

Exercise 2 – Plasticity

➢ **PROPERTIES: Steel**

Elastic: E = 210.73 GPa; $\nu = 0.29$;

Plastic:

Yield Stress	Plastic Strain
200.2	0
246	0.02353
294	0.0474
374	0.09354
437	0.1377
480	0.18

Thickness (Plane Stress): 5 mm;

➢ **ASSEMBLY;**

Exercise 2 – Plasticity

- **STEP:** Static, General (time = 1 s); Nlgeom: ON;

Initial Increment size = 0.05

Maximum Increment size = 0.2

Field Output:

Frequency – Every x units of time: 0.01 (100 frames).

Exercise 2 – Plasticity

- **LOAD:**

- **MESH:**

Element Type: CP4S (Plane Stress)

Controls: Quad mesh – Medial Axis

Global Size: 2

Exercise 2 – Plasticity

- **JOB:** Plasticity

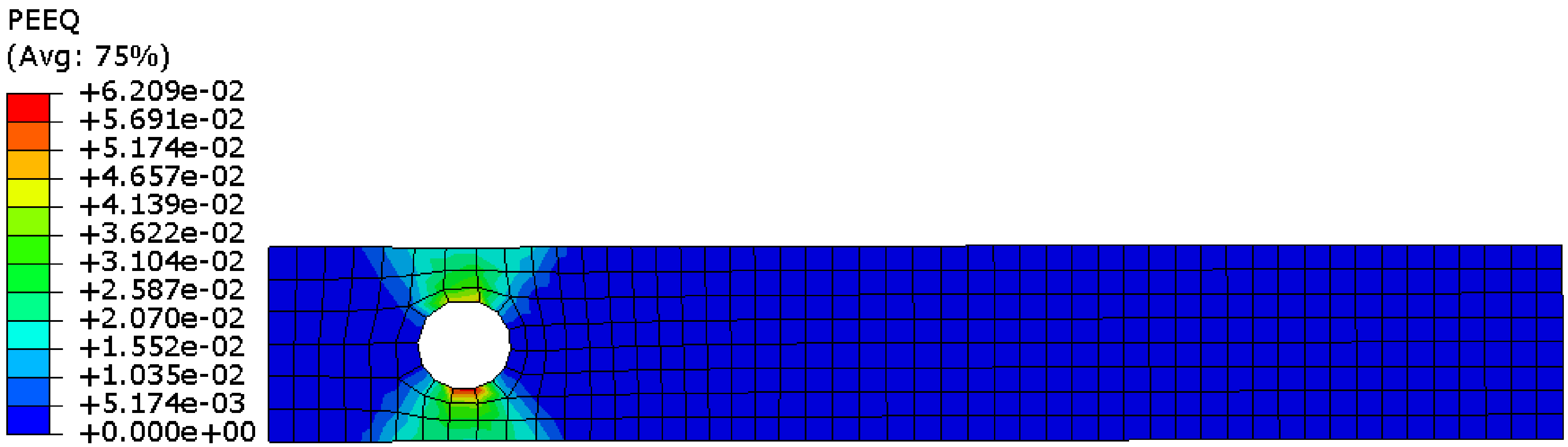

Report: PEEQ

FEM Macroscale

- **PART 1:**

Workpiece - 3D – Deformable – Solid

20 x 20 x 200 **m³**

Roller - 3D – Discrete Rigid – Solid – Extrusion

$\emptyset\ 100\ m$

Depth = 45 m

Create Reference Point (Tools).

- **PROPERTIES: Workpiece - Steel**

Elastic: E = 200 GPa; $\nu = 0.3$;

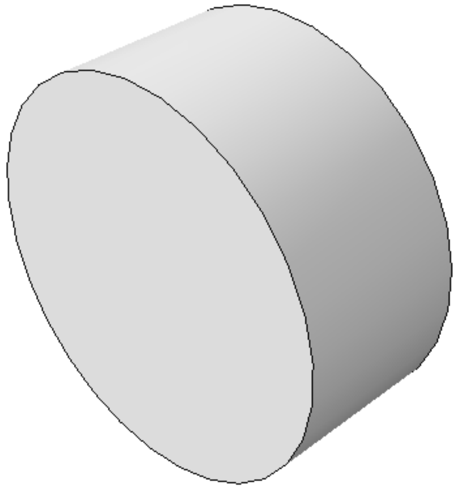

- **PROPERTIES: Workpiece - Steel**

Plastic:

Yield Stress	Plastic Strain
380e6	0
420e6	0.04
470e6	0.12
500e6	0.19
530e6	0.25

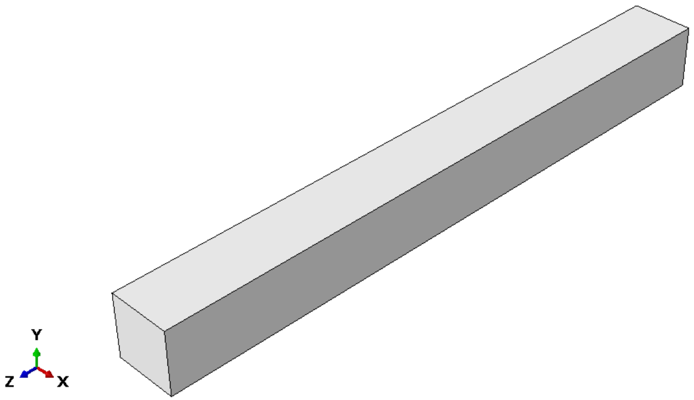

Izabel Machado – machadoi@usp.br

FEM Macroscale

- **ASSEMBLY:**

Rotate and Translate the Workpiece

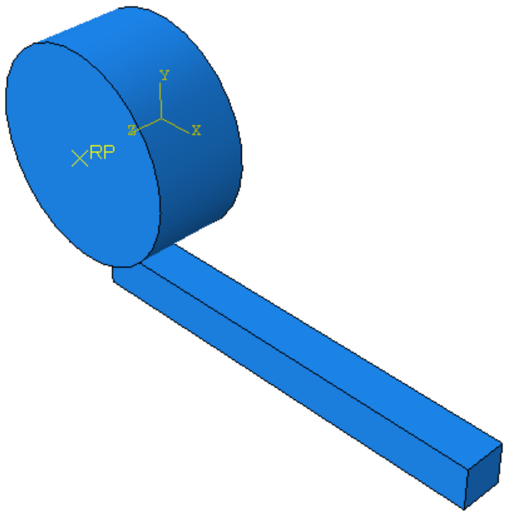

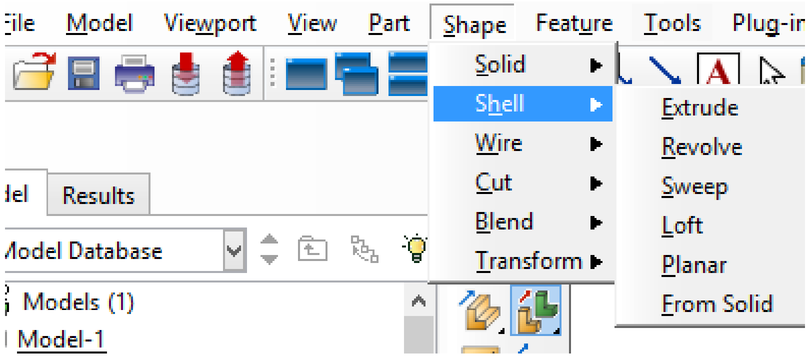

- **INTERACTION:**

Surface-to-surface;

Penalty: COF = 0.3;

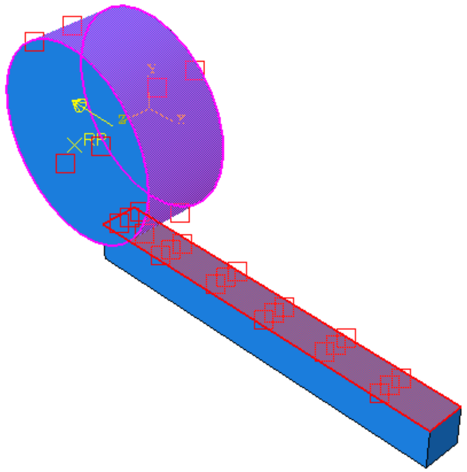

FEM Macroscale

- **LOAD:**

Workpiece

Pre-defined field (V_1 = - 70 m/s);
ZSymm;
YSymm.

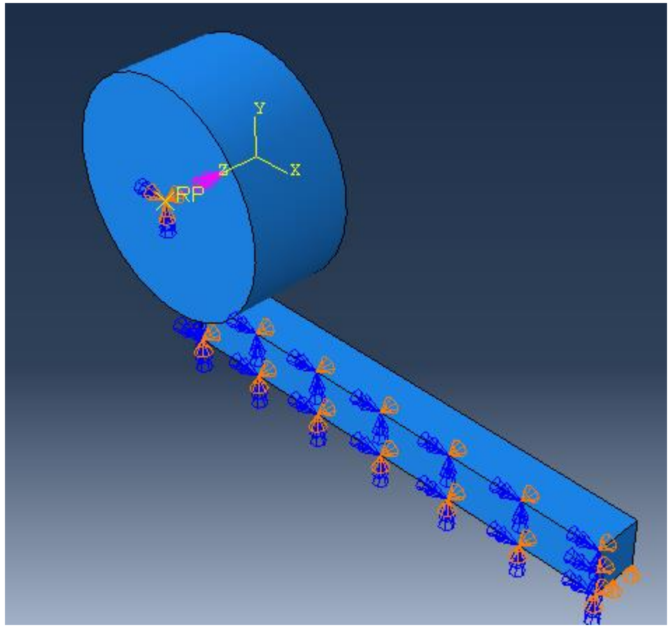

RP – Roller:

Initial Step - $U_1 = U_2 = U_3 = UR_1 = UR_2 = 0$
Step -1: VR_3 = -5 rad/s

- **MESH:**

Workpiece: Hex (C3DR8) – Global Size: 3;

Roller: R3D4 – Global Size: 3;

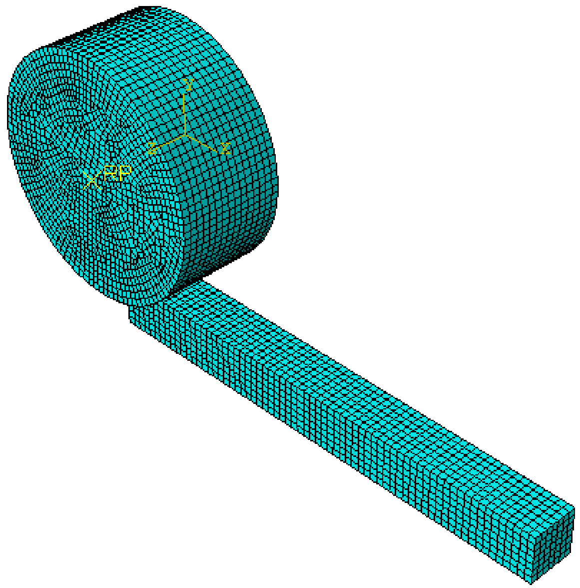

FEM Macroscale

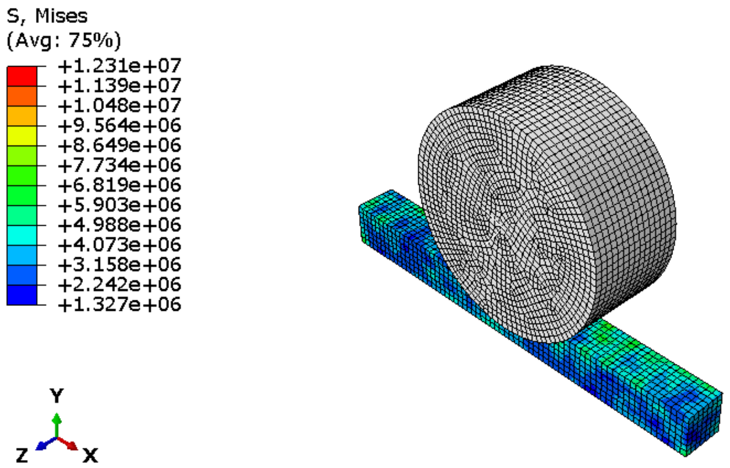

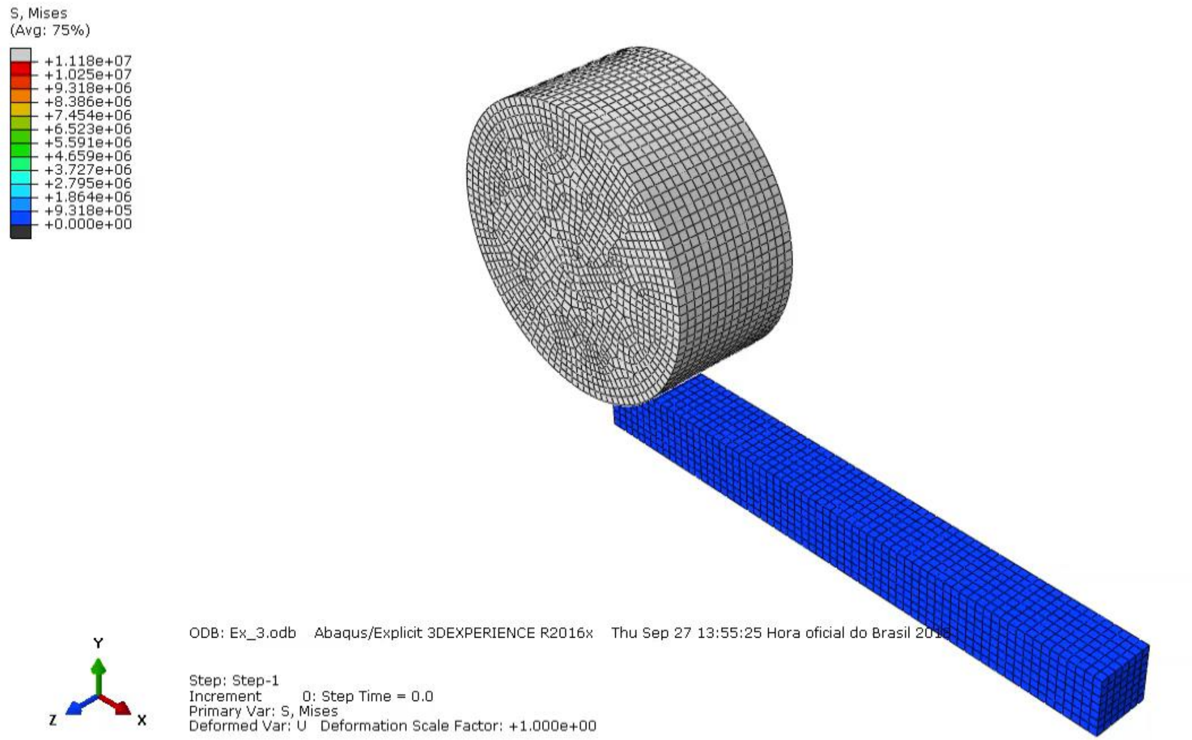

Mechanical and Tribological (Micro) Behavior Assessment using Finite Element Method Tools

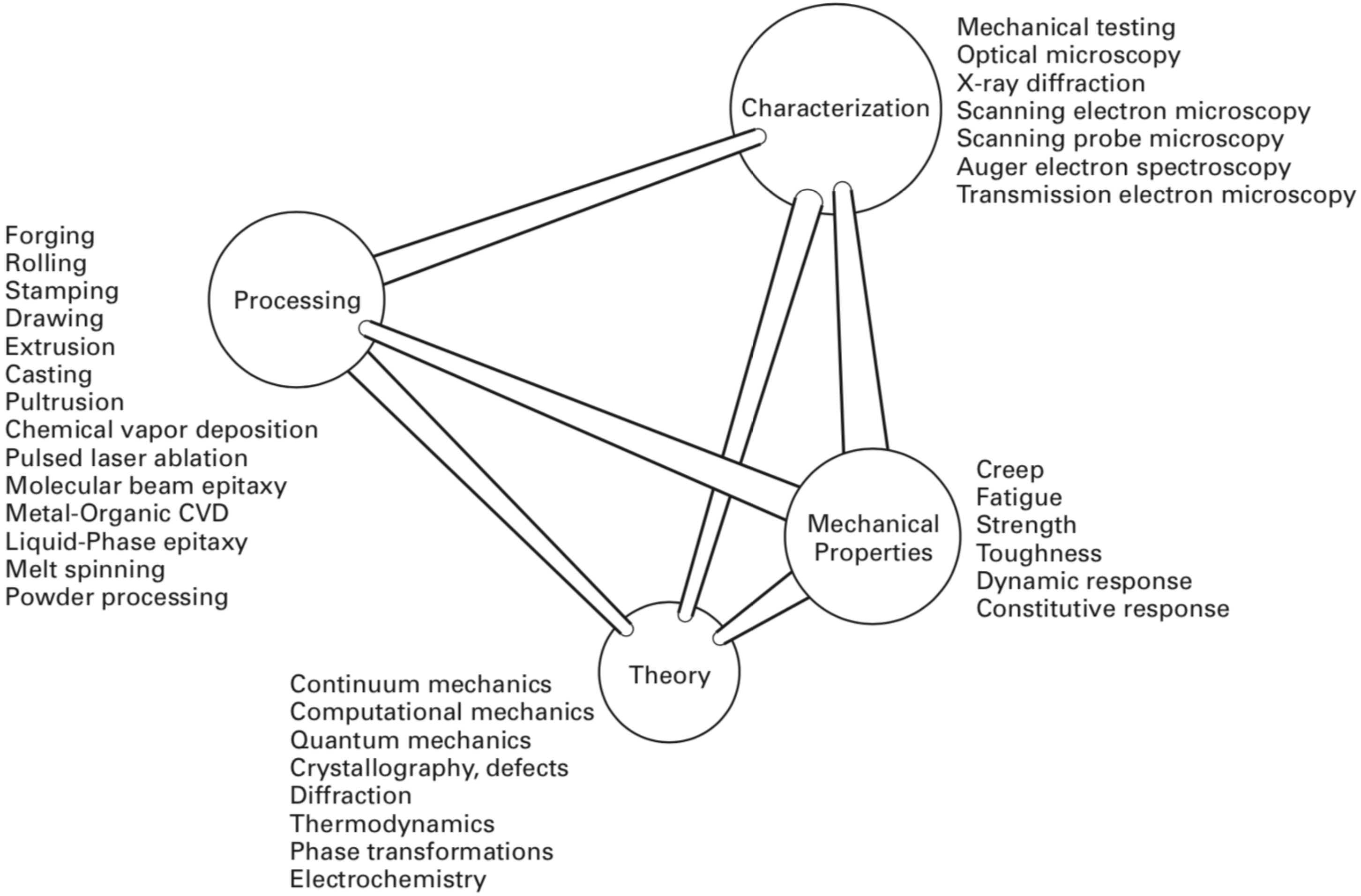

Meyers and Chawla, Mechanical behavior of Materials , 2009

Stress constrains that can cause failure!

Basic types of deformation and failure (Dowlling, 2012)

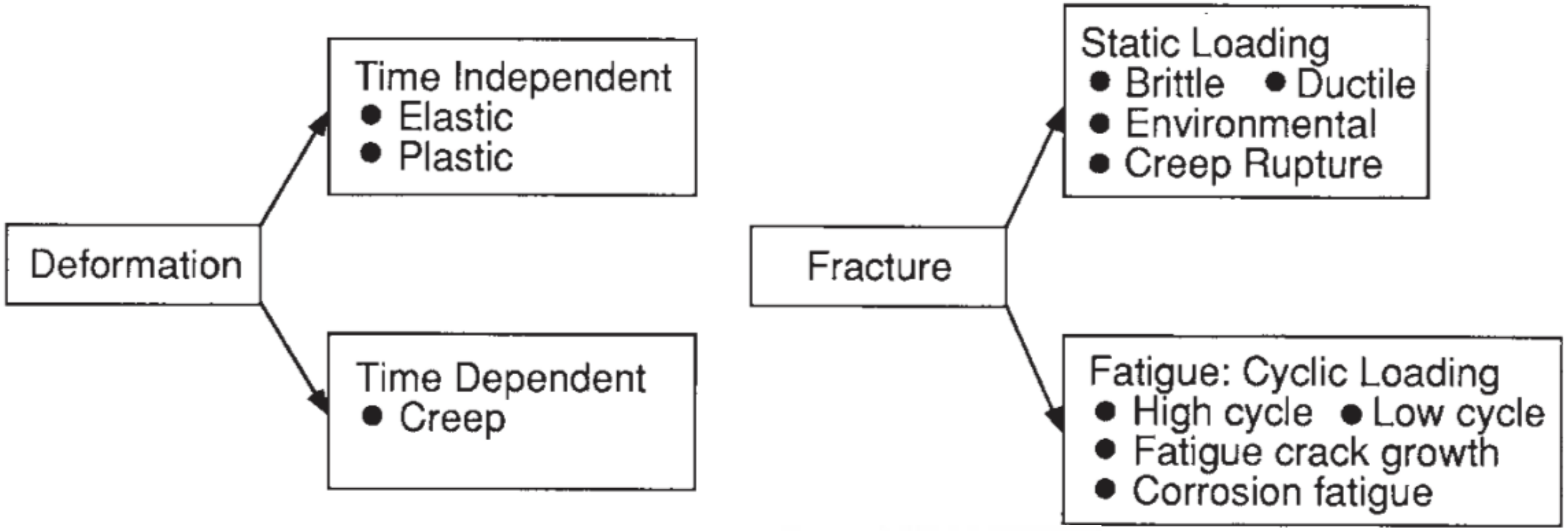

How can we connect all possible mechanisms and conditions ???

Knowledge, characterization, experiments models and computational tools …

And the effect stress constraints influence on damage

Mechanical Approach X Metallurgical/Materials Approach

1. **Materials are usually considereded homogenous and isotropic**
2. Plastic deformation is based on **tension tests**
3. Failure is based on the onset of deformation (Von Mises criteria) – Principal stresses
4. State of strain and stress are evalueted
5. Strain rate and **constitutive equations** such as Johson-Cook are importante to describe the mechanical behavior
6. Damage is mainly evaluated during crack growth - Macro
7. Focus on Design of components

1. **Materials are usually considereded heterogeneuos and anysotropic**
2. Plastic deformation is based on **dislocations teory**, crystaline structure
3. State of strain and stress were not usually considered
4. Damage are based on ductile or fragile behavior (nucleation)
5. Microstructural Characterization (Nano and Micro levels) is an important tool
6. Mechanical behavior (mechanical properties and processing) – Micro
7. Focus on Design of Materials

FEM Microescale

CAD, Parameters, MICROSTRUCTURE

X-Ray Tomography : resolution, density of phases

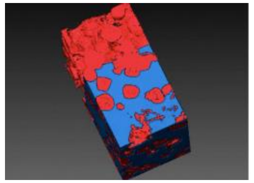

https://commons.wikimedia.org/wiki/File:Micro_CT_analysis_of_Ti2AlC_and_Al_composite.gif

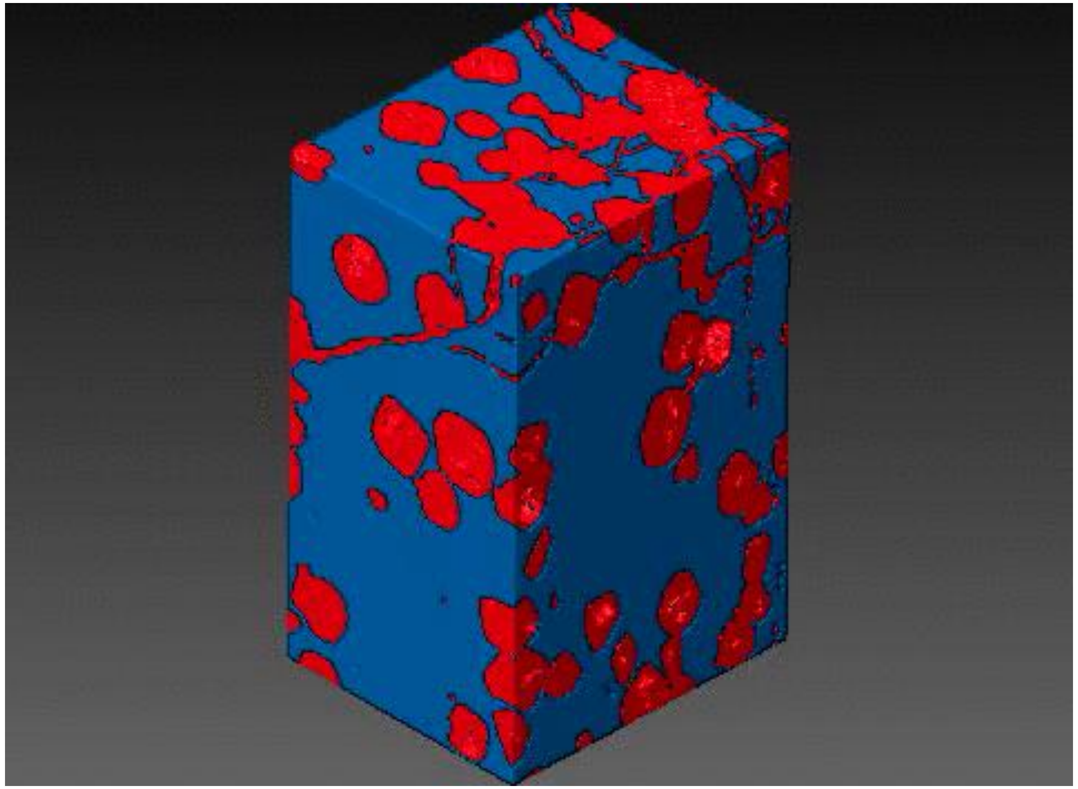

FEM Microescale

CAD, Parameters, MICROSTRUCTURE

Softwares

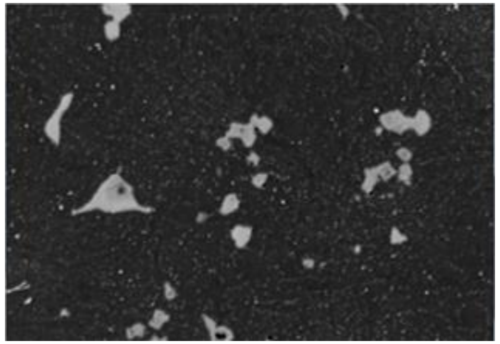

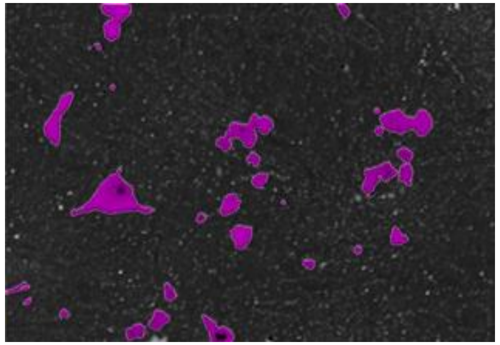

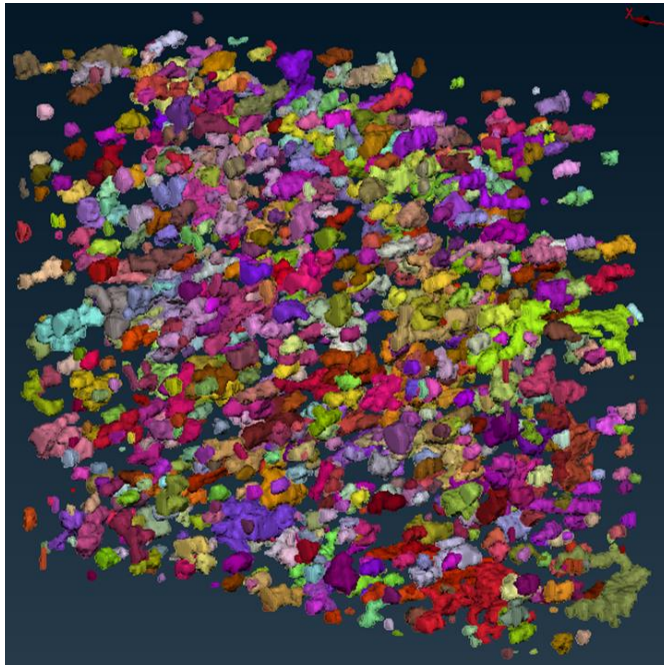

Izabel Machado – machadoi@usp.br

FEM Microescale

CAD, Parameters, MICROSTRUCTURE

Softwares

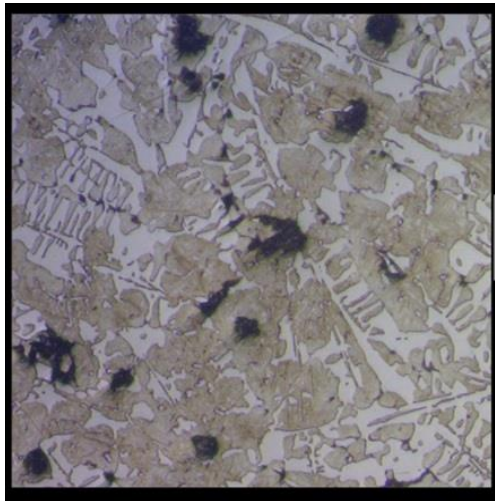

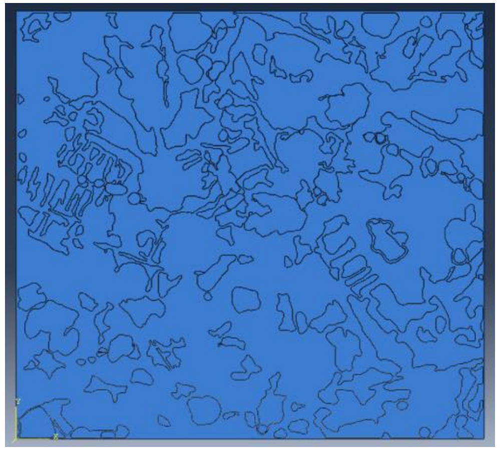

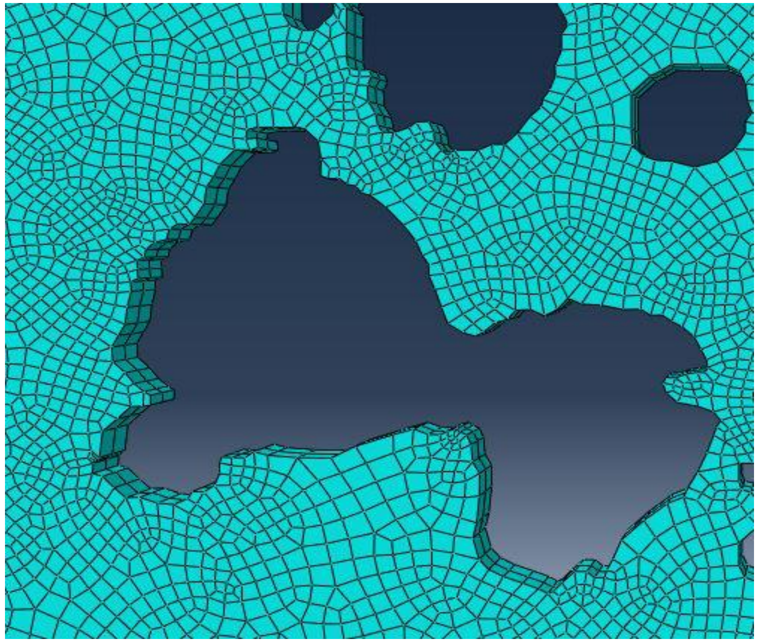

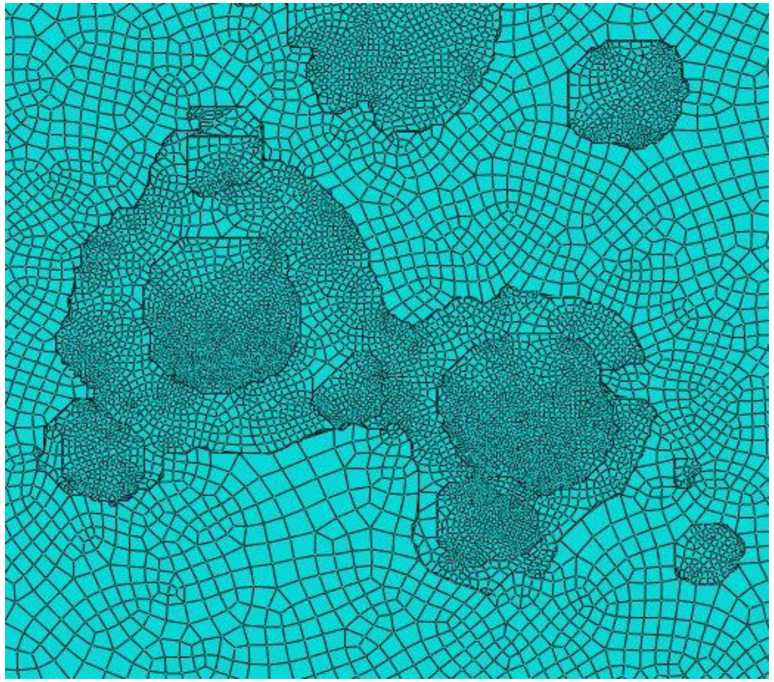

Izabel Machado – machadoi@usp.br

Mechanical and Tribological (Micro) Behavior Assessment using Finite Element Method Tools

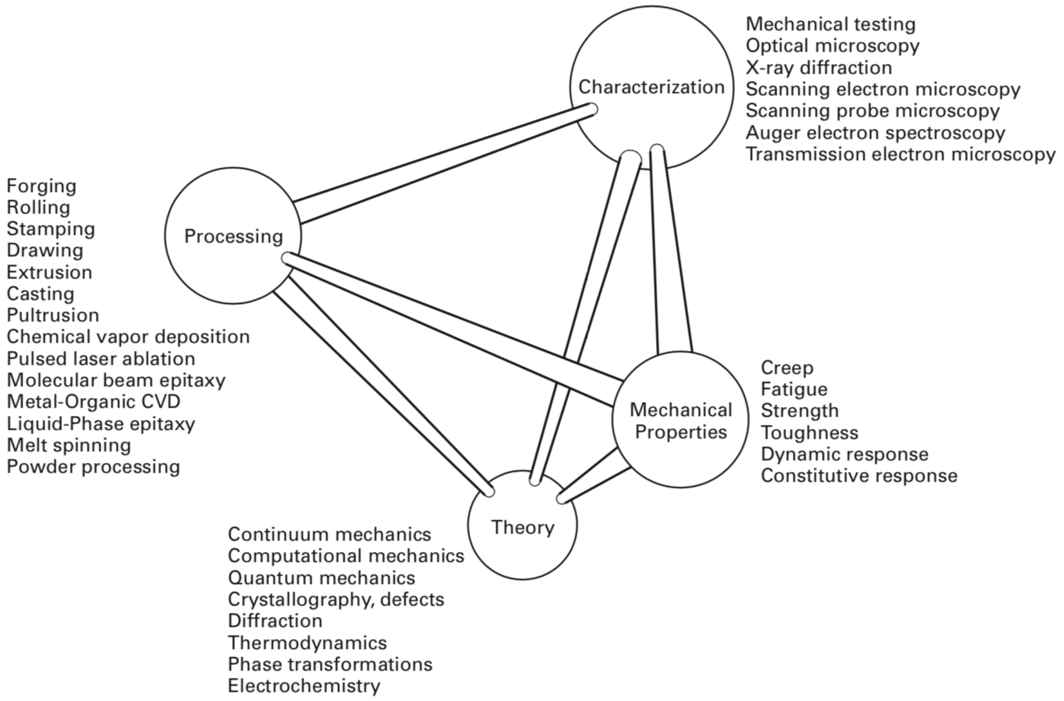

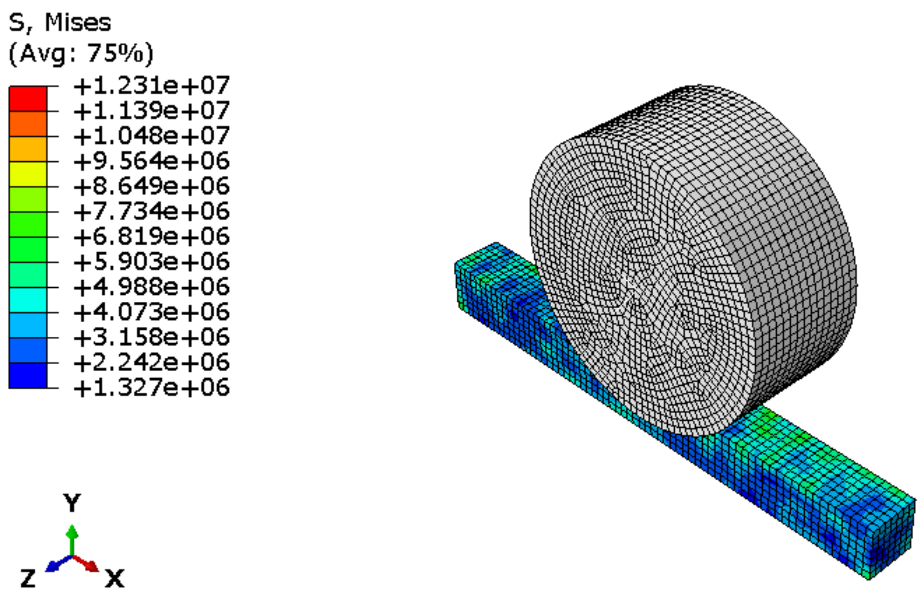

Meyers and Chawla, Mechanical behavior of Materials , 2009

1

Finite element analysis of the effects of thermo-mechanical T loadings on a tool steel microstructure

V. Seriacopi, N.K. Fukumasu, R.M. Souza, I.F. Machado, Engineering Failure Analysis , https://doi.org/10.1016/j.engfailanal.2019.01.006

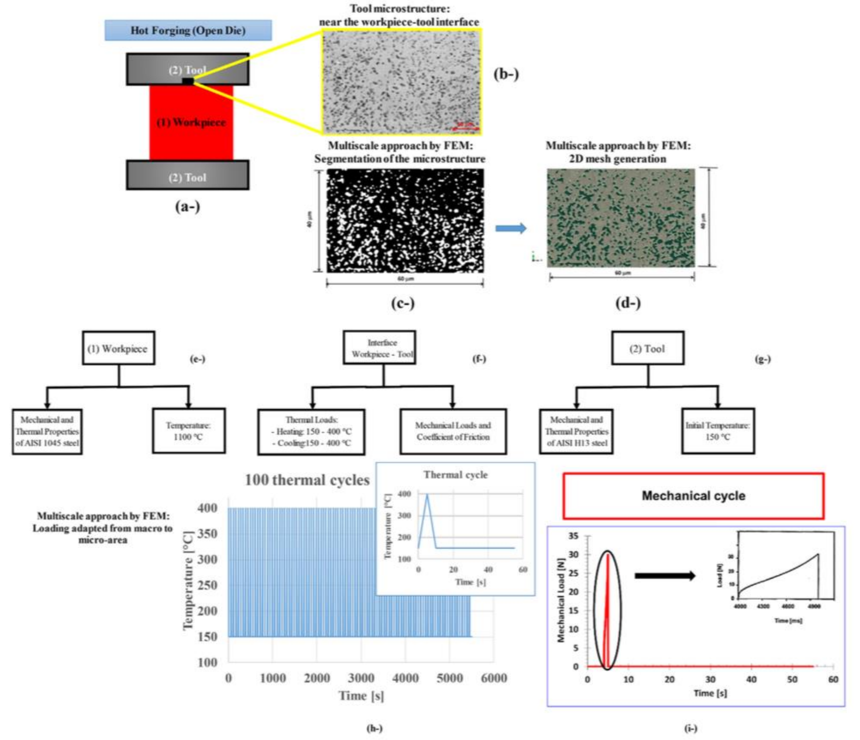

Fig. 1. Schematic representation containing the assumption of the micro-analyses conducted from the macroscopic system, mainly focused on the hot forging tool. Simplified frames are provided to specify the inputs of the models: purely thermal and thermo-mechanical loadings: (a-) general layout of the open die forging process, where (1) is the workpiece and (2) is the tool; (b-) microstructure of the tool steel studied; (c-) micrograph after segmentation, considering gray scales; (d-) 2D mesh assigned to the microstructural region evaluated; (e-) inputs of the numerical model regarding the workpiece – AISI 1045 steel; (f-) inputs of the numerical model regarding the interface between tool and workpiece; (g-) inputs of the numerical model regarding the tool – AISI H13 steel; (h-) thermal cycle considered on the analyses; and (i-) mechanical cycle evaluated by numerical modelling.

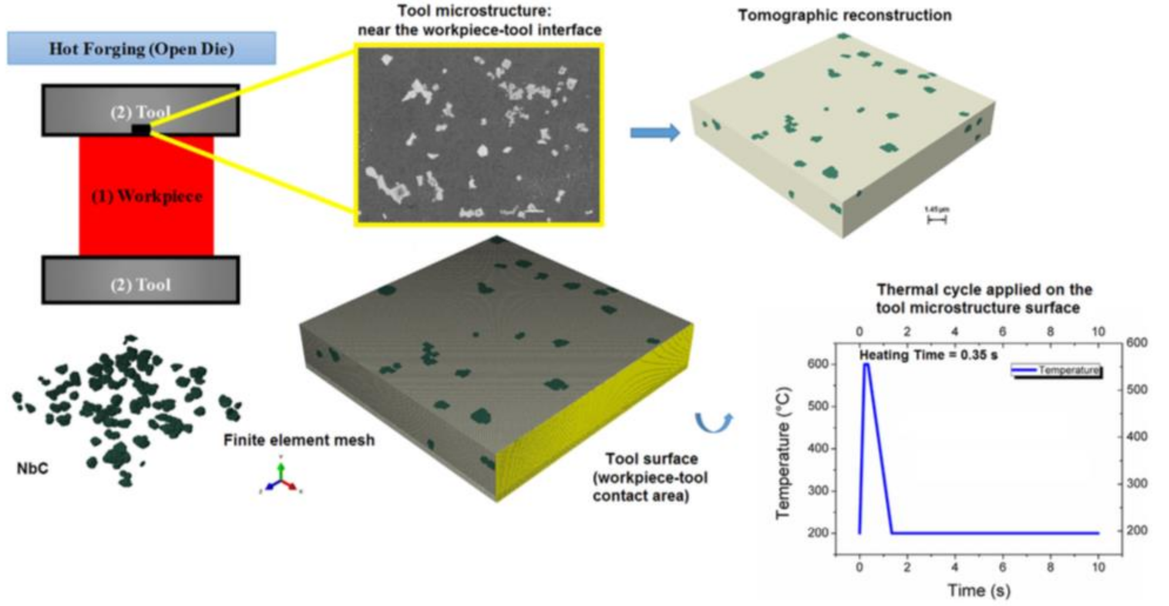

Fig. 8. Microstructure of the hot forging tool steel, consisting of martensitic matrix and niobium carbides (in green), and a detail of these carbides with the finite element mesh. Also, thermal cycle applied during the heat transfer analysis on the tool microstructure surface (yellow area) is shown. (For interpretation of the references to colour in this figure legend, the reader is referred to the web version of this article.)

Finite element analysis of the effects of thermo-mechanical loadings on a tool steel microstructure

V. Seriacopi, N.K. Fukumasu, R.M. Souza, I.F. Machado, Engineering Failure Analysis , https://doi.org/10.1016/j.engfailanal.2019.01.006

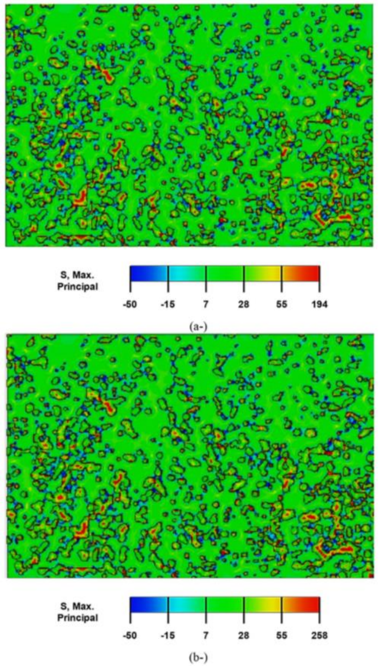

Fig. 6. Thermo-mechanical Loading results: Evolution of the results for Maximum Principal Stress [MPa] obtained during the post-cooling: (a-) First cycle; (b-) Hundredth Cycle.

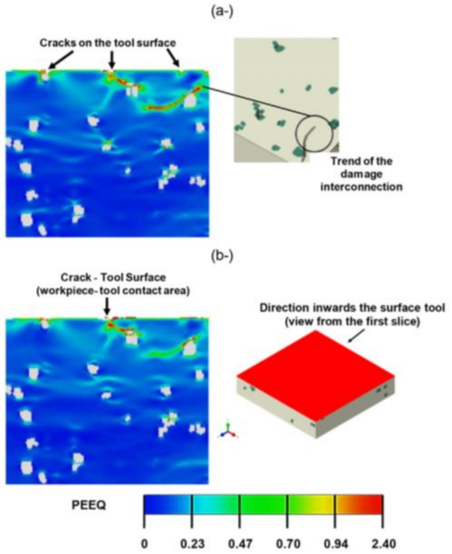

Fig. 11. View from the first slice in the direction inwards the surface tool - Equivalent plastic strain (PEEQ) field after the cooling for the following cases of NbC fracture toughness: 5 $MPam^{1/2}$ (a) and 7 $MPam^{1/2}$ (b).

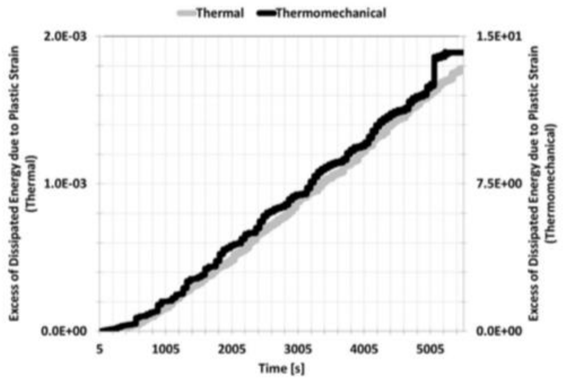

Fig. 7. Excess of the energy dissipated due to plastic strain along the time during 100 thermal cycles. This parameter was calculated from the normalized relation by 5 first seconds of heating.

2

Stress Analysis to Improve Pitting Resistance in Gear Teeth

Newton K.Fukumasu Guilherme A.A.Machado Roberto M.Souza Izabel F.Machado
https://doi.org/10.1016/j.procir.2016.02.349

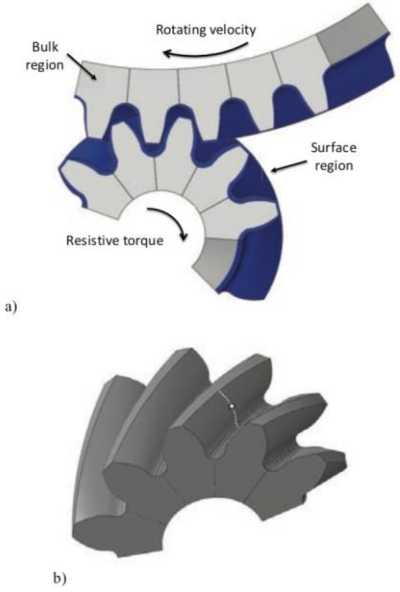

Fig. 1 – Finite Element Model of the helical gears: a) numerical model of five pairs of helical gear tooth, in which blue indicates the near surface region while the light gray indicates the bulk region of gear teeth; b) central point and path of numerical results extraction.

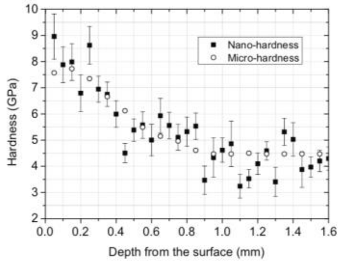

Fig. 3 – Hardness profile from surface towards the inner region of the helical gear measured by micro and nano-indentation techniques.

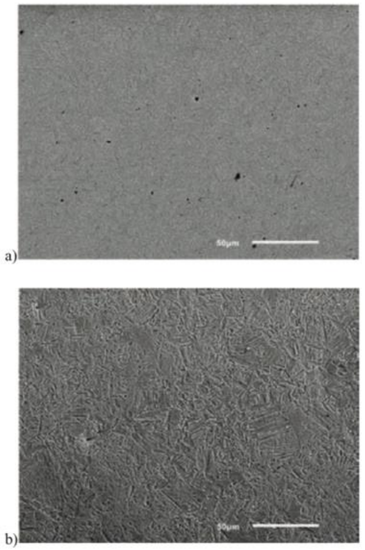

Fig. 2 – Back scattering SEM image of the microstructure of one gear tooth: a) bainitic inner region and b) martensitic surface region.

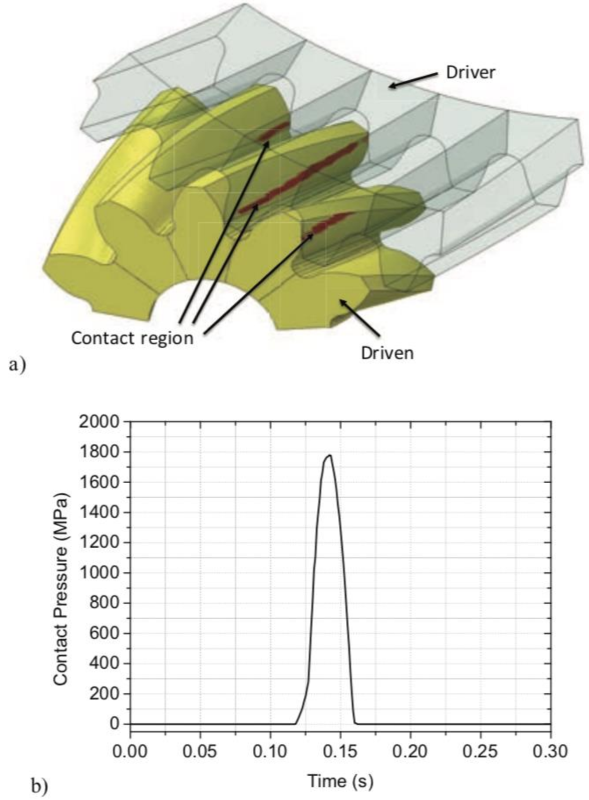

Fig. 4 – Contact in an engaged helical gear pair: a) contact region distributed in three pairs of gear tooth (red region) and b) evolution of contact pressure in the central point of the gear tooth (Fig. 1b).

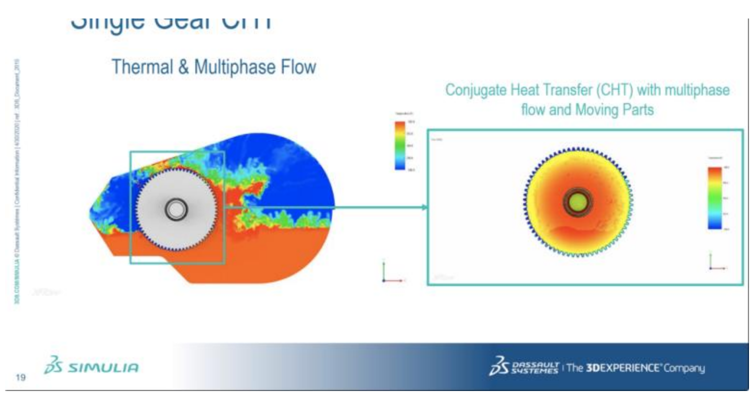

Simulação do funcionamento de engrenagens

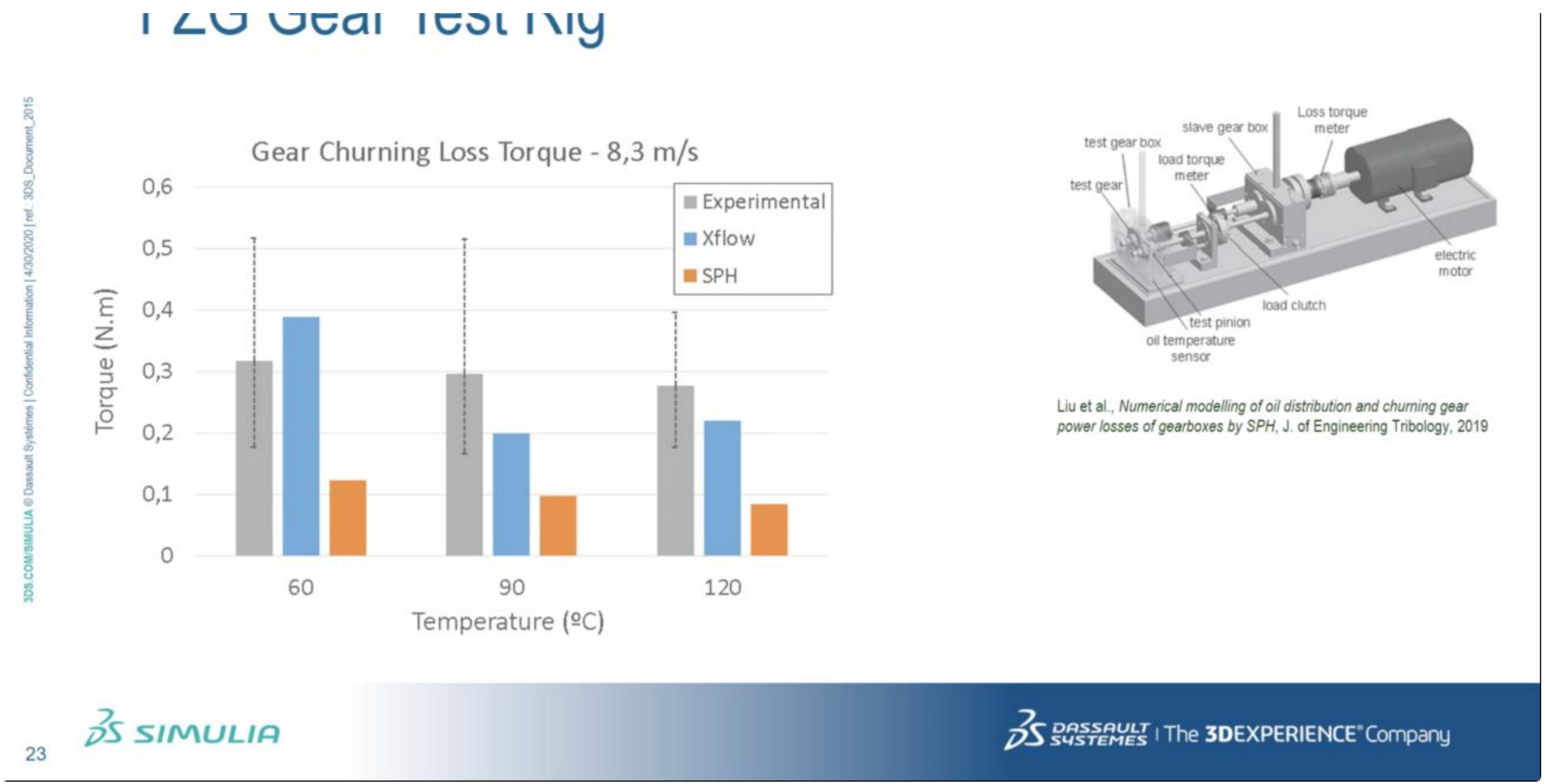

FGZ – churning losses

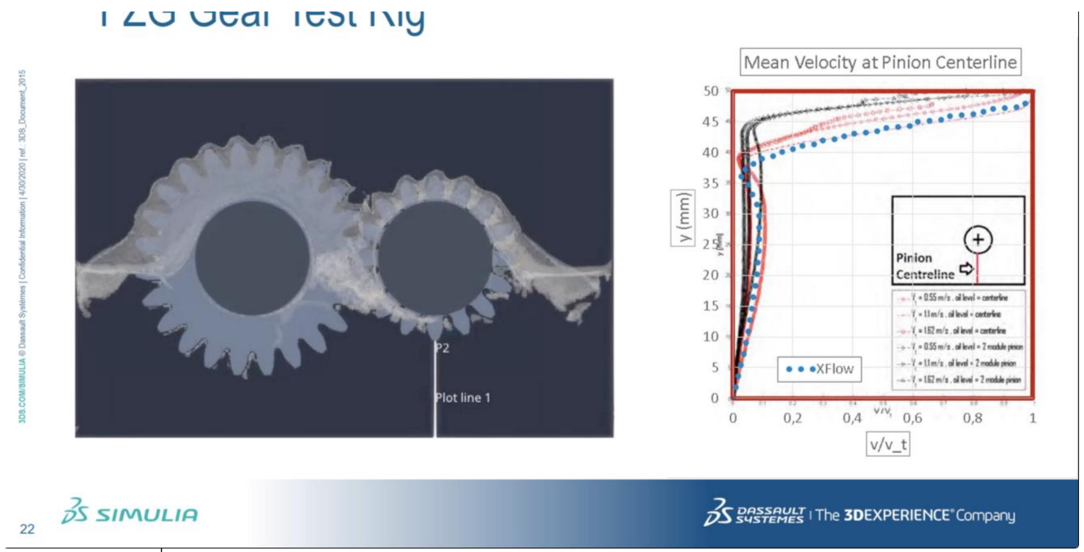

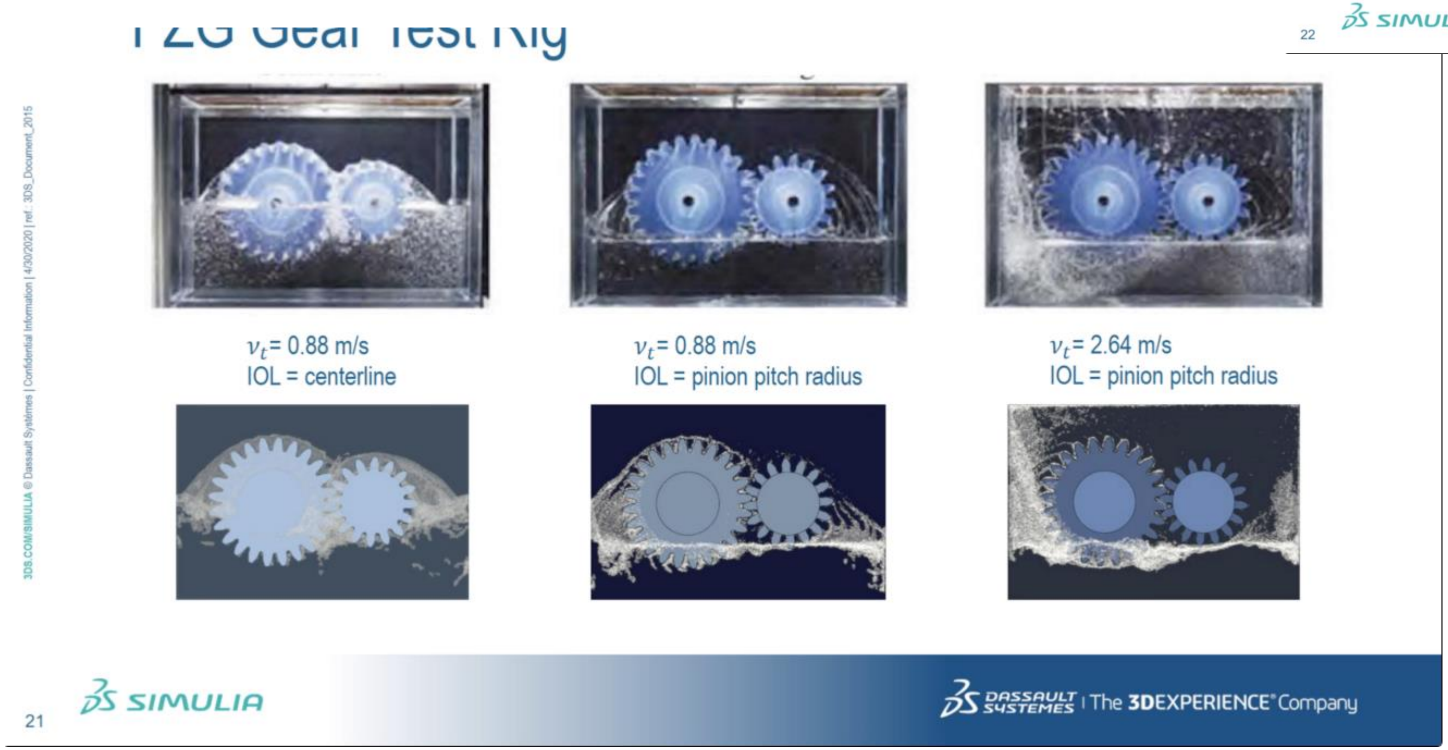

Markers – Colored by Velocity

- Markers provide an indication of where the liquid phase (oil is)
- In this animation we can see how the oil behaves and how it transitions from rest to regime

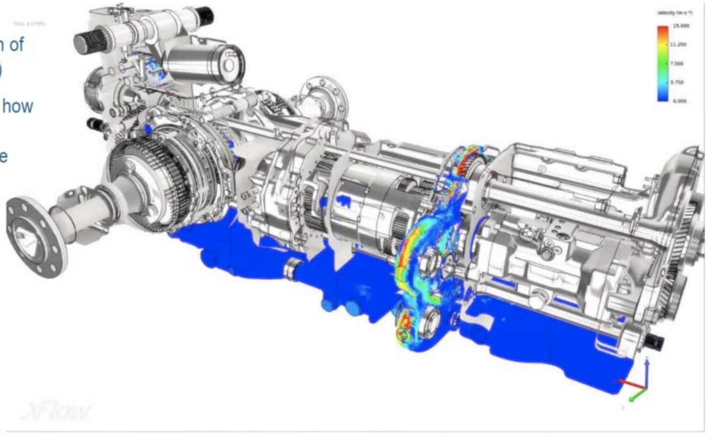

Gears Wet Surface

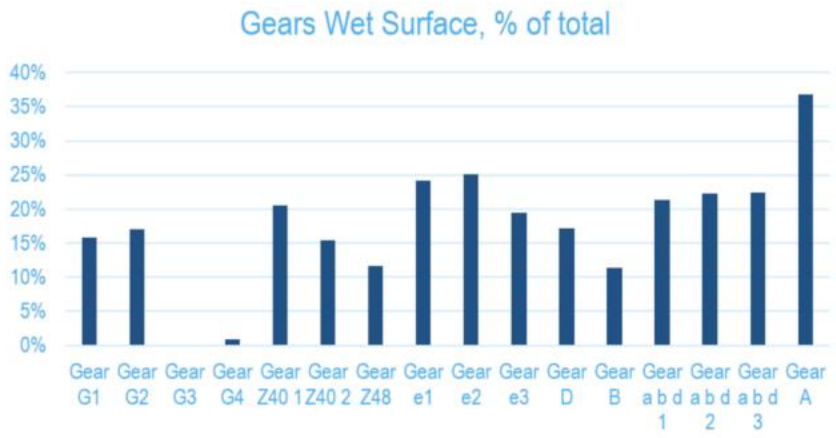

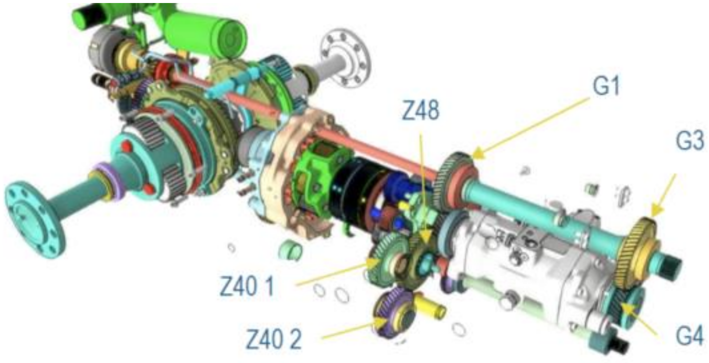

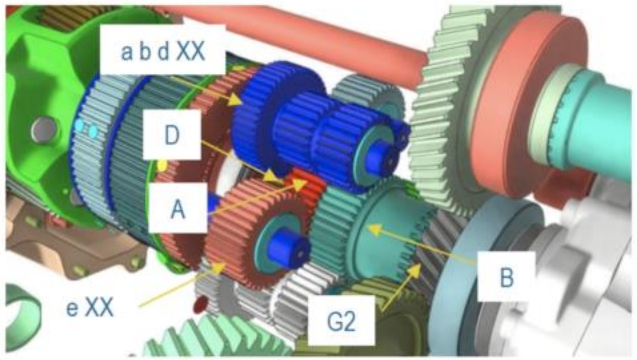

- The chart reports the % of wet surface for the rotating gears
- Note how Gears G3 and G4 are not lubricated at all

Friction evaluation during contact – manual transmission

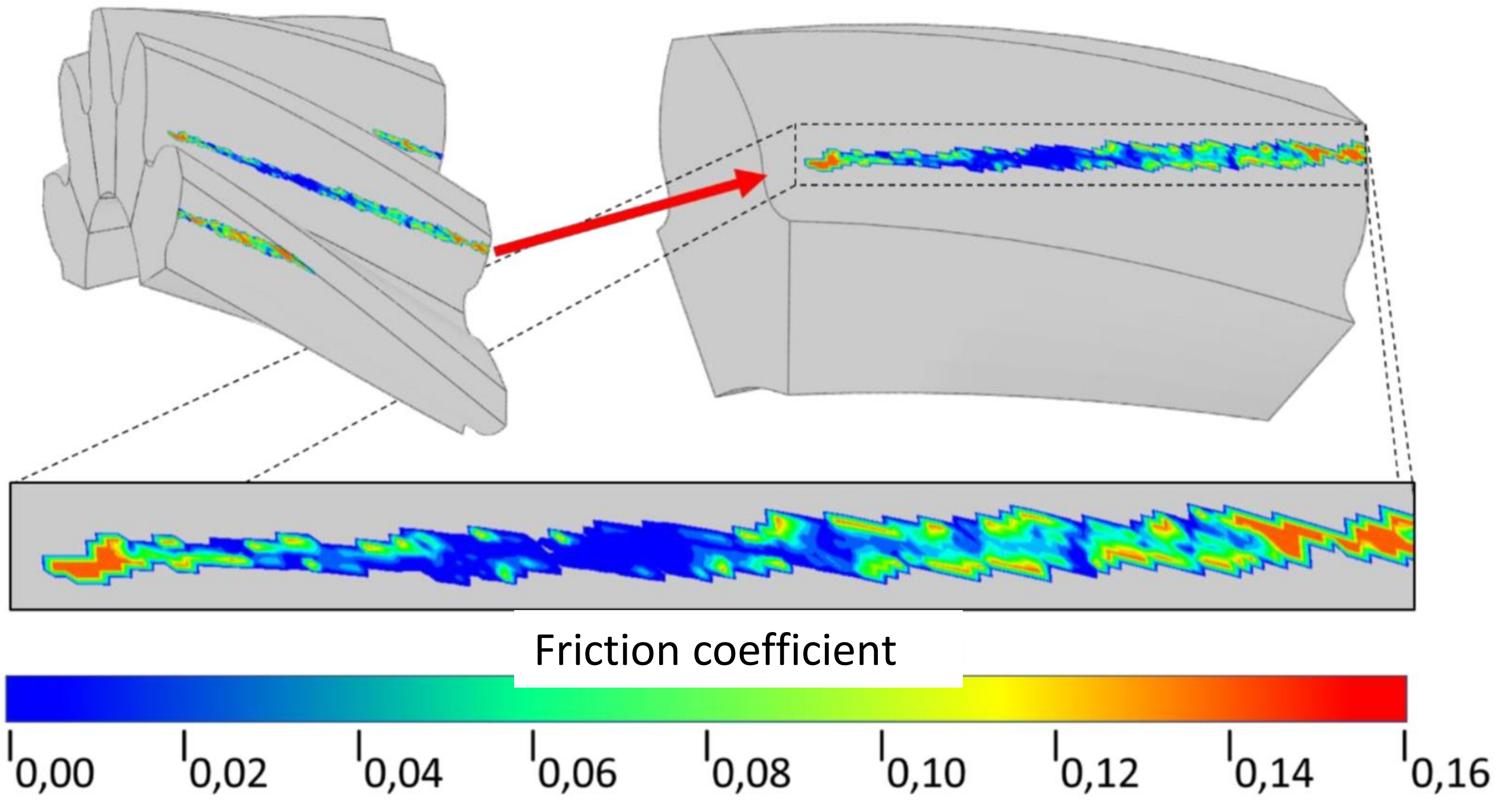

3

Experimental and numerical analysis of dry contact in the pin on disc test

E.M. Bortoleto, A.C. Rovani, V. Seriacopi, F.J. Profito, D.C. Zachariadis, I.F. Machado, A. Sinatora, R.M. Souza, WEAR.
http://dx.doi.org/10.1016/j.wear.2012.12.005

Table 2
Material properties of the pin (AISI 4140 steel) and disc (AISI H13 steel) [14].

	Material	
	AISI 4140 (wt%)	AISI H13 (wt%)
Density [kg/m^3]	7885	7800
Elastic modulus [GPa]	210	210
Poisson's ratio	0.29	0.3
Yield stress [MPa]	1370	1410

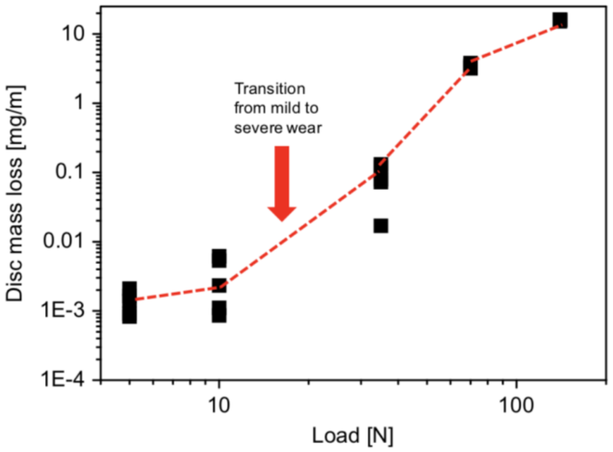

Fig. 6. Disc mass loss of the experimental results for the 5, 10 35, 70 and 140 N.

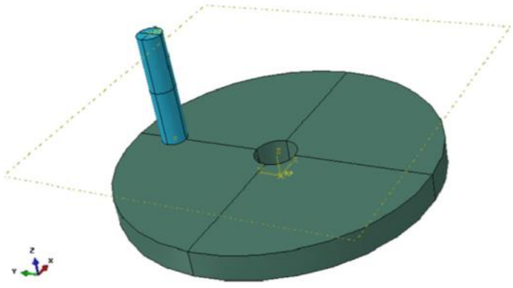

Fig. 1. Geometry of the contact pair pin on disc (tribological system).

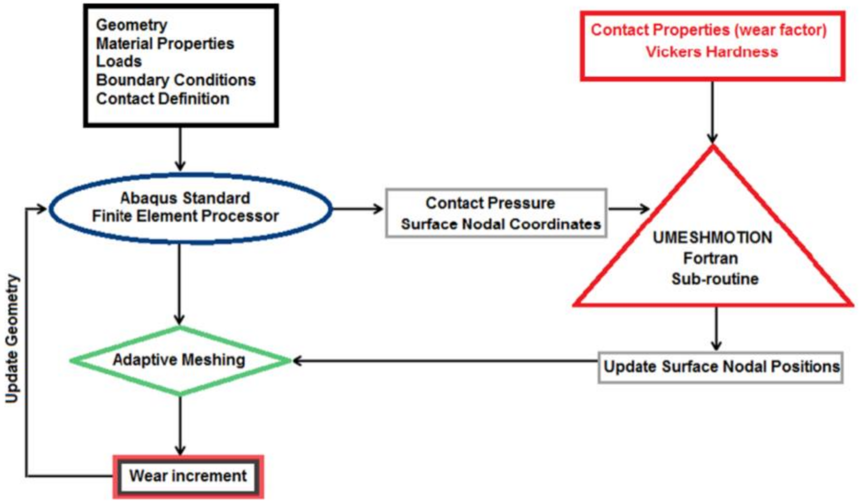

Fig. 4. Flowchart for the UMESHMOTION subroutine.

Experimental and numerical analysis of dry contact in the pin on disc test

E.M. Bortoleto, A.C. Rovani, V. Seriacopi, F.J. Profito, D.C. Zachariadis, I.F. Machado, A. Sinatora, R.M. Souza, WEAR.
http://dx.doi.org/10.1016/j.wear.2012.12.005

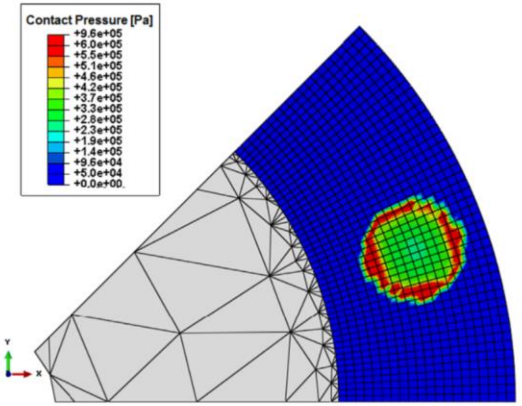

Fig. 8. Contact pressure on the disc surface during pin sliding with 10 N normal load.

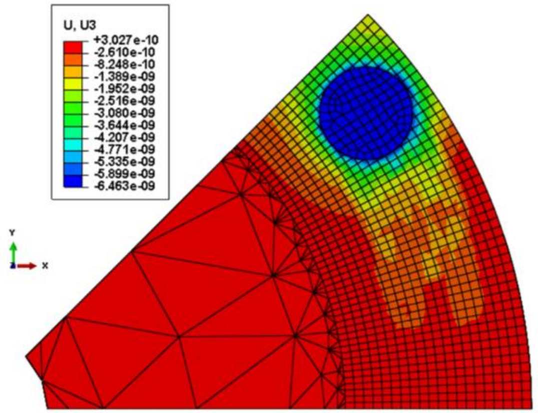

Fig. 12. Superposition of elastic deformation effects and wear after pin sliding over disc surface .

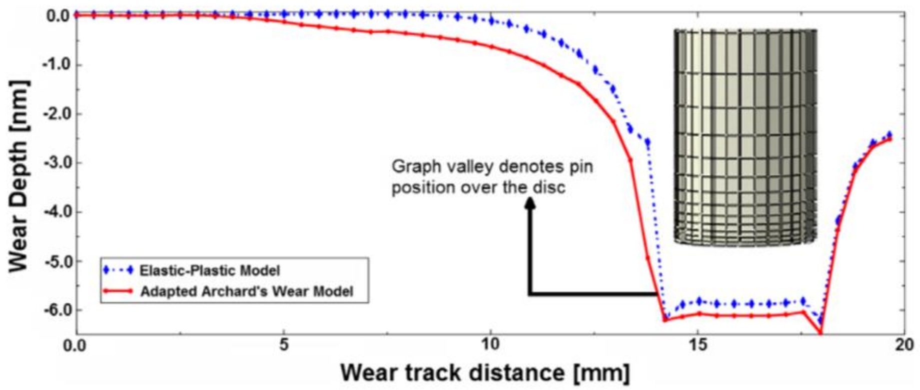

Fig. 11. Comparison between wear profile (continuous line) and elastic deformation (dashed line) during pin sliding over disc under 10 N load along movement direction.

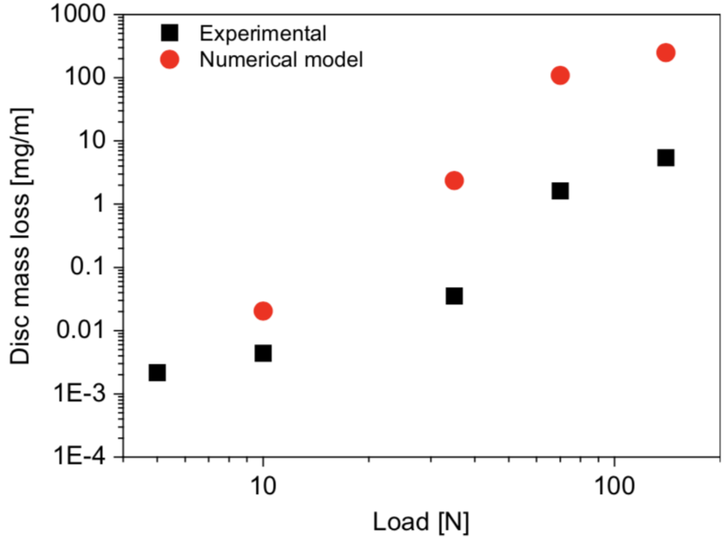

Fig. 10. Comparison between mass losses of experimental and numerical results after the sliding wear.

4

Numerical Model of Machining Considering the Effect of MnS Inclusions in an Austenitic Stainless Steel

G.M.P.Chagas, I.F.Machado
https://doi.org/10.1016/j.procir.2015.04.093

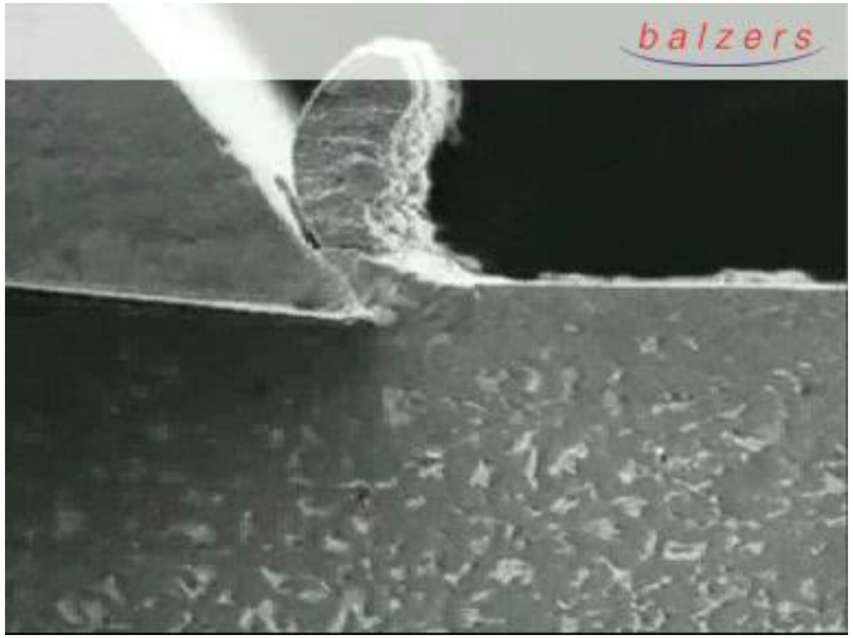

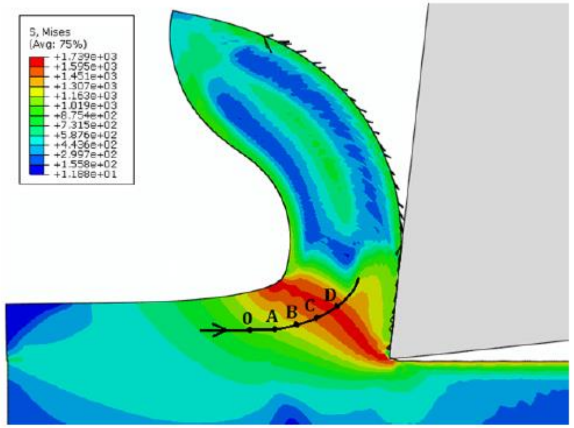

Fig. 4. Von Mises stress with positions evaluated along the flow line

Table 4. Maximum and minimum plane stress

Distance	σ_1 (MPa)	σ_2 (MPa)
0-A	59	-1267
A-B	118	-1229
B-C	470	-1151
C-D	615	-1187

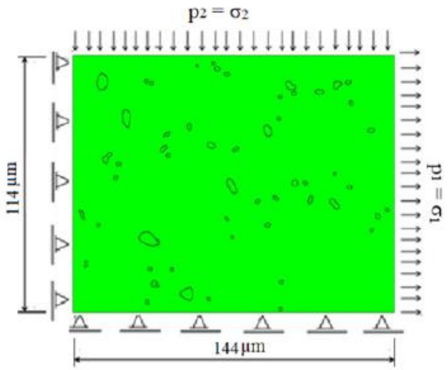

Fig.7. Microstructure boundary conditions and loads applied

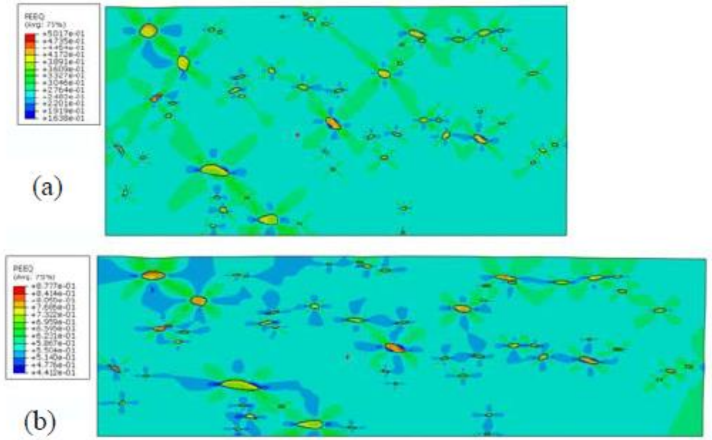

Fig. 11 Equivalent plastic strain behavior:
(a) in the instant time of 8.083 x10^{-5}s, (b) instant of time of 2.546x10^{-4}s.

5

Phenomena – Abrasion, 2D analysis

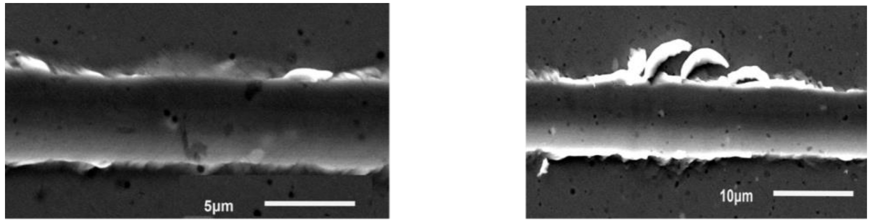

50 mN - Mechanism Transition

100 mN - Cutting

Chip formation mechanism during cutting: When the scalar stiffness degradation is unity, the material failure will occur promoting debris such as discontinuous chips agreement with the experimental results.

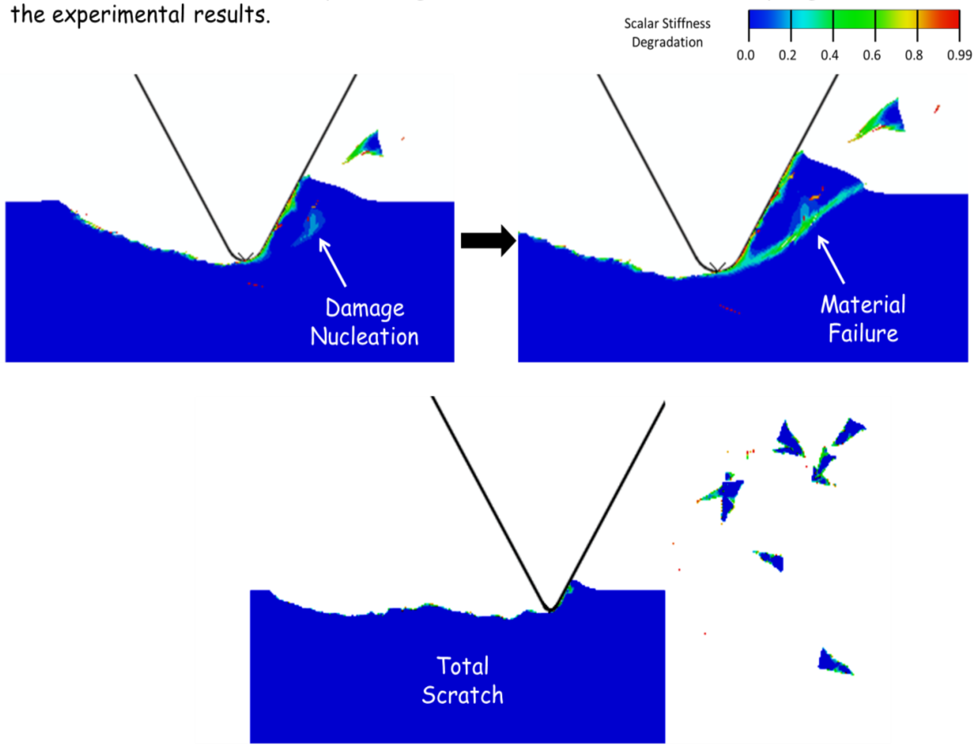

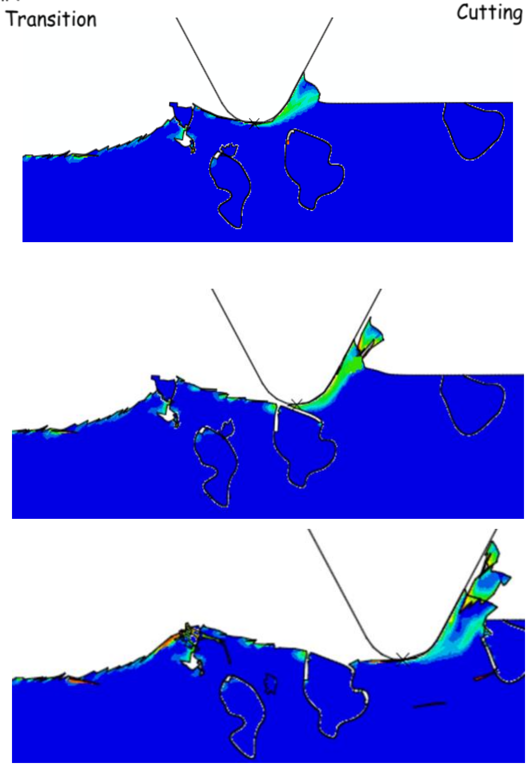

Homogeneous material

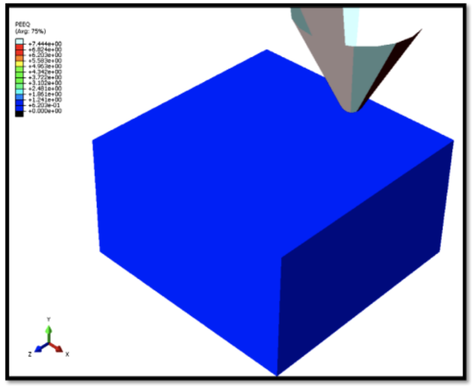

Izabel Machado – machadoi@usp.br

Analysis of abrasion mechanisms in the AISI 303 stainless steel: Effect of deformed layer

V. Seriacopi, N. K. Fukumasu, R. M. Souza, I. F. Machado

10.1016/j.procir.2016.02.326

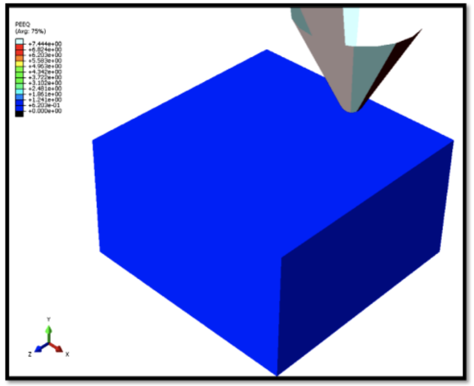

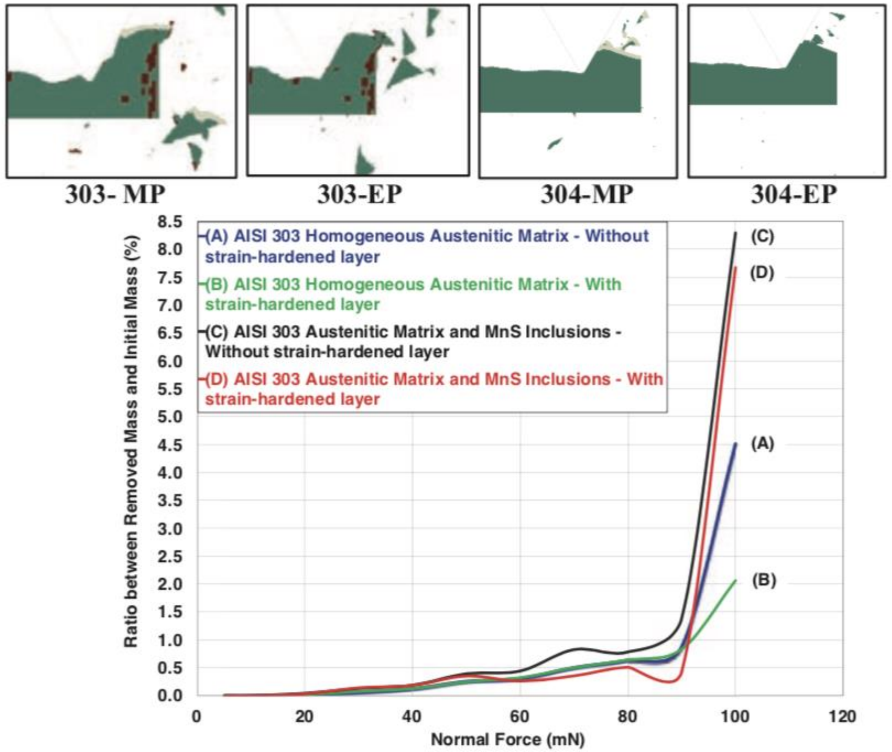

Fig. 6. Numerical results of mass removal by abrasion, obtained considering difference in surface finishing and microstructure.

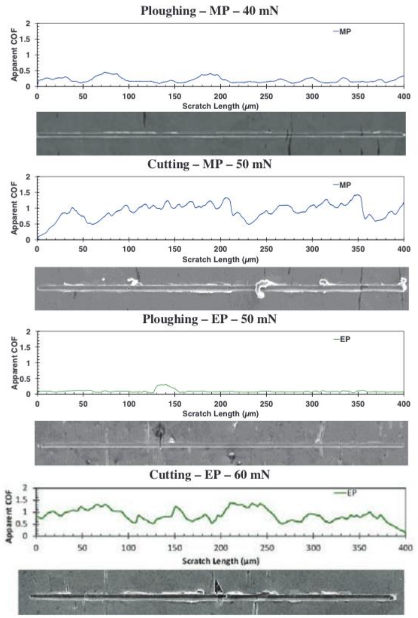

Fig. 4. Abrasion mechanism transitions characterized by SEM (secondary electrons).

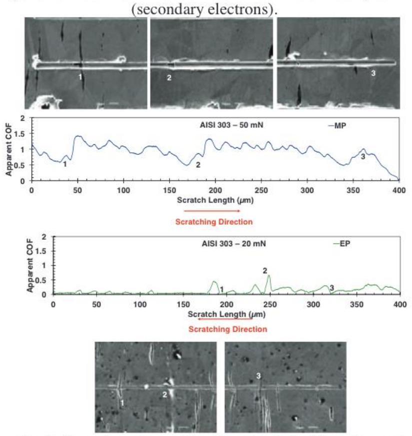

Fig. 5. Experimental results of scratch test at the microscale: details of AISI 303 microstructural behavior.

6

Vanessa Seriacopi. Evaluation of abrasive mechanisms in metallic alloys during scratch tests: a numerical-experimental study in micro-scale. 2017.

(a-) AISI 304 stainless steel: **SEM characterization was conducted to better observe the homogeneous microstructure.**

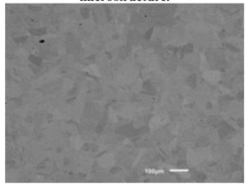

(b-) AISI 303 stainless steel: **MnS characterized using OM (elongated in the rolling direction) - Volume fraction of MnS calculated using ImageJ® software: (3.2 ± 0.4) %.**

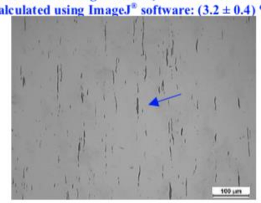

(c-) AISI 310 stainless steel: **TiN (golden color and square morphology observed using OM).**

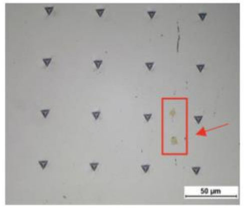

(d-) AISI H13 steel: **the tool steel metallographically etched to allow observing the martensitic matrix.**

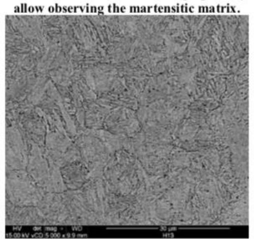

(d-) Cast alloy: heterogeneous hard material - **Volume fraction of carbides calculated using ImageJ® software: (7.6 ± 2.8) %.**

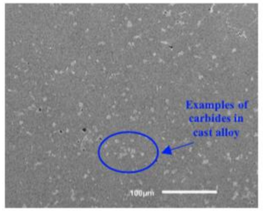

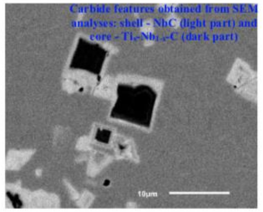

Figure 1. Characterization microstructural using different techniques (SEM – Scanning Electron Microscopy – and OM – Optical Microscopy) of the materials evaluated in the present work.

(a-) Homogeneous soft material and Heterogeneous soft material with soft particles: 3,302,700 linear hexahedral elements of type C3D8; and 3,376,209 nodes.

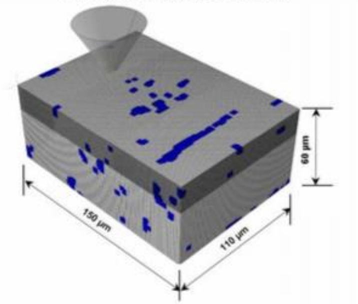

(b-) Heterogeneous soft material with hard particles: 3,143,252 linear hexahedral elements of type C3D8; and 3,238,485 nodes.

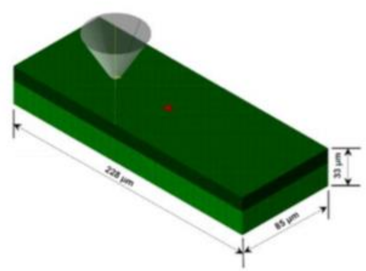

(c-) Hard materials (homogeneous and heterogeneous): 2,171,400 linear hexahedral elements of type C3D8; and 2,223,960 nodes.

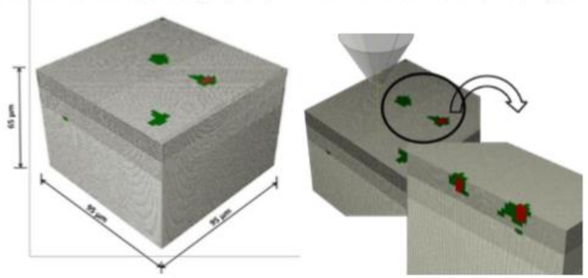

Figure 2. Finite element meshes generated from the microstructures of the materials studied: (a-) details of the heterogeneous soft material with soft precipitates (Group 2), composed by austenitic matrix and manganese sulfides; and (b-) heterogeneous soft material with hard precipitate (Group 3): austenitic matrix and titanium nitride; (c-) details of the heterogeneous hard material (Group 5), composed by martensitic matrix and niobium carbides, which are divided into a shell (in green – rich in Nb) and a core (in red – rich in Ti) [16].

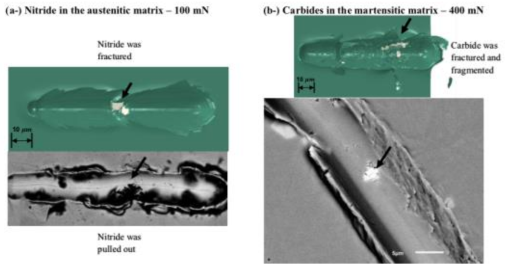

Figure 8. The reduction of the material removal resistance since the hard second phase particles tend to fracture, shear and/or fragment under higher normal loads applied during the micro-scratch tests.

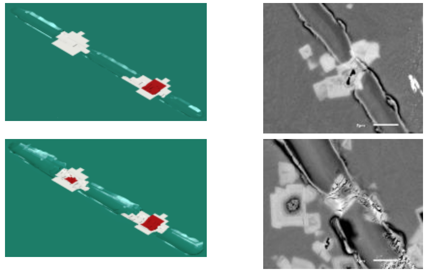

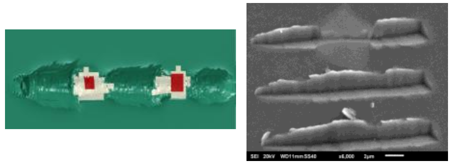

Riscamento

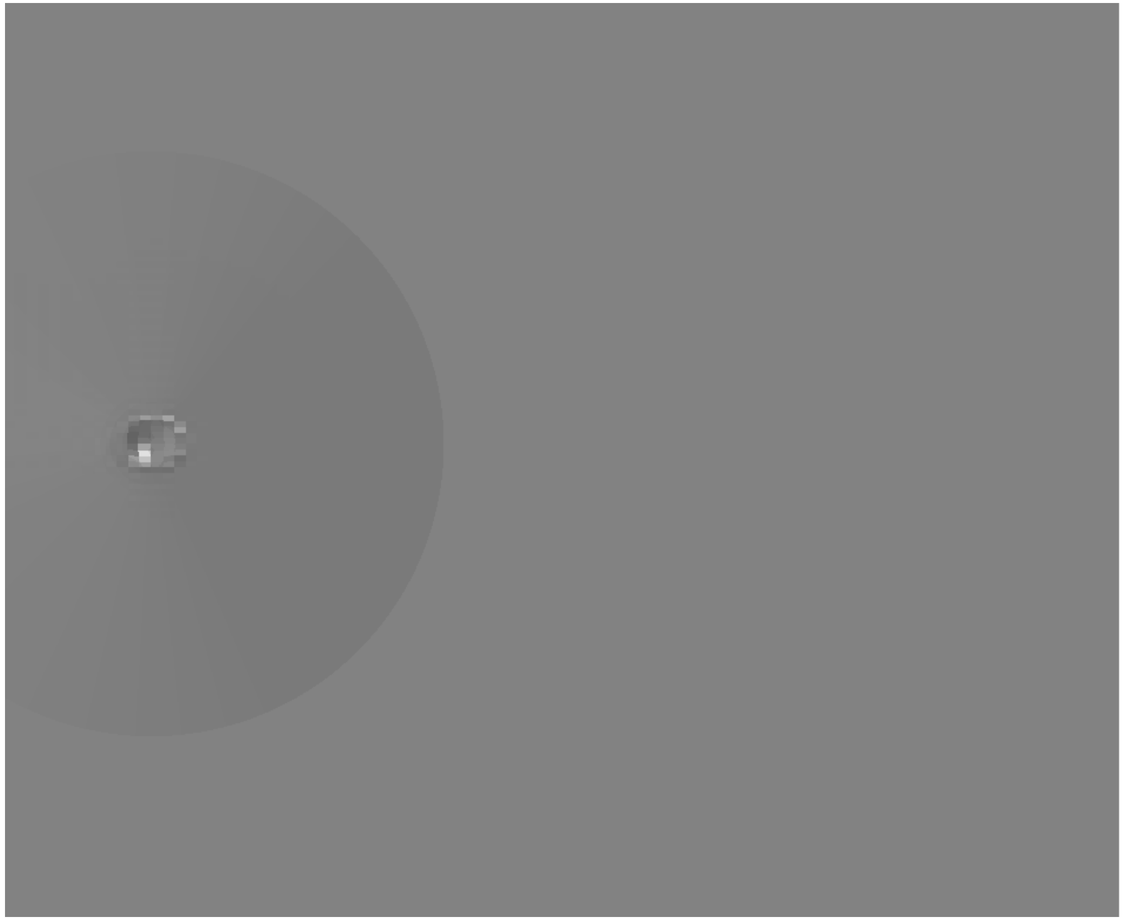

7

Study of angular cutting conditions using multiple scratch tests onto low carbon steel: An experimental-numerical approach

V. Seriacopi, S. Mezghani, S. Crequy, I.F. Machado, M. El Mansori, R.M. Souza, Wear

https://doi.org/10.1016/j.wear.2019.01.101

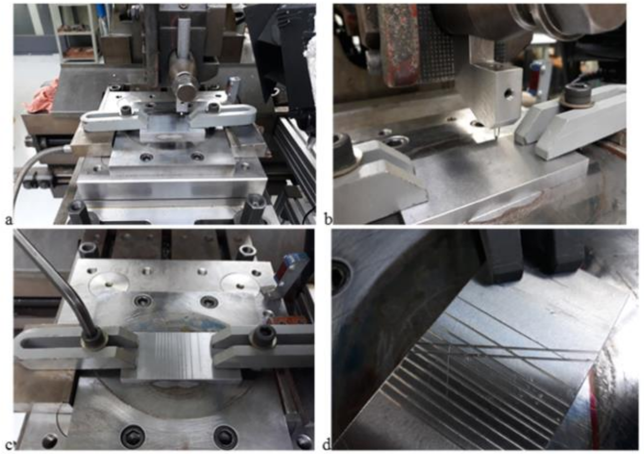

Fig. 1. Experimental setup of the scratch tests onto the 1020 steel conducted in the sequence a-d. Parallel scratches were carried out (a-c) and later a second set of parallel scratches was run at a specific angle (10, 20 or 30°) with respect to the previous one (d).

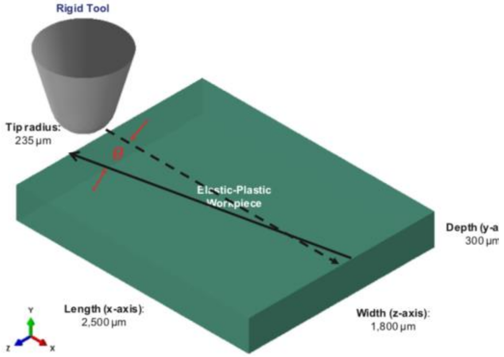

Fig. 2. Numerical modelling created to study the angled scratches. The following successive steps can be predicted here: (i-) first scratch due to the tool movement along x-direction; (ii-) tool moving along z-direction; and finally (iii-) angular scratches in the x-z plane (θ = 10, 20 and 30°), resulting in a V-shape or a X-shape depending on the angle and the consequent final scratch length.

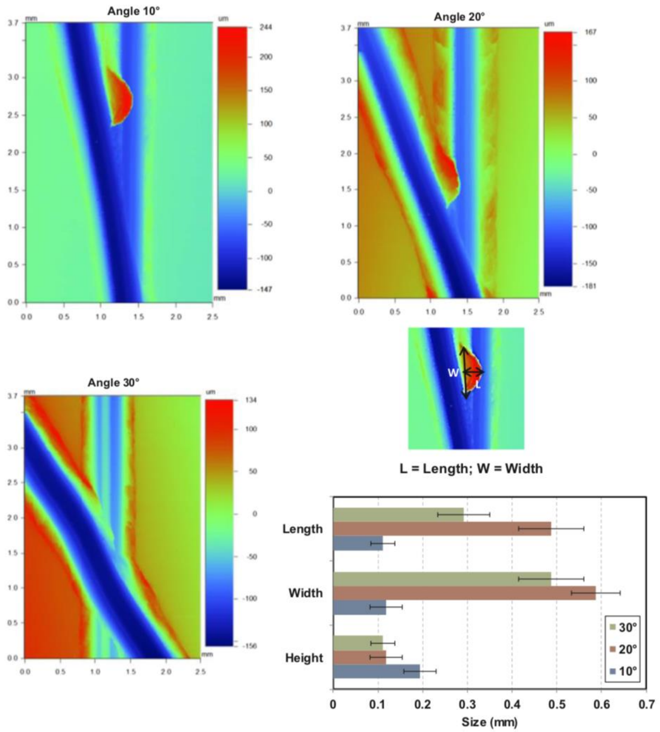

Fig. 5. Experimental results: topography characterization for all orientations. The burr features – length, width and height - are also displayed h

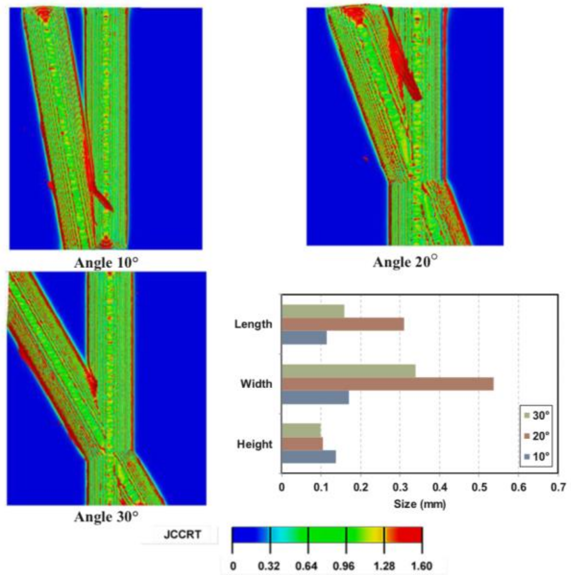

Fig. 6. Numerical results: Equivalent plastic strain at the onset of the fracture, defined by the Johnson-Cook damage criterion (JCCRT) for all orientations. The burr features – length, width and height – obtained from the numerical analyses are available here.

Study of angular cutting conditions using multiple scratch tests onto low T carbon steel: An experimental-numerical approach

V. Seriacopi, S. Mezghani, S. Crequy, I.F. Machado, M. El Mansori, R.M. Souza, Wear

https://doi.org/10.1016/j.wear.2019.01.101

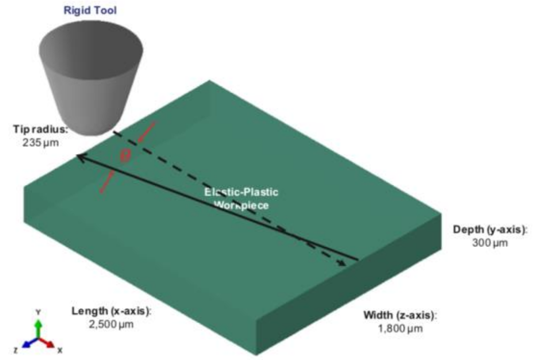

Fig. 2. Numerical modelling created to study the angled scratches. The following successive steps can be predicted here: (i-) first scratch due to the tool movement along x-direction; (ii-) tool moving along z-direction; and finally (iii-) angular scratches in the x-z plane (θ = 10, 20 and 30°), resulting in a V-shape or a X-shape depending on the angle and the consequent final scratch length.

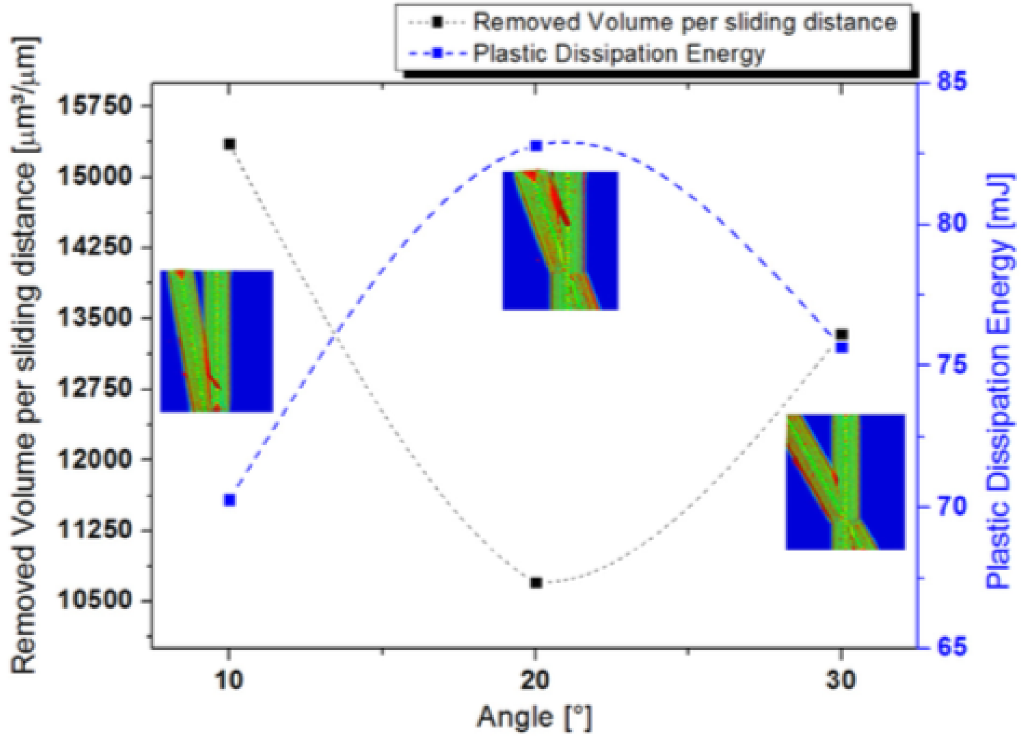

Fig. 7. Numerical results of the material removal and plastic dissipation energy as a function of the orientation of the angular scratch.

8

Numerical analyses of stress induced damage during a reciprocating lubricated test of FeCMo SPS sintered alloy

N.K.Fukumasu, G.Boidi, V.Seriacopi, G.A.A.Machado, R.M.Souza, I.F.Machado, Tribology International

https://doi.org/10.1016/j.triboint.2016.12.025

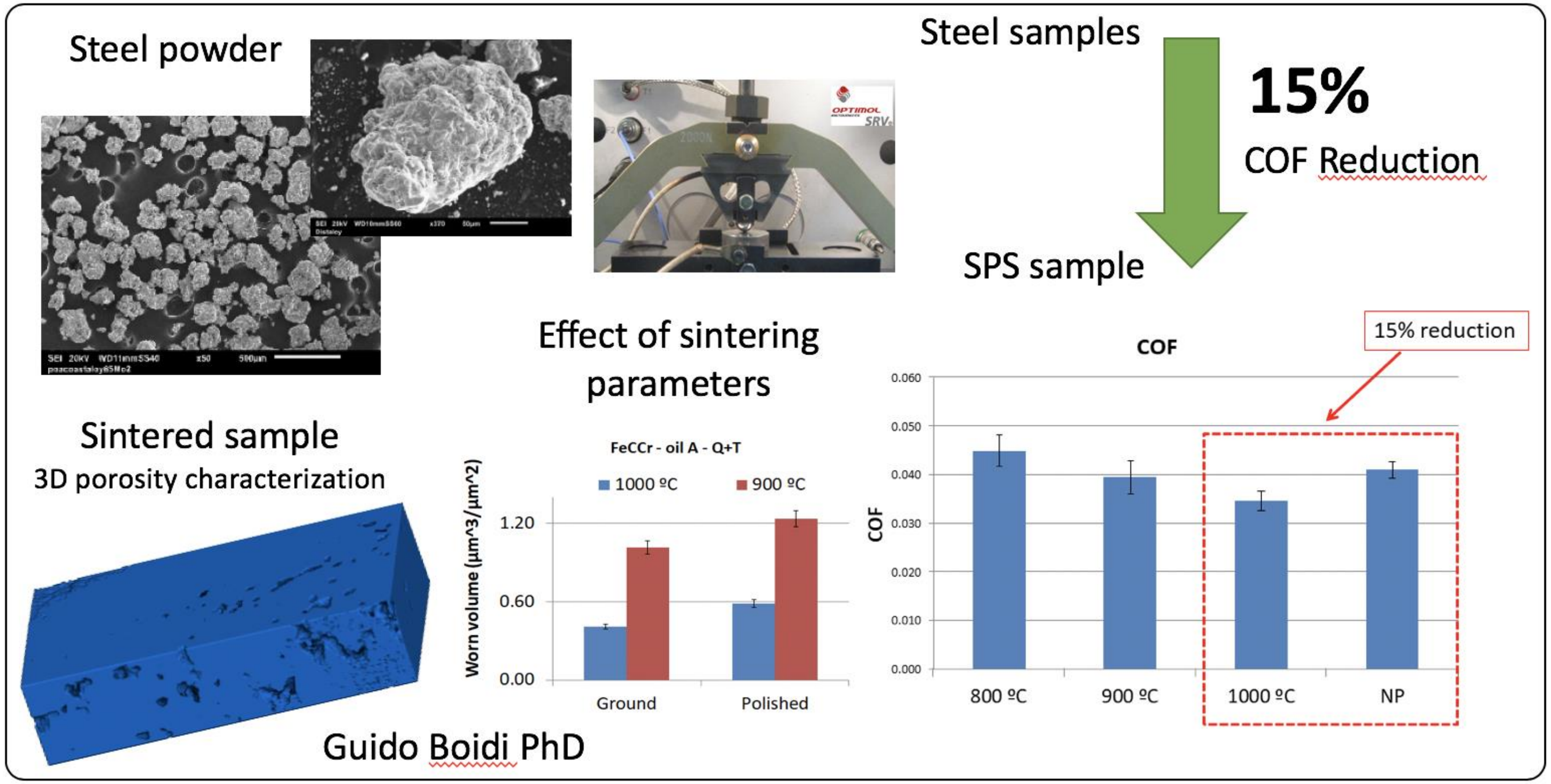

Numerical analyses of stress induced damage during a reciprocating lubricated test of FeCMo SPS sintered alloy

N.K.Fukumasu, G.Boidi, V.Seriacopi, G.A.A.Machado, R.M.Souza, I.F.Machado, Tribology International

https://doi.org/10.1016/j.triboint.2016.12.025

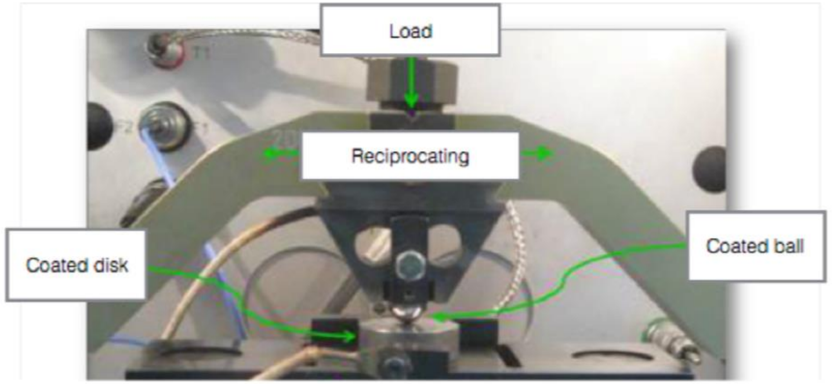

Fig. 1. Macroscale reciprocating test configuration analyzed in this work, in which both sphere and disk were coated.

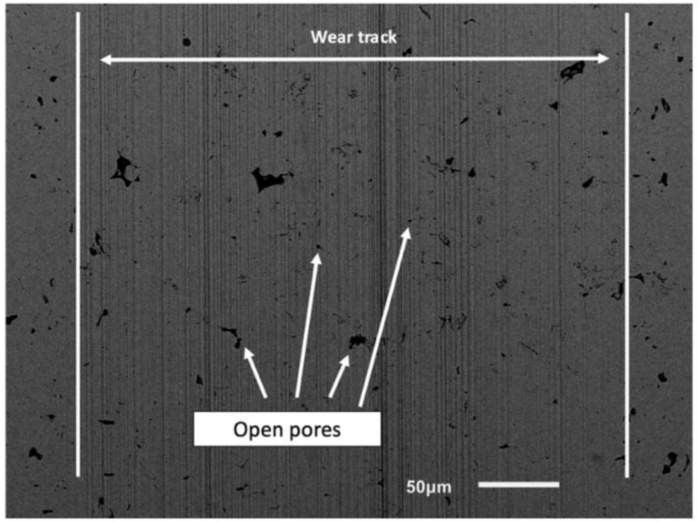

Fig. 5. Back scattered SEM image of the wear track from the experimental reciprocating test with contact pressure of 2.5 GPa.

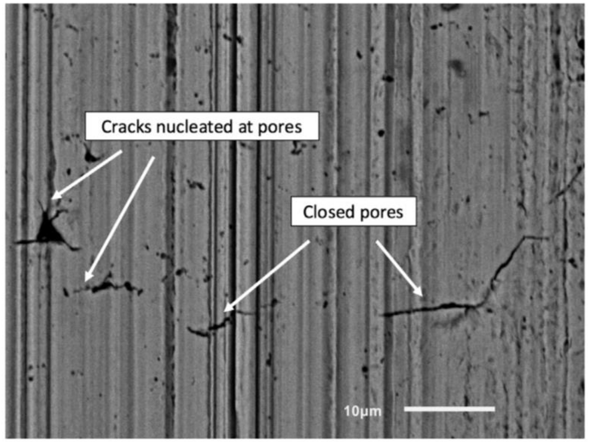

Fig. 8. Higher magnification of the back scattered SEM image of the white ellipses in Fig. 7.

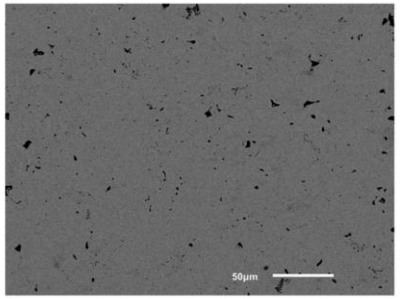

Fig. 3. Back scattered SEM image of the sintered FeCMo material presenting less than 2% porosity.

Numerical analyses of stress induced damage during a reciprocating lubricated test of FeCMo SPS sintered alloy

N.K.Fukumasu, G.Boidi, V.Seriacopi, G.A.A.Machado, R.M.Souza, I.F.Machado, Tribology International

https://doi.org/10.1016/j.triboint.2016.12.025

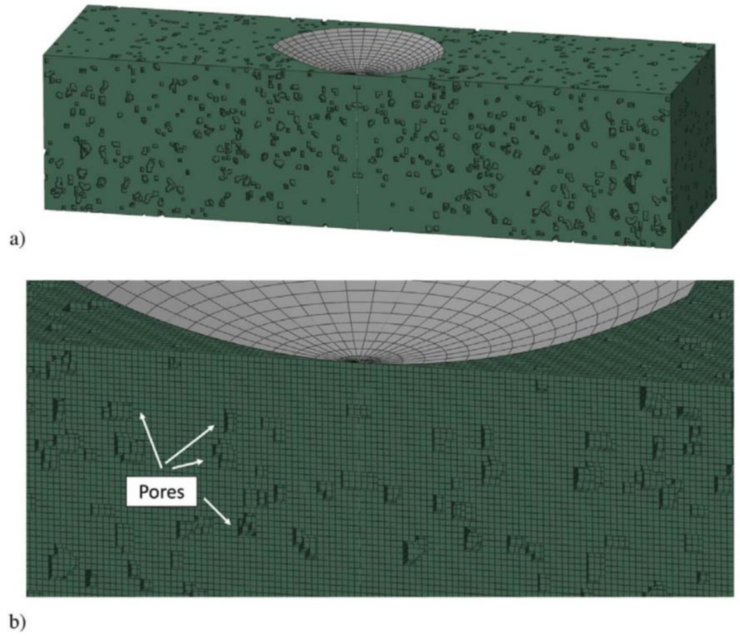

Fig. 1. Computational domain for the reciprocating test analyses: a) system composed by an analytical rigid sphere (gray) and a plane counterbody (dark green); b) detail of the system indicating the porosity represented as small voids (regions without elements) in the numerical mesh. (For interpretation of the references to color in this figure legend, the reader is referred to the web version of this article.)

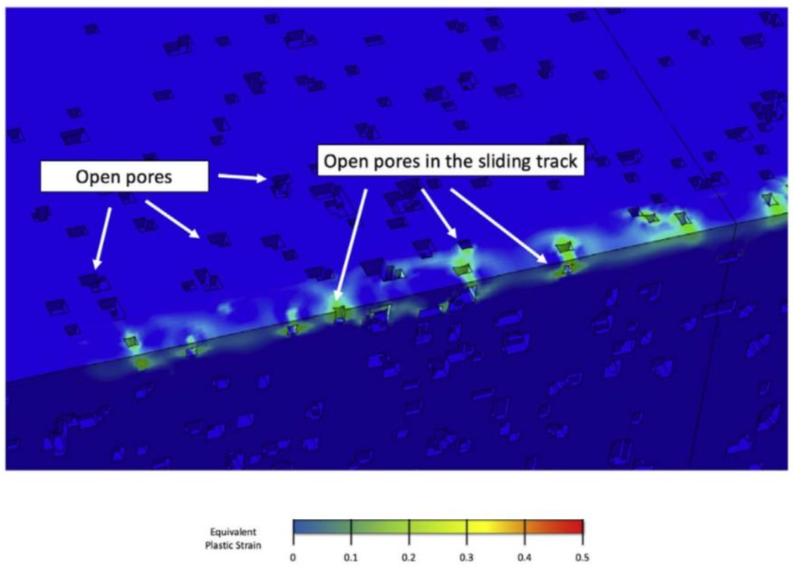

Fig. 4. Localized plastic deformation induced by the pores during the sliding of the sphere. The color field indicate the level of plastic deformation.

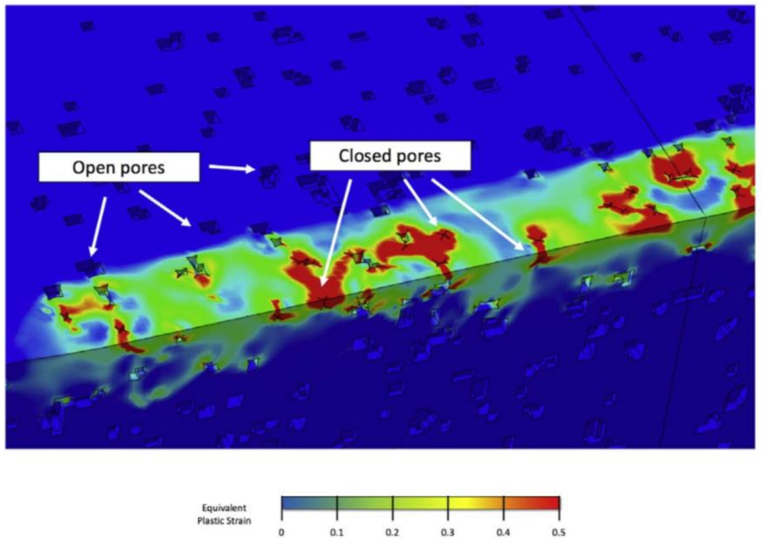

Fig. 6. Collapse of the pores by the plastic deformation during the sliding of the sphere. The color field indicate the level of plastic deformation and red regions indicate plastic deformation higher than 50%.

Numerical analyses of stress induced damage during a reciprocating lubricated test of FeCMo SPS sintered alloy

N.K.Fukumasu, G.Boidi, V.Seriacopi, G.A.A.Machado, R.M.Souza, I.F.Machado, Tribology International

https://doi.org/10.1016/j.triboint.2016.12.025

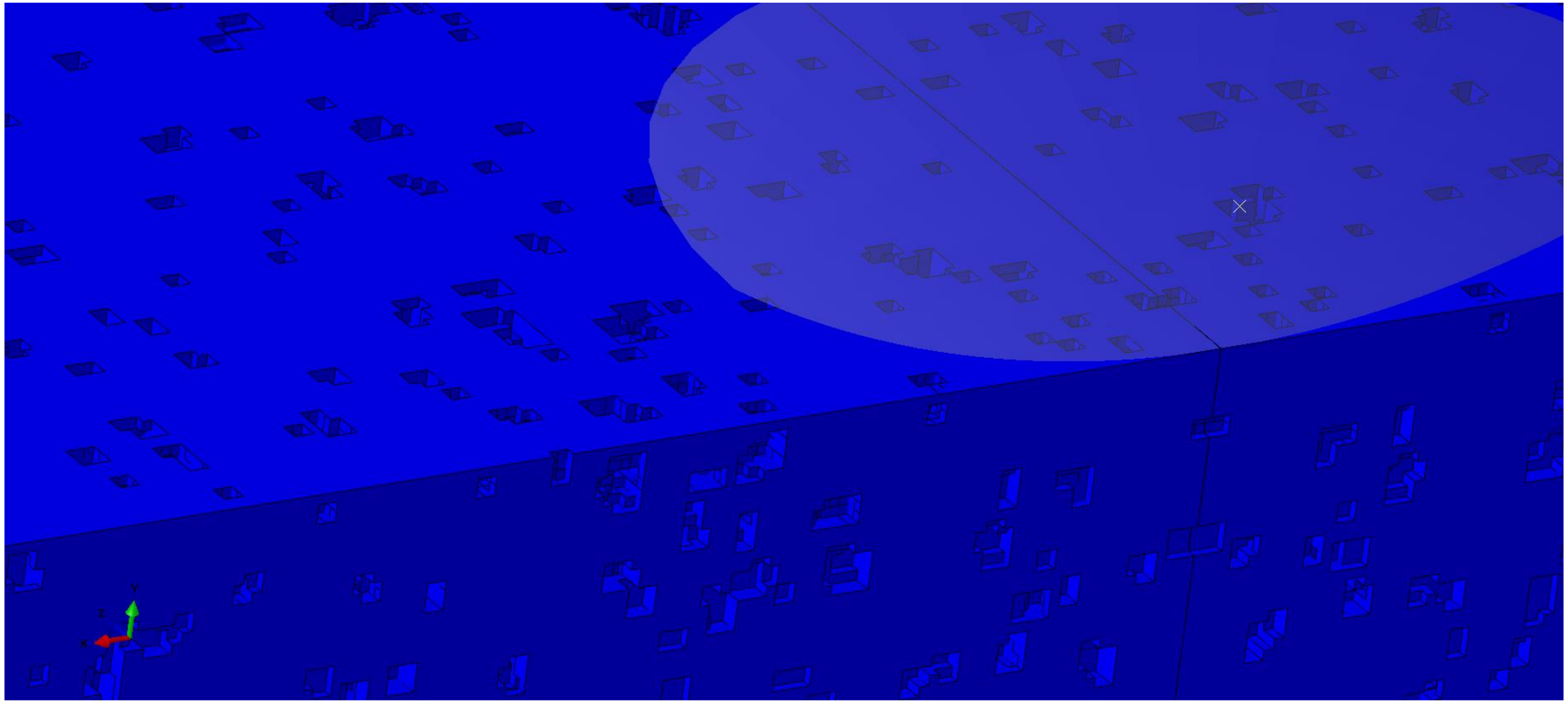

Numerical analyses of stress induced damage during a reciprocating lubricated test of FeCMo SPS sintered alloy

N.K.Fukumasu, G.Boidi, V.Seriacopi, G.A.A.Machado, R.M.Souza, I.F.Machado, Tribology International

https://doi.org/10.1016/j.triboint.2016.12.025

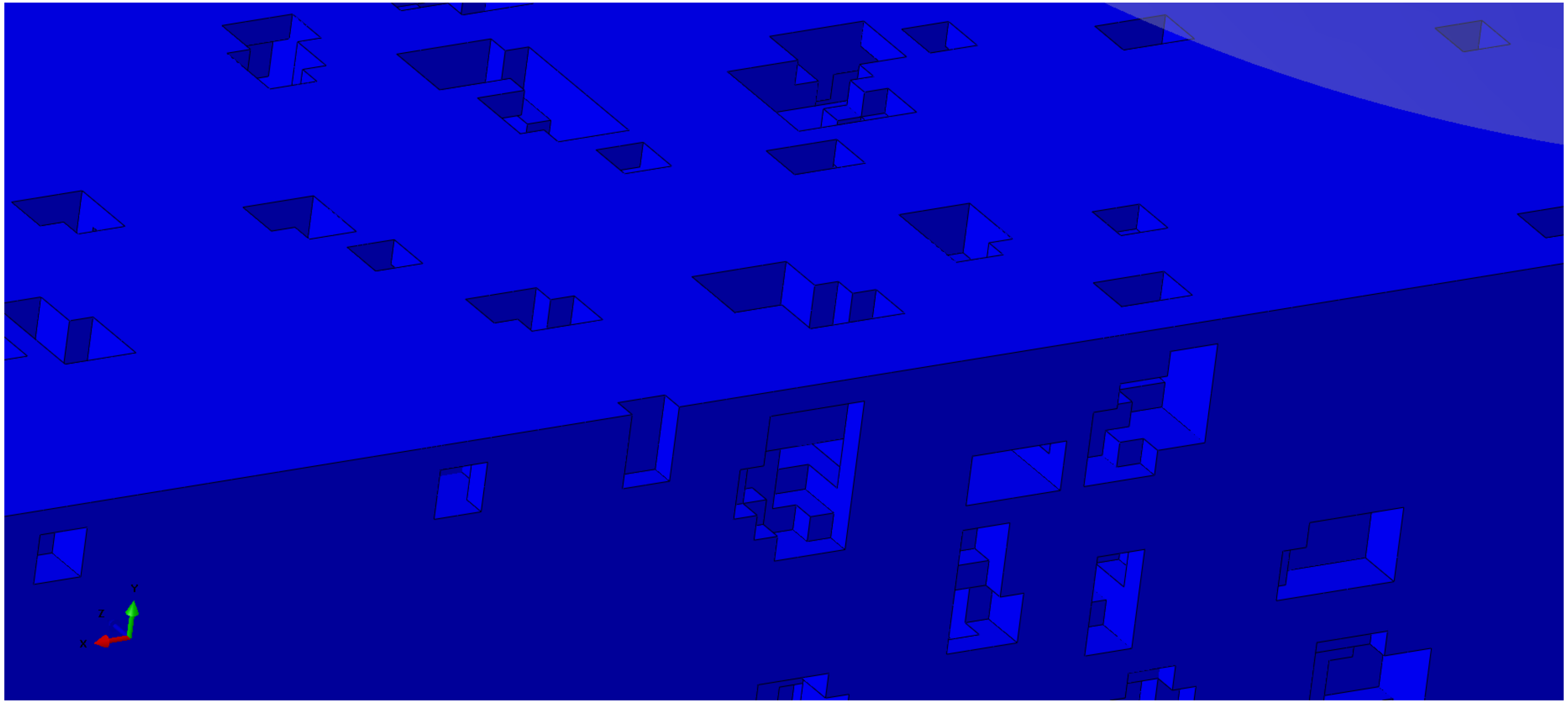

Influence of Sintering Parameters on Micro-Scale Mechanical and Tribological Behavior of Niobium Carbides

N.K. Fukumasu, A.J.O.Tertuliano, C.F. Bernardes, V. Seriacopi, R.M. Souza, I.F. Machado

Plansee Seminar - 2017

Wear

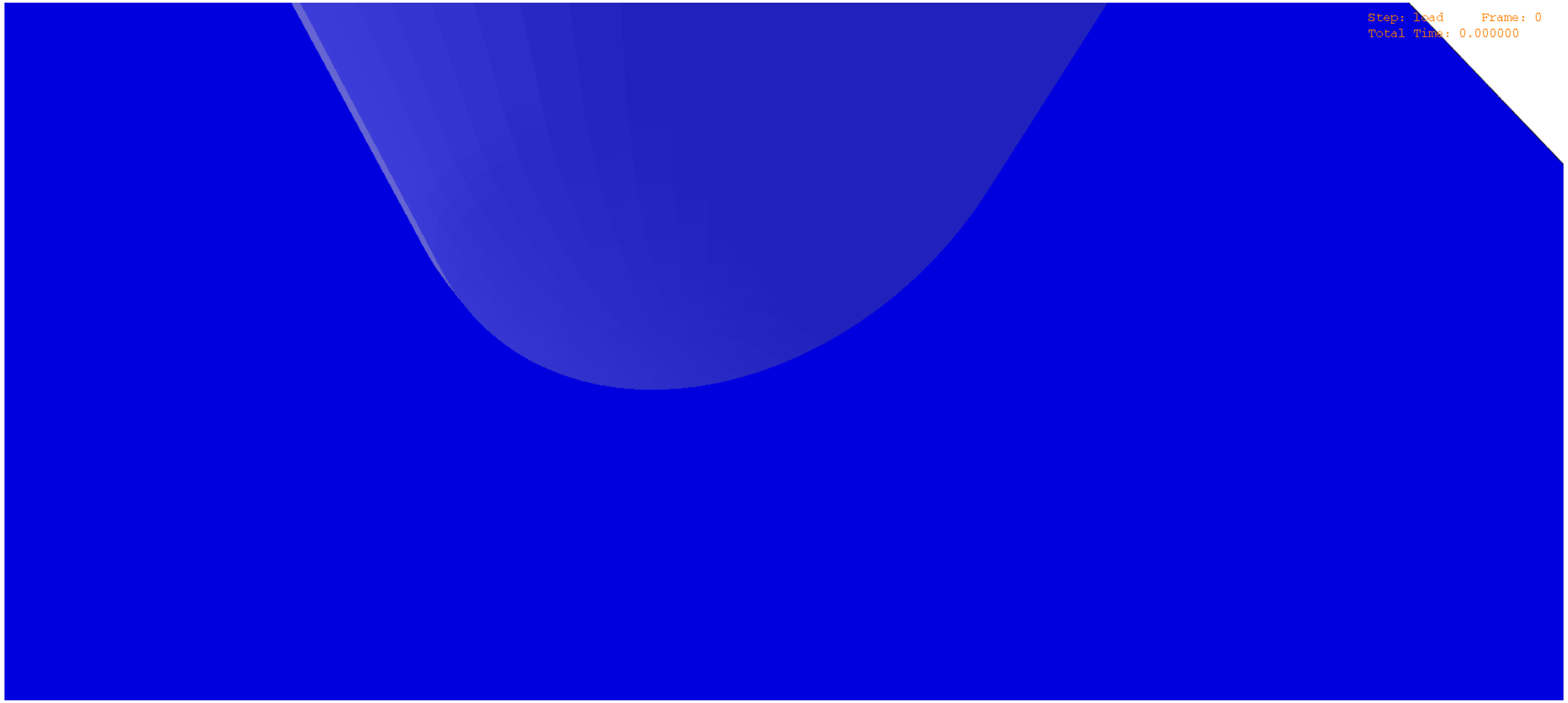

10

Local transformation of amorphous hydrogenated carbon coating induced by high contact pressure

N.K. Fukumasu, C.F. Bernardes, M.A. Ramirez, V.J. Trava-Airoldi, R.M. Souza, I.F. Machado

Tribology International

https://doi.org/10.1016/j.triboint.2018.04.006

The coating and the interlayer were deposited using a pulsed Direct Current Plasma Enhanced Chemical Vapor Deposition (DC PECVD)

Under dry sliding condition, DLC coated systems may present a reduction of friction force based on the graphitization of the contacting surfaces, as observed by Liu et al. [9]. This phenomenon is related to the re- arrangement of the sp3 and sp2 carbon bonds by energy transferred from the mechanical movement to chemical bond kinetics.

Scratch test on coated systems – sequence of stress states

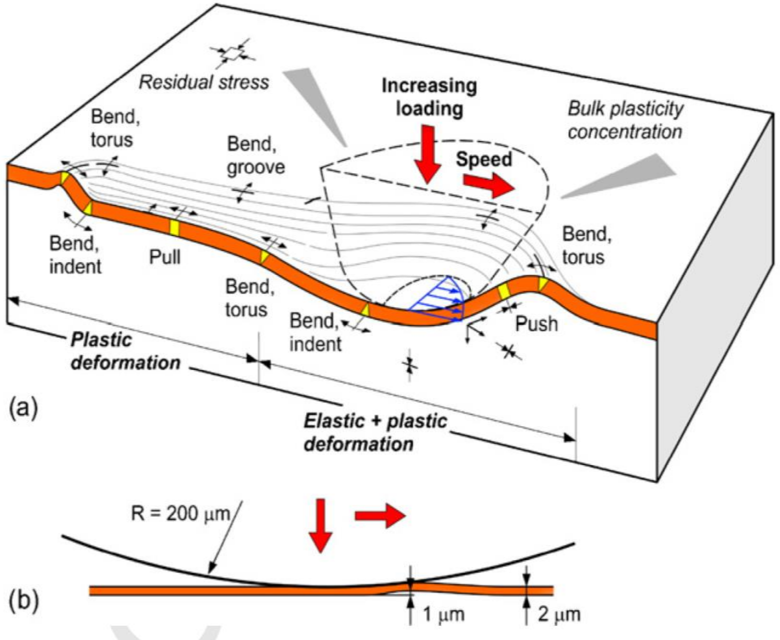

[Holmberg *et al.* Wear 267 (2009) 2142–2156]

Local transformation of amorphous hydrogenated carbon coating induced by high contact pressure

N.K. Fukumasu, C.F. Bernardes, M.A. Ramirez, V.J. Trava-Airoldi, R.M. Souza, I.F. Machado

Tribology International

https://doi.org/10.1016/j.triboint.2018.04.006

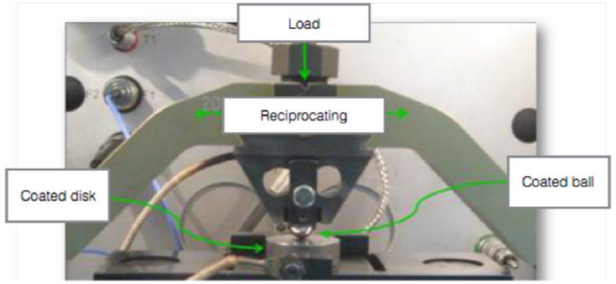

Fig. 1. Macroscale reciprocating test configuration analyzed in this work, in which both sphere and disk were coated.

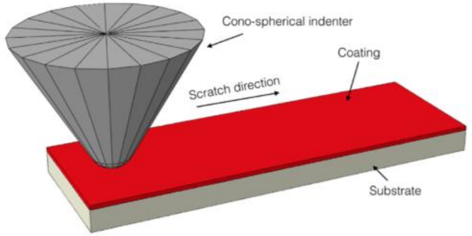

Fig. 2. Numerical model configuration consisting of a cono-spherical tip used to scratch the coated (red) substrate (light gray). (For interpretation of the references to color in this figure legend, the reader is referred to the Web version of this article.)

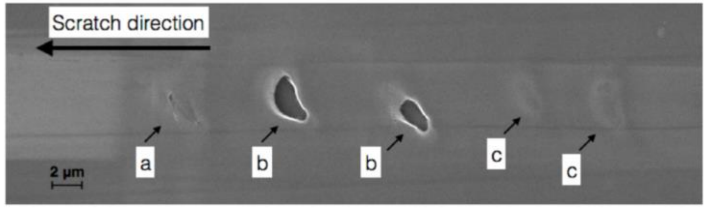

Fig. 8. Microscale scratch track presenting the local typical observed failure modes: a) adhesive and cohesive failures of the coating; b) complete spallation of coating and c) adhesive failure of the coating/substrate interface.

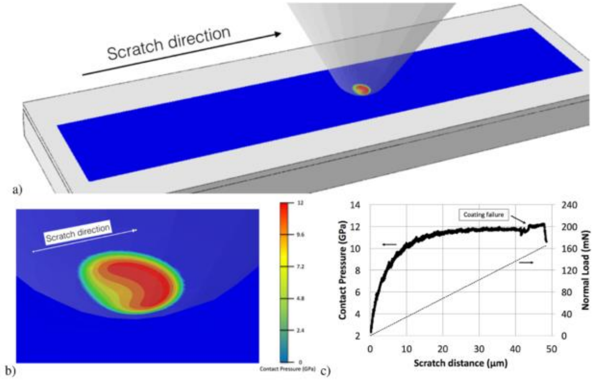

Fig. 14. Contact Pressure at the coating promoted by the indenter movement: a) Instantaneous spatial distribution of the contact pressure; b) detail of the contact region and c) evolution of the contact pressure with the ramping load during the scratch test.

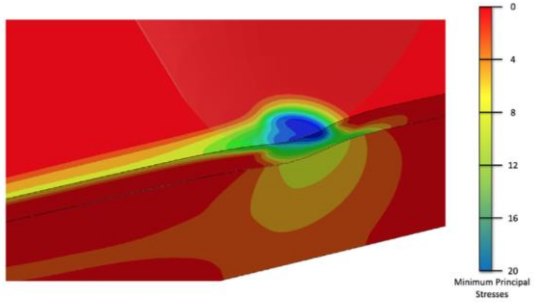

Fig. 15. Minimum Principal Stresses distribution developed inside of the material during the scratch test.

Local transformation of amorphous hydrogenated carbon coating induced by high contact pressure

N.K. Fukumasu, C.F. Bernardes, M.A. Ramirez, V.J. Trava-Airoldi, R.M. Souza, I.F. Machado , Tribology International

https://doi.org/10.1016/j.triboint.2018.04.006

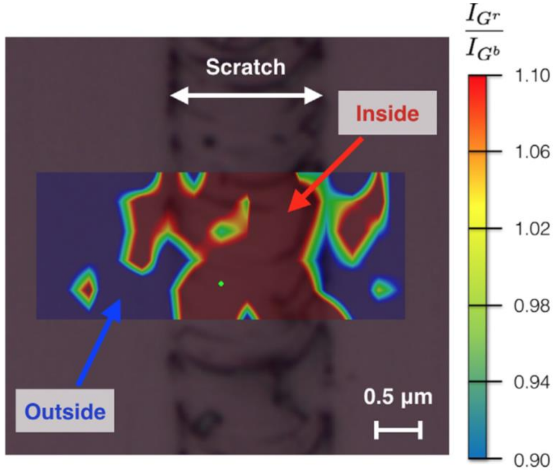

Fig. 9. Superimposed Raman spectroscopy map of I_{G^r}/I_{G^b} ratio on the scratch track of Fig. 8. Higher ratio values (red colored regions) indicate a red-shift of the G band. (For interpretation of the references to color in this figure legend, the reader is referred to the Web version of this article.)

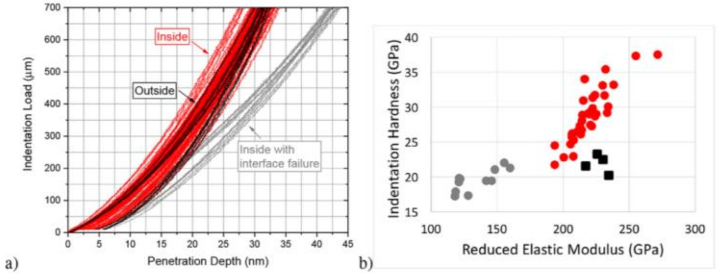

Fig. 6. Nano-indentation measurements of the coating: a) nano-indentation curves for inside (red and gray lines) and outside (black lines) of the wear track; b) results for hardness and reduced elastic modulus of the coating for inside (circles) and outside (squares) of the wear track. Red circles indicate similar reduced elastic modulus but higher hardness compared to outside measurements (black squares), while gray circles indicate a reduction on both characteristics. (For interpretation of the references to color in this figure legend, the reader is referred to the Web version of this article.)

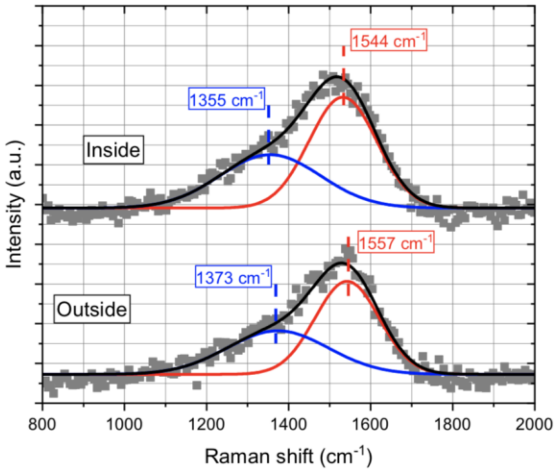

Fig. 10. Raman spectroscopy analysis of a-C:H coatings after the scratch test. Gray squares indicate typical spectra obtained for inside and outside the scratched regions, while lines indicate the deconvolution of the Raman spectra into D (blue) and G (red) bands. (For interpretation of the references to color in this figure legend, the reader is referred to the Web version of this article.)

Numerical simulation indicates high contact pressure (>12GPa) developed at the surface and high internal stresses, ranging from 20 GPa to 12 GPa, are developed along coating thickness. The increase on indentation hardness inside the scrat- ched region are compatible with the nucleation of sp3 carbon bond sites derived from sp2 bonds.

12

Influence of spark plasma consolidation conditions on the superconducting properties of (Bi,Pb)-Sr-Ca-Cu-O ceramic samples

F. Rosales-Saiz, L. Pérez-Acosta , I.F. Machado , J.E. Pérez-Fernández , R.F. Jardim , E. Govea-Alcaide, Ceramics International

http://dx.doi.org/10.1016/j.ceramint.2016.08.053

Influence of the material die and plungers on the superconducting properties of Bi1.65Pb0.35Sr2Ca2 Cu3O10 δ samples processed by the Spark Plasma Sintering method. Samples were then consolidated by using two setups comprised of different materials: **all-steel and all-graphite**. Finite element simulations (FEM) were performed to provide extra information regarding the distribution of temperature within the samples. X-ray diffraction (XRD) analysis and DC magnetization as a function of temperature, M(T), have been conducted in all synthesized samples as complementary char- acterizations. The main motivation of this study is to evaluate the influence of the material setup of the SPS apparatus on the de- oxygenation of Bi-2223 compounds consolidated by the SPS method.

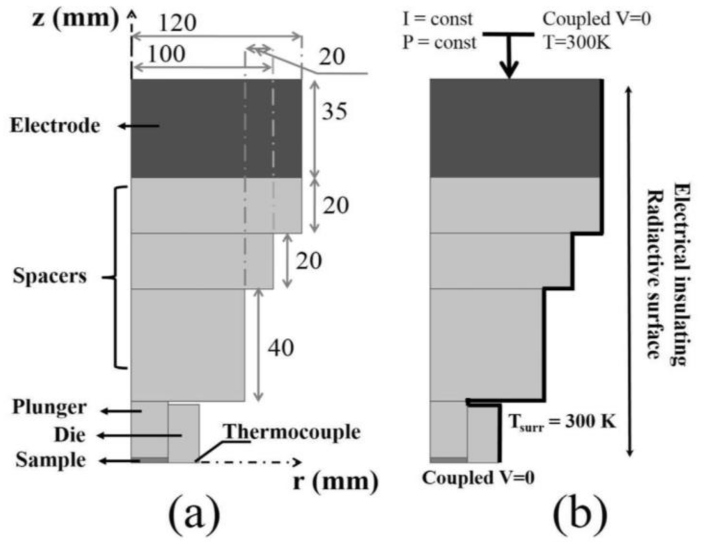

Fig. 1. (a) Schematic drawing of the consolidation system; (b) boundary conditions.

Table 1
Consolidation parameters used during the SPS process for producing Bi-2223 samples. T_D is the consolidation temperature, HR is the heating rate, t_r is the heating time, and t_D is the consolidation time. We also included values of the density of the pellets, D.

Sample	T_D (°C)	HR (°C/min)	t_r (min)	t_D (min)	D (g/cm³)
H1	700	135	5	5	4.8
H2	750	50	15	5	5.5
G1	750	145	5	5	5.7

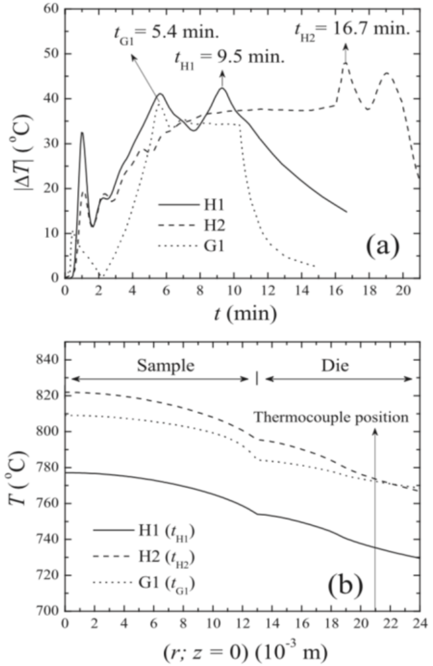

Fig. 3. (a) Estimated temperature difference during the SPS process for the studied samples; (b) the simulated radial temperature profiles for z=0 of samples H1, H2, and G1, respectively (see text for details).

Surface damage modeling

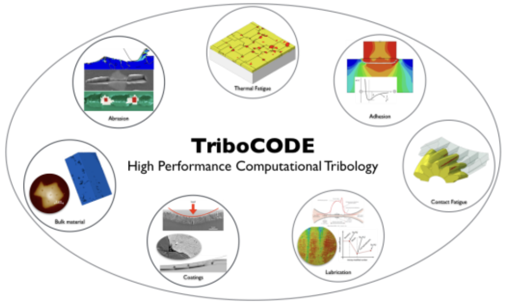

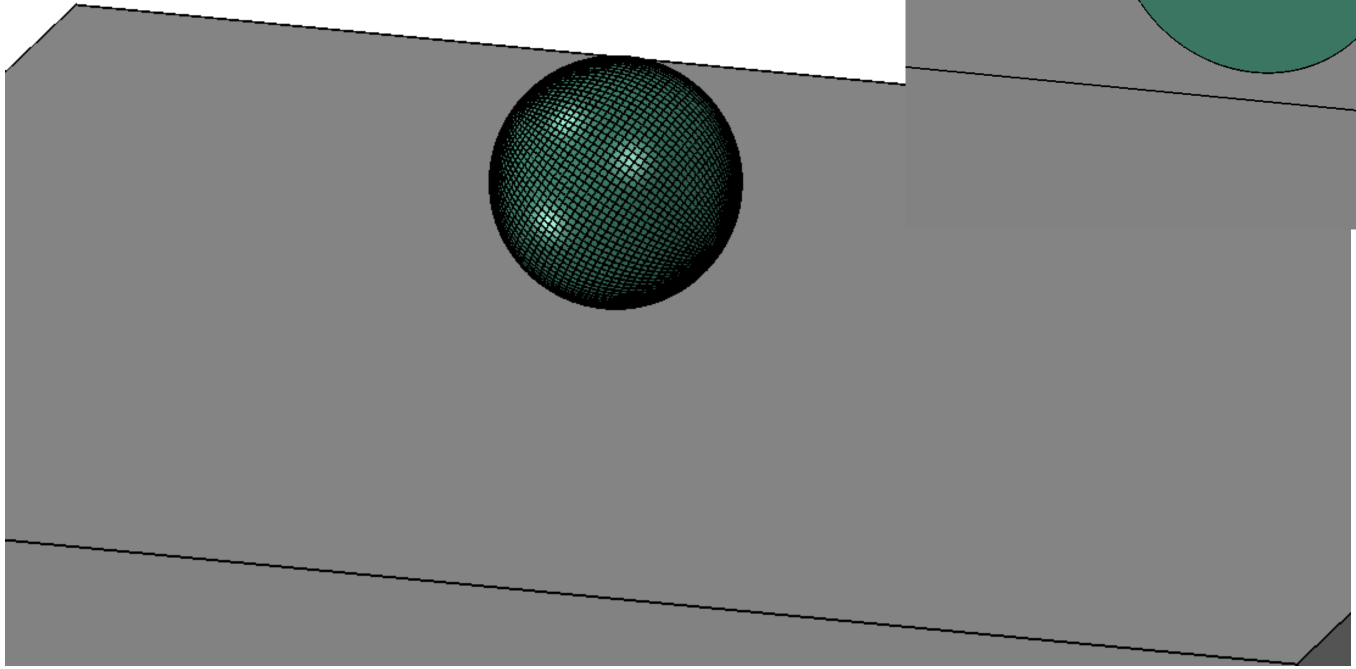

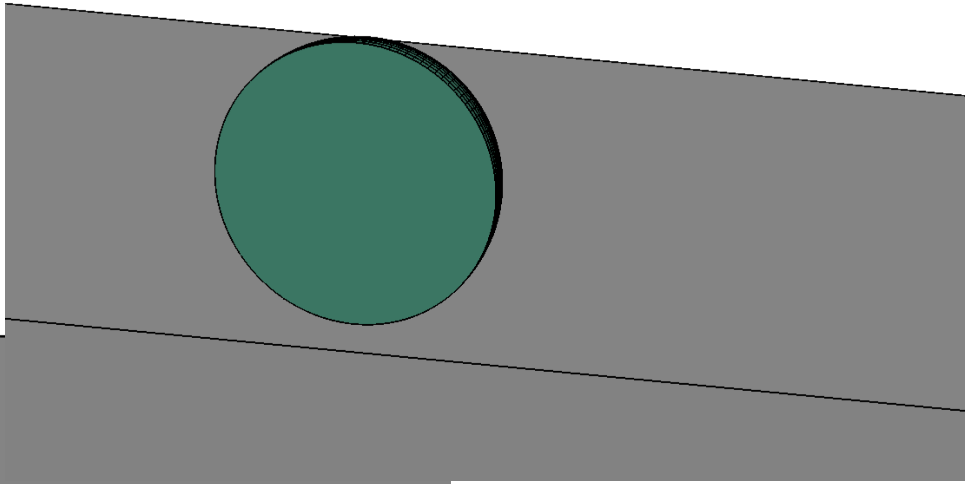

Surface damage modeling

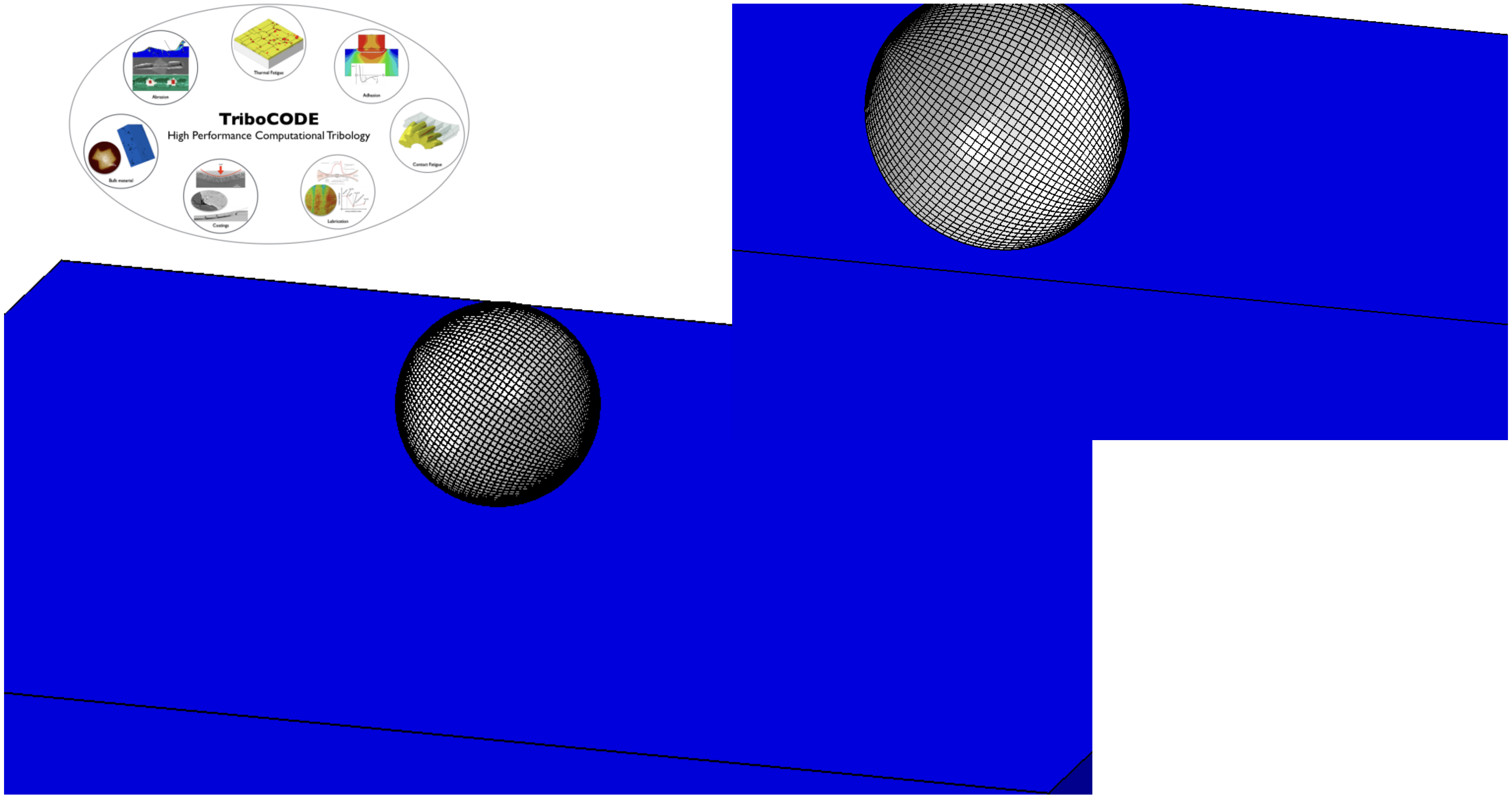

Surface damage modeling

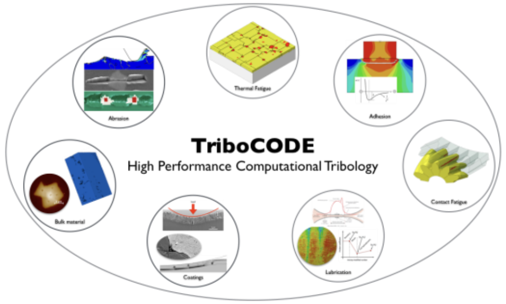

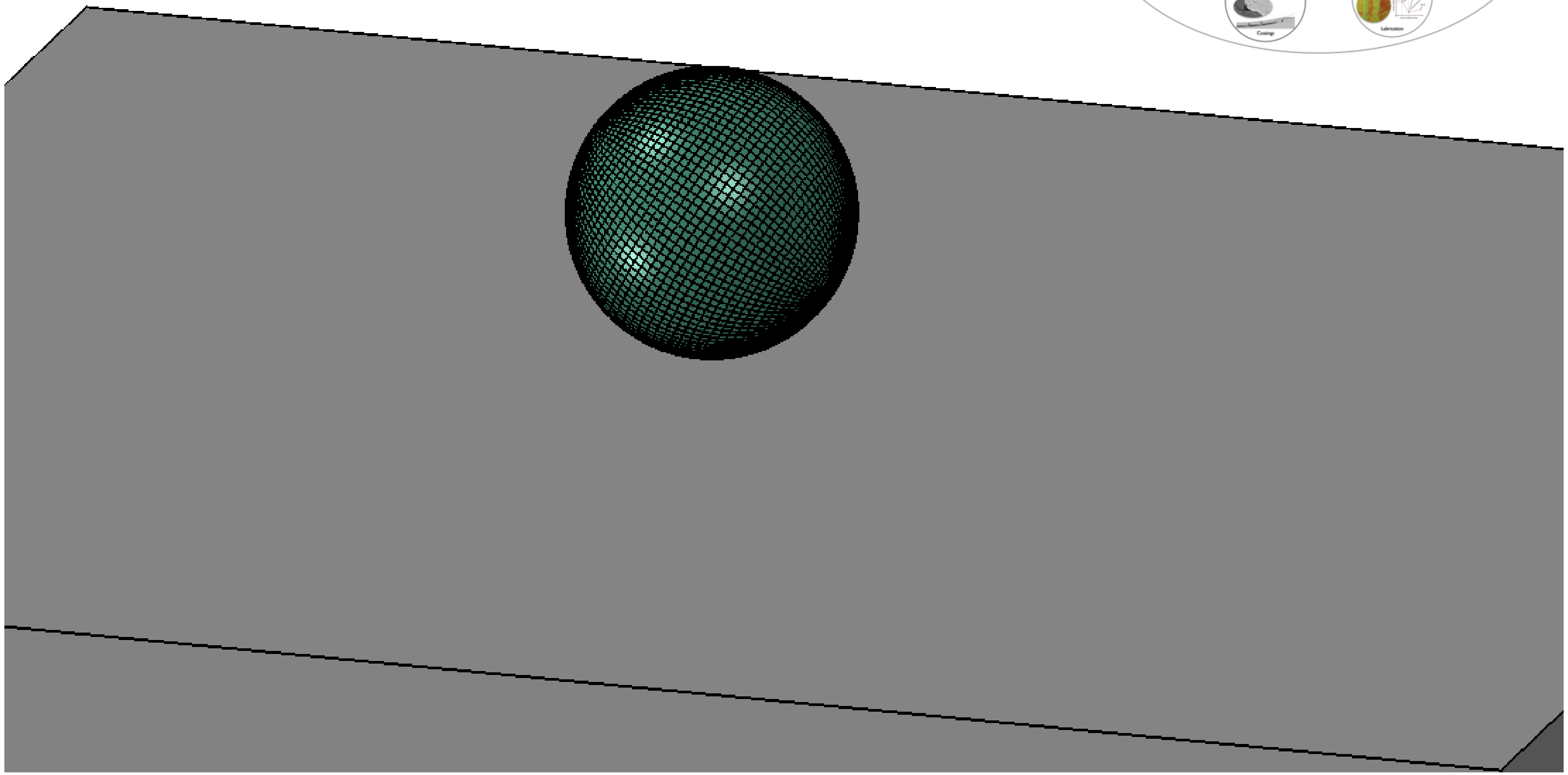

- https://www.youtube.com/watch?v=FdipJNG_vV8

CAM

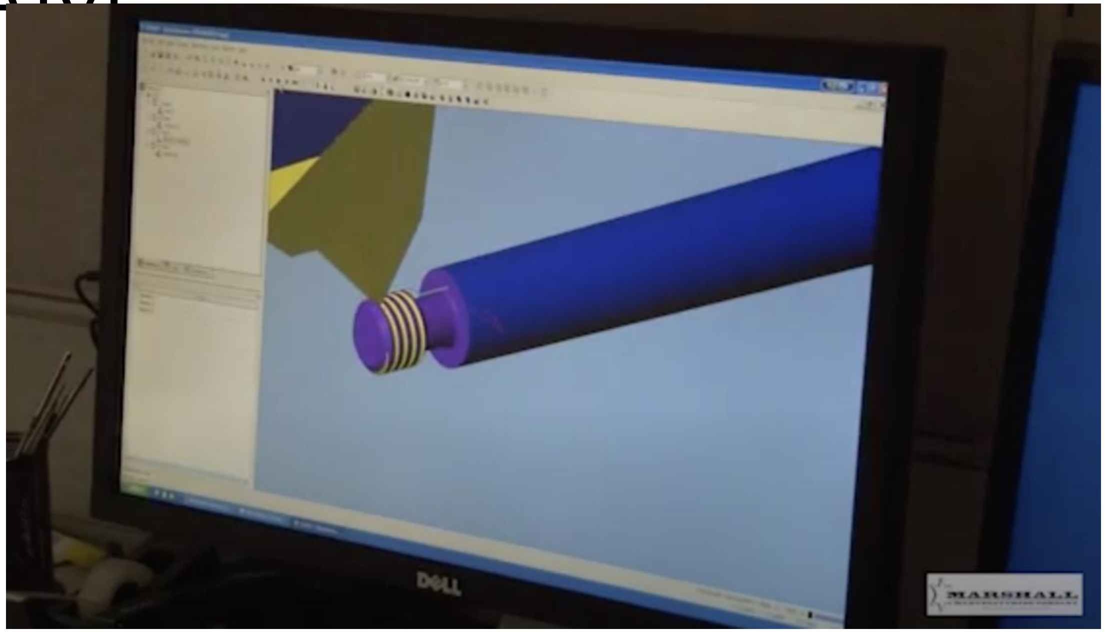

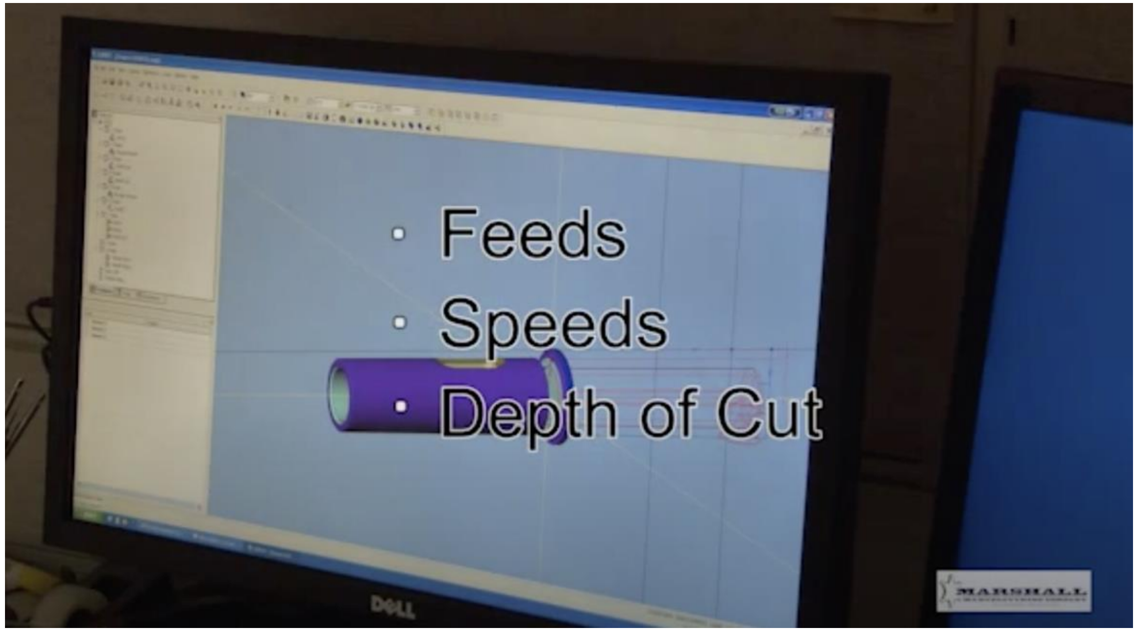

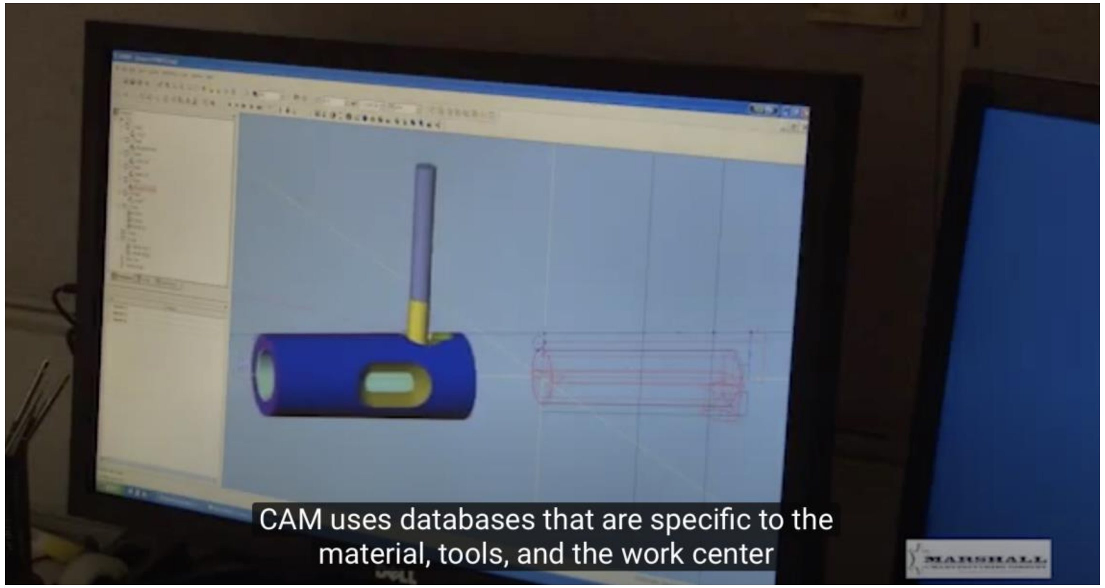

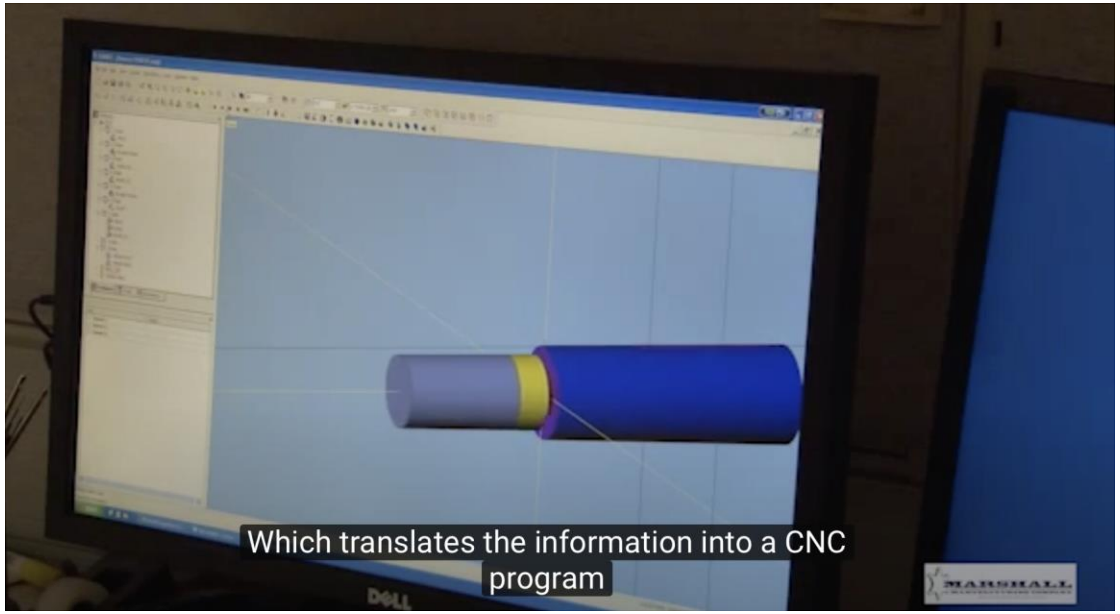

CAM

- https://www.youtube.com/watch?v=JrmYZIrcuMs

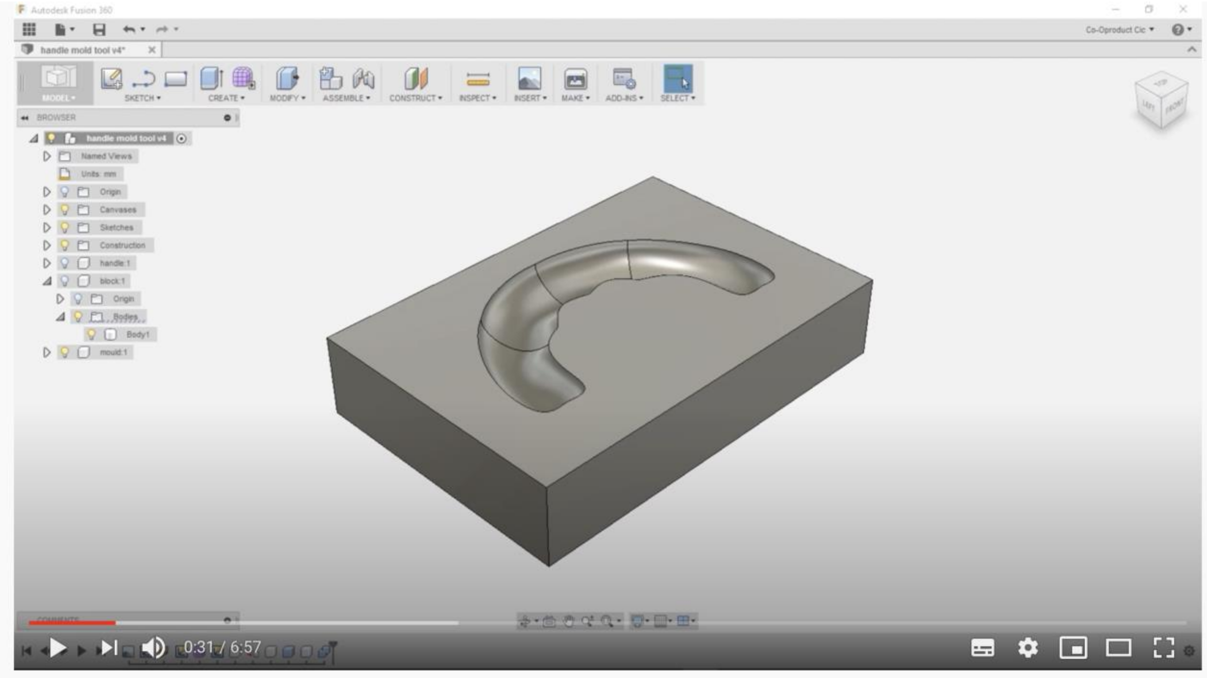

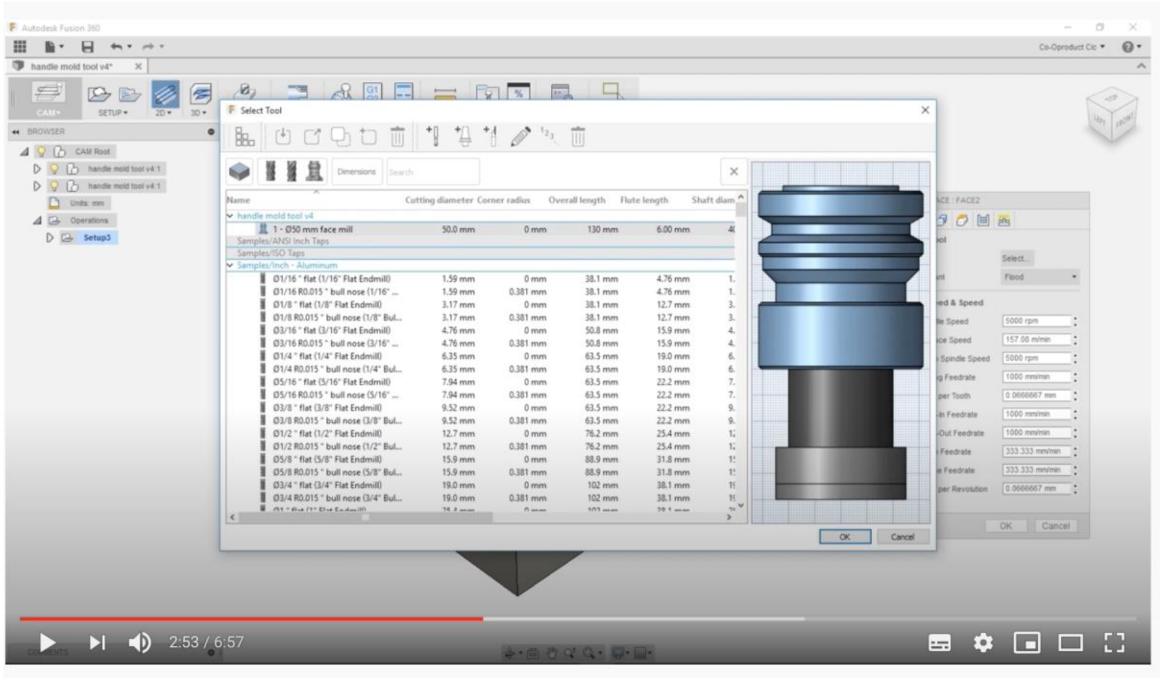

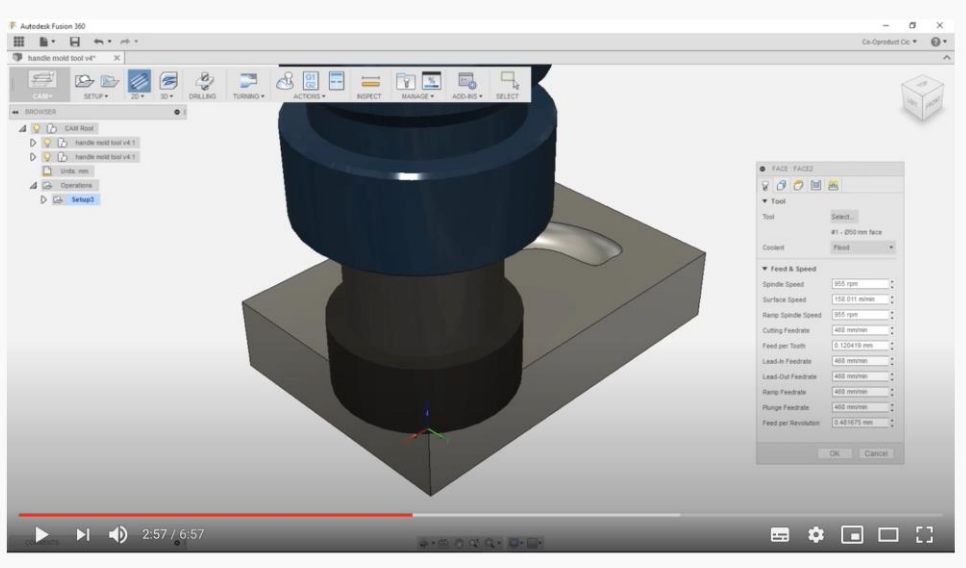

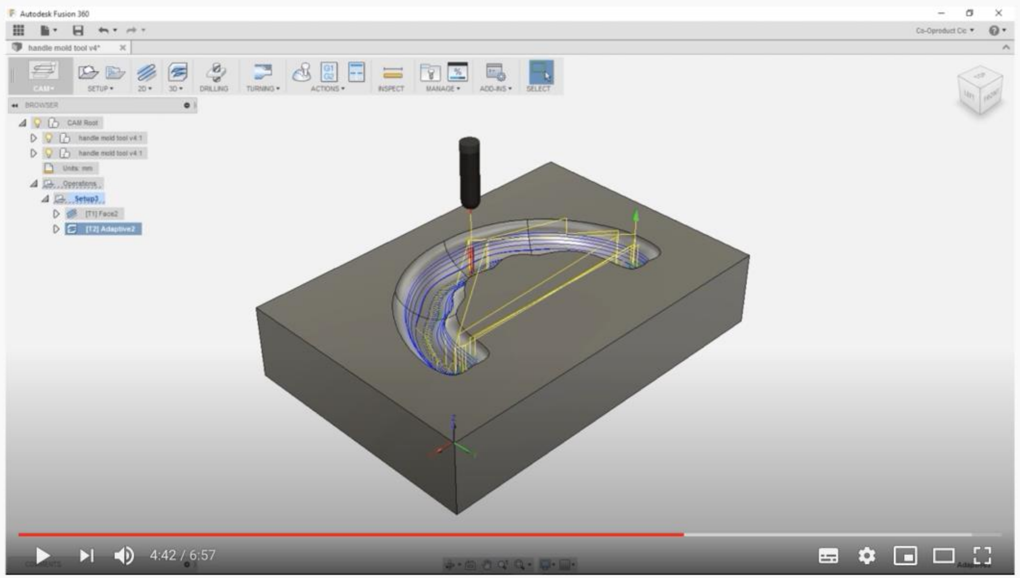

CAM

- https://www.youtube.com/watch?v=JrmYZIrcuMs

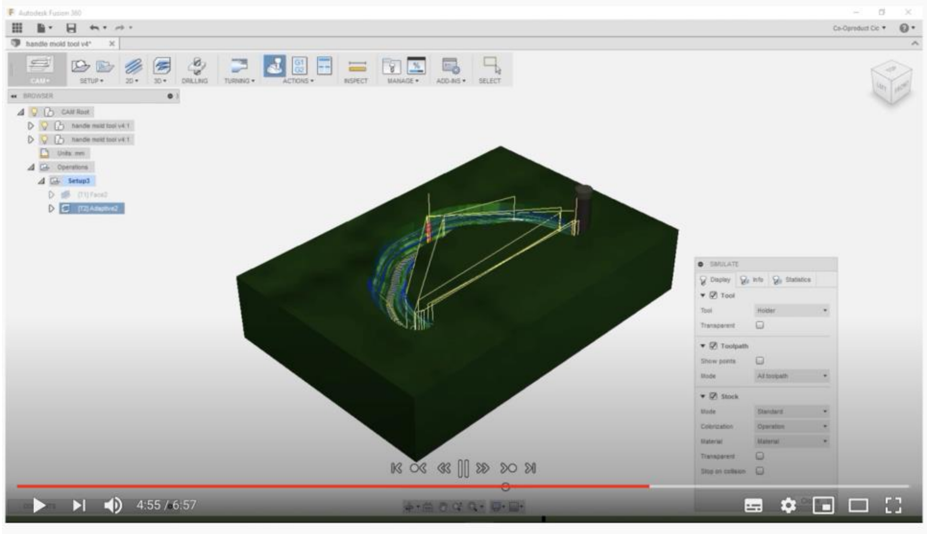

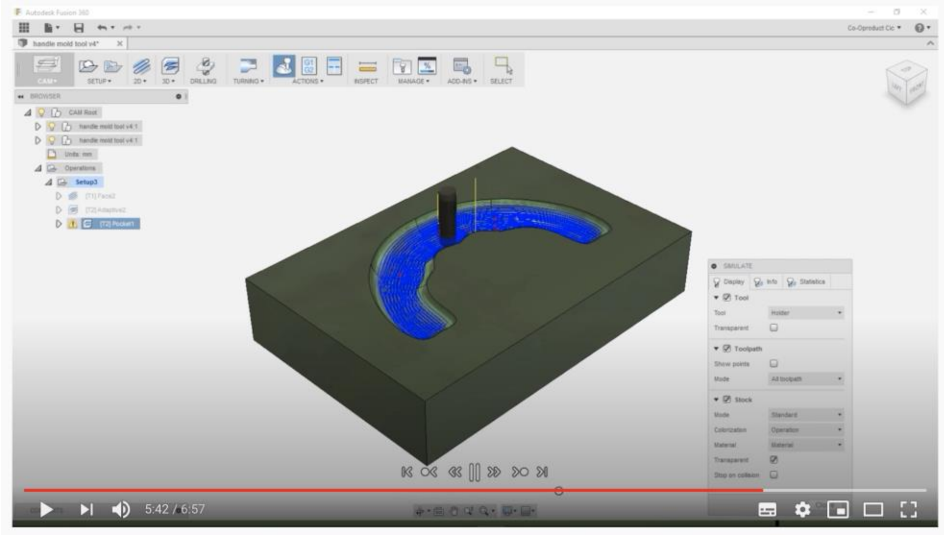

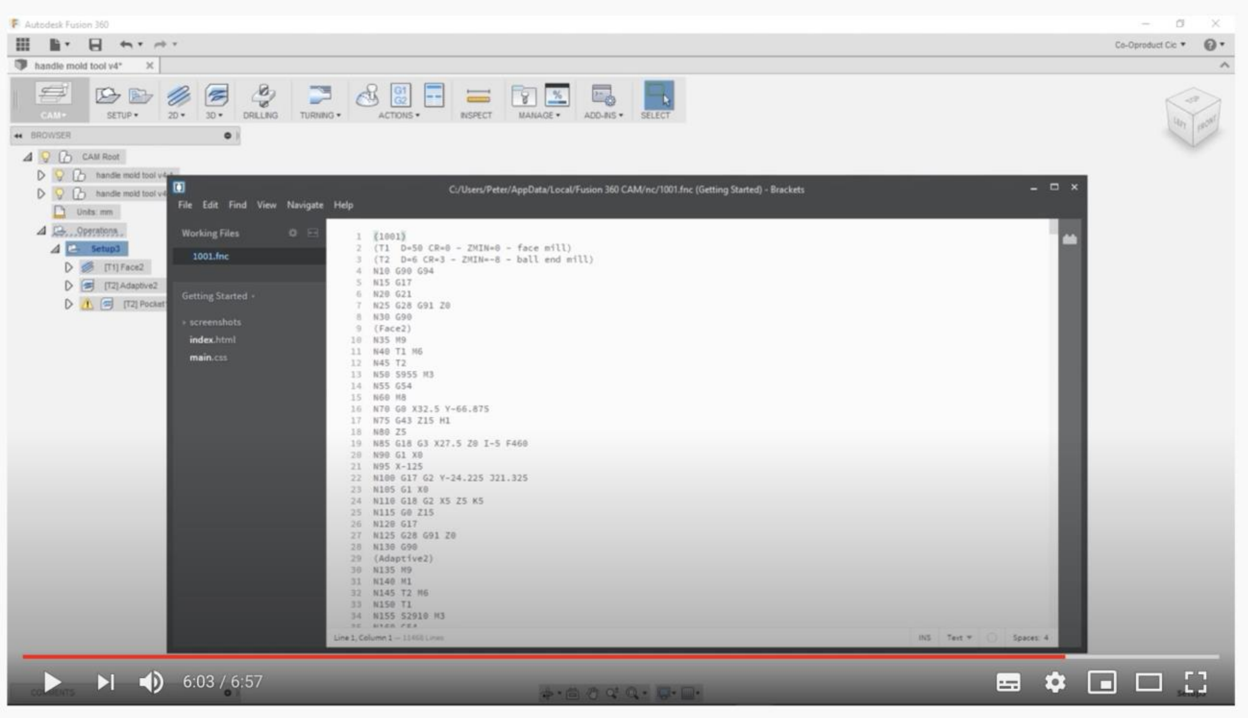

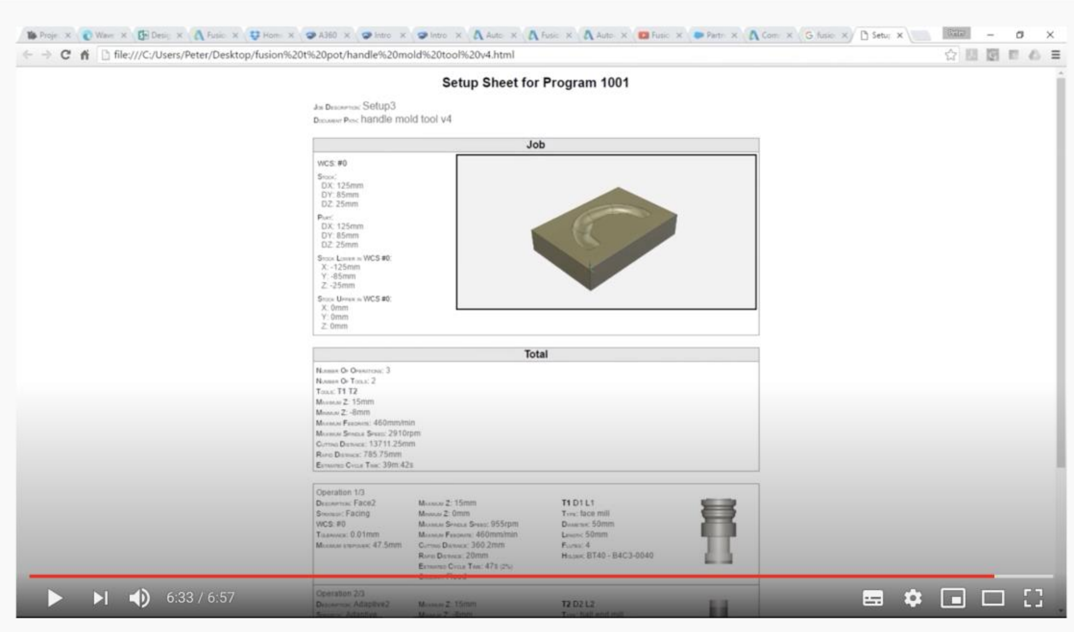

CAM

- https://www.youtube.com/watch?v=00TqO1pBEro

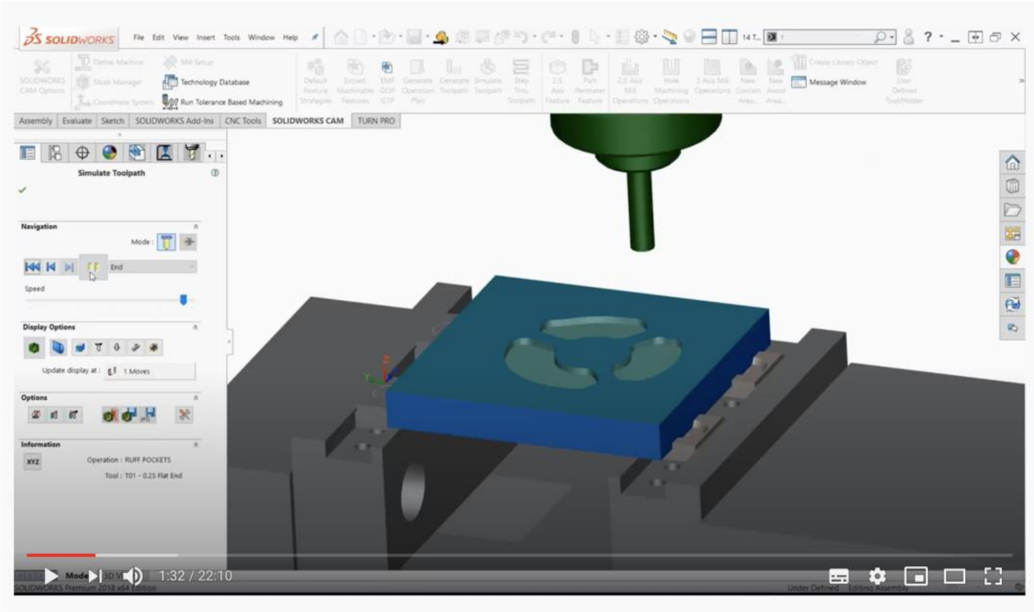

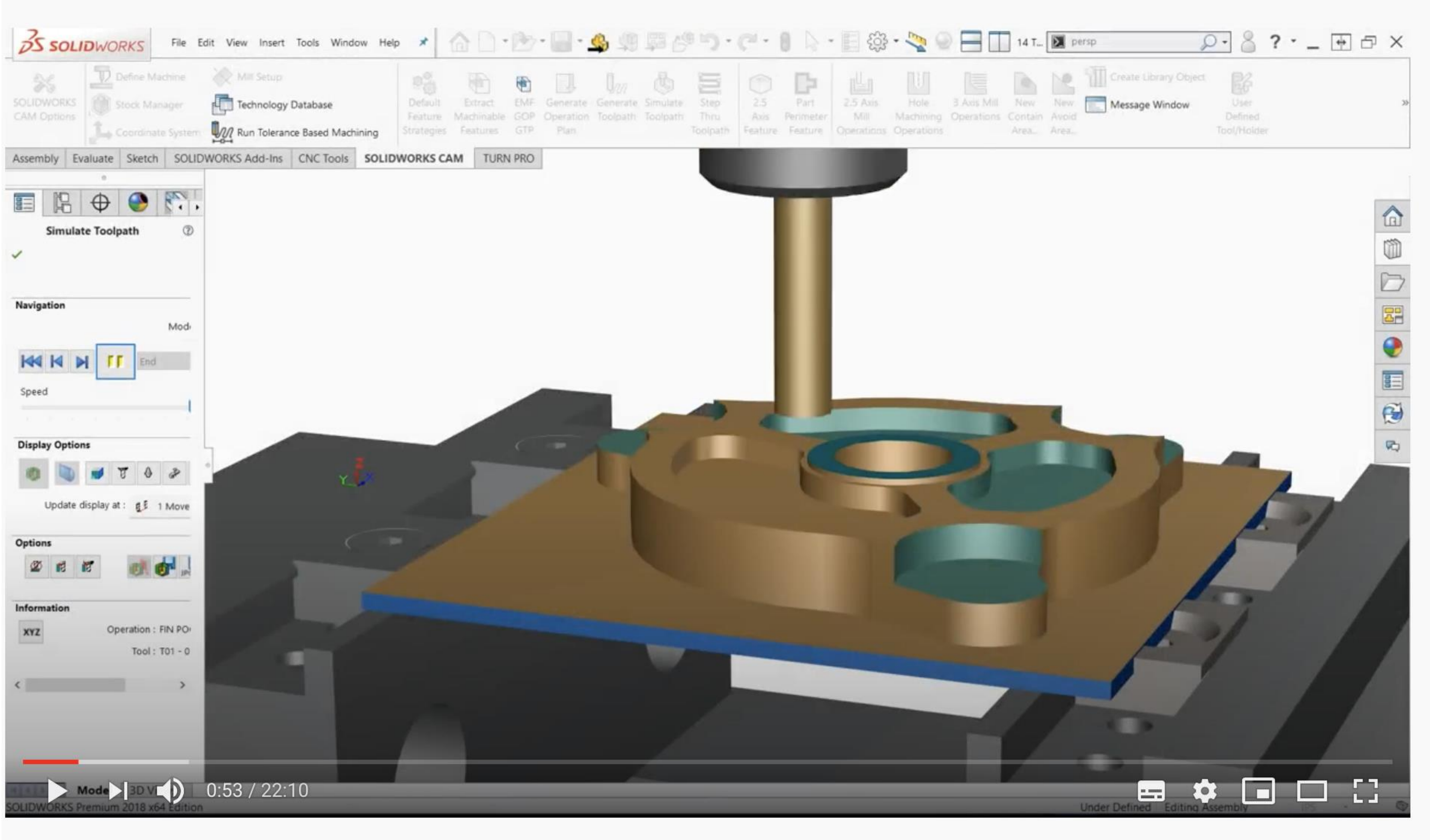

CAM

- https://www.youtube.com/watch?v=00TqO1pBEro

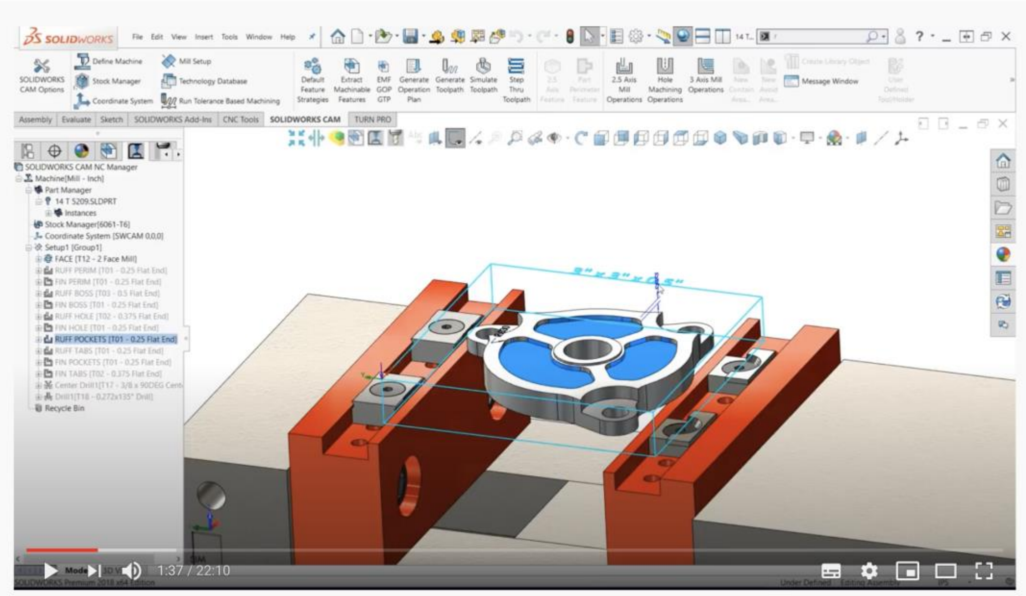

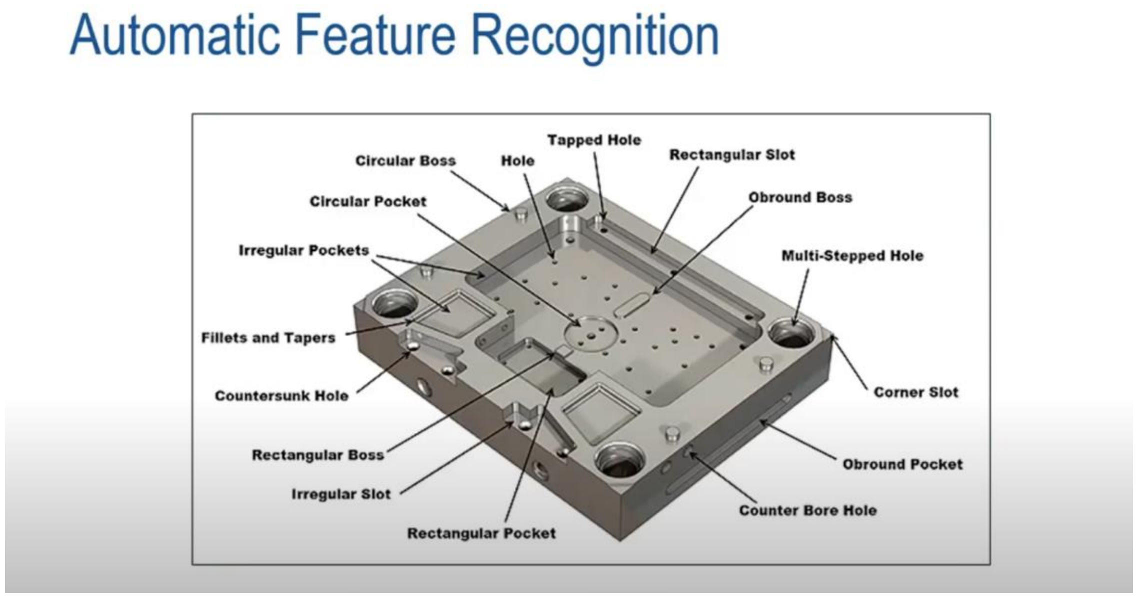

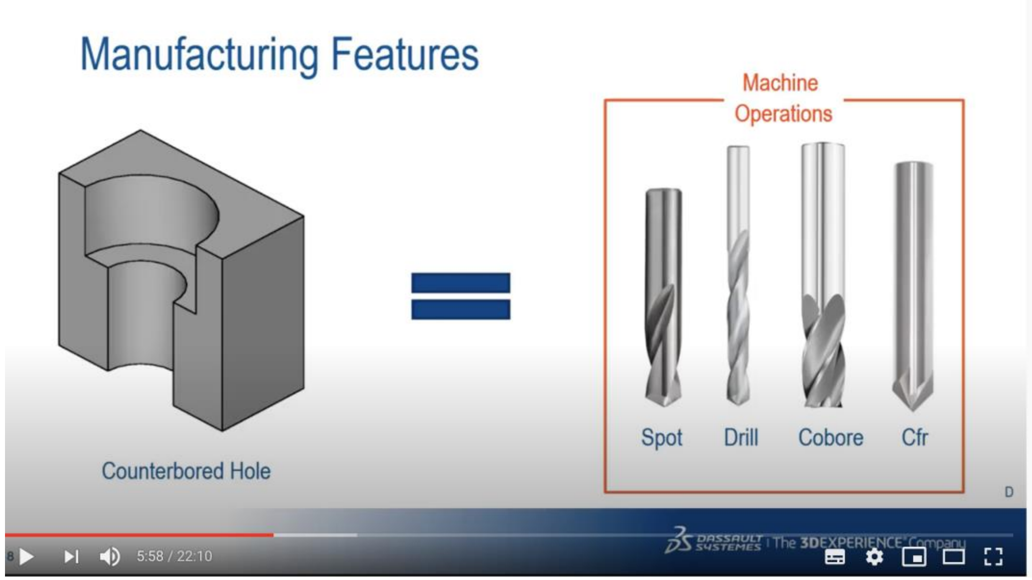

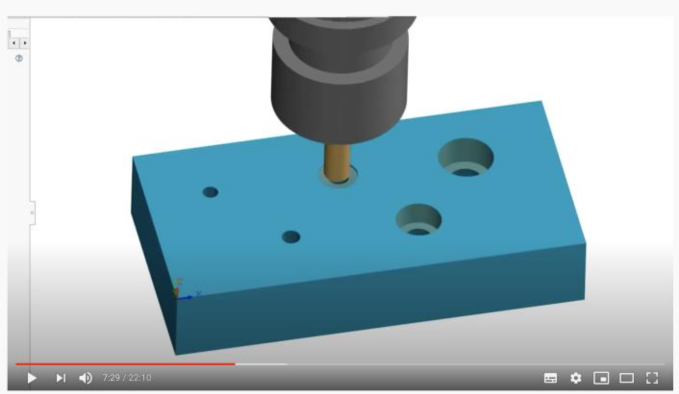

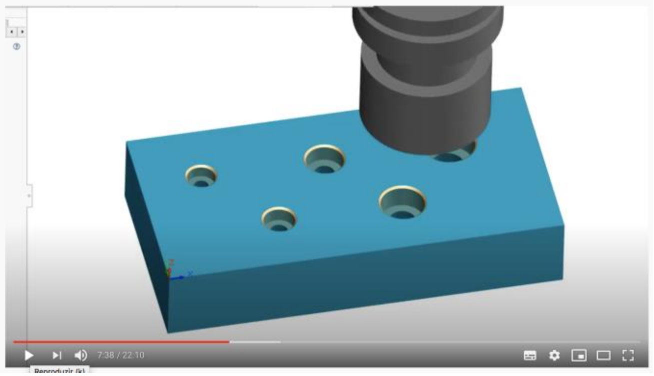

Atividade

- Dê 3 exemplos do uso do CAD, FEA e CAM para simulação da fabricação de componentes mecânicos.
- Esses exemplos devem ser descritos detalhamente, mostrando cada etapa em CAD, FEA e CAM
- Não há necessidade de programar, mas de ilustrar cada uma das etapas
- Exemplo: Uma barra engastada: Material, dimensões, solicitações (mecânicas, térmicas...), seleção de processos de manufatura (fundição, usinagem, laminação??) com justificativa.

Agradecimentos

Dr Newton Kiyoshi Fukumasu

Dra Vanessa Seriacopi

Prof. Dr. Roberto Martins de Souza

LFS - USP